ABSTRACT

Title of Document: A HYBRID AIR CONDITIONER DRIVEN BY
                                      A HYBRID SOLAR COLLECTOR

                                      Ali Al-Alili, Doctor of Philosophy, 2012

Directed By: Professor, Reinhard Radermacher, Department
                                      of Mechanical Engineering

The objective of this thesis is to search for an efficient way of utilizing solar energy in
air conditioning applications. The current solar Air Conditioners (A/C)s suffer from
low Coefficient of Performance (COP) and performance degradation in hot and
humid climates. By investigating the possible ways of utilizing solar energy in air
conditioning applications, the bottlenecks in these approaches were identified. That
resulted in proposing a novel system whose subsystem synergy led to a COP higher
than unity. The proposed system was found to maintain indoor comfort at a higher
COP compared to the most common solar A/Cs, especially under very hot and humid
climate conditions.

The novelty of the proposed A/C is to use a concentrating photovoltaic/thermal
collector, which outputs thermal and electrical energy simultaneously, to drive a
hybrid A/C. The performance of the hybrid A/C, which consists of a desiccant wheel,
an enthalpy wheel, and a vapor compression cycle (VCC), was investigated
experimentally. This work also explored the use of a new type of desiccant material,

which can be regenerated with a low temperature heat source. The experimental results showed that the hybrid A/C is more effective than the standalone VCC in maintaining the indoor conditions within the comfort zone. Using the experimental data, the COP of the hybrid A/C driven by a hybrid solar collector was found to be at least double that of the current solar A/Cs. The innovative integration of its subsystems allows each subsystem to do what it can do best. That leads to lower energy consumption which helps reduce the peak electrical loads on electric utilities and reduces the consumer operating cost since less energy is purchased during the on peak periods and less solar collector area is needed.

In order for the proposed A/C to become a real alternative to conventional systems, its performance and total cost were optimized using the experimentally validated model. The results showed that for an electricity price of 0.12 $/kW-hr, the hybrid solar A/C's cumulative total cost will be less than that of a standard VCC after 17.5 years of operation.

A HYBRID AIR CONDITIONER DRIVEN BY A HYBRID SOLAR COLLECTOR

By

Ali Al-Alili

Dissertation submitted to the Faculty of the Graduate School of the
University of Maryland, College Park, in partial fulfillment
of the requirements for the degree of
Doctor of Philosophy
2012

Advisory Committee:
Professor Reinhard Radermacher, Chair
Professor Michael Ohadi
Associate Professor Bao Yang
Associate Professor Keith Herold, Dean's Representative
Research Associate Professor Yunho Hwang

Acknowledgements

Table of Contents

List of Tables

List of Figures

Nomenclature

Abbreviations	Description	Units
A/C	Air Conditioner	
ABS	Absorption cycle	
AQSOA	AQua SOrb zeolitic Adsorbent	
ARI	American Refrigerant Institute	
ARI	Air-Conditioning and Refrigeration Institute	
ASHRAE	American Society of Heating, Refrigerating and Air Conditioning Engineers	
B	Bias error	
COP	Coefficient of Performance	
CPC	Compound Parabolic Collector	
CPVT	Concentrating Photovoltaic/Thermal	
DB	Dry Bulb temperature	^{o}C
DC	Direct current	
DP	Dew Point temperature	^{o}C
DW	Desiccant Wheel	
DWC	Desiccant Wheel Cycle	
EC	Evaporative Cooler	
EES	Engineering Equation Solver	
ESF	Electrical Solar Fraction	
ETC	Evacuated Tube Collector	
EW	Enthalpy Wheel	

Exp	Experimental	
FAM	FerroAluMinophosphate	
FPC	Flat Plate Collector	
FPVT	Flat Photovoltaic/Thermal collector	
FS	Full Scale	
GA	Genetic Algorithm	
GENOPT	Generic Optimizer	
HRW	Heat Recovery Wheel	
HX	Heat eXchanger	
ISOC	Integrated Systems Optimization Consortium	
MDB	Mean coincident Dry Bulb temperature	^{o}C
MFR	Mass Flow Rate	kg/hr
MMB	Moisture Mass Balance	
MOGA	Multi Objective Genetic Algorithm	
MOOP	Multi Objective Optimization Problem	
MR	Moisture Removal	
MRC	Moisture Removal Capacity	kg_W/hr
MRR	Moisture Rejected Rate	kg_W/hr
MWB	Mean coincident Wet Bulb temperature	^{o}C
NREL	National Renewable Energy Laboratory	
P	Precision error	
PS	Pattern Search	
PV	PhotoVoltaic	

PVT	PhotoVoltaic/Thermal collector	
RD	Reading	
RPH	Revolution Per Hour	
S	Sample Standard deviation	
SACE	Solar Air Conditioning in Europe	
SEER	Seasonal Energy Efficiency Ratio	
SF	Solar Fraction	
SHX	Sensible Heat Exchanger	
SPAC	Solar Powered Absorption Cycle	
SW	Sensible Wheel	
TC	Thermocouple	
TEB	Total Energy Balance ratio	
TMY2	Typical Meteorological Year 2	
TRNEdit	TRNSYS Editor	
TRNOPT	TRNSYS Optimizer	
TRNSYS	Transient Systems Simulation	
VCC	Vapor Compression Cycle	
WAHX	Water-Air Heat Exchanger	

Symbol	**Description**	**Units**
$\dot{m}$	Mass flow rate	kg_a/hr
ε_{HW}	Effectiveness of the Enthalpy Wheel	-
$\bar{x}$	Mean value	

A	Area	m^2
C	Concentration Ratio	
c	Speed of light	m/s
C	Cost	$
C_{min}	minimum fluid heat capacity rate	W/^{o}C
Cp	Heat capacity	kJ/kg-K
CS	Control Signal	
D	Diameter	m
dp	Pressure drop	kPa
E	Energy rate	kW
E_p	Photon energy	eV
ESF	Electrical Solar Fraction	-
F	Control function	
F,i	Fluid inlet	
$F_{1,2}$	Iso-potential line	
f_{comp}	Compressor frequency	Hz
F_{dirt}	Scaling factor for dirt on a mirror	
FF	Filling Factor	-
F_H	Carnavos correction factor	-
$F_{n,k}$	Iso-potential lines	-
F_{shade}	Scaling factor for shading of a mirror	
F_{shape}	Scaling factor for mirror shape error	-
$F_{uniformity}$	Scaling factor for non-uniform radiation	-

G	Solar irradiance	W/m^2
h	Enthalpy	kJ/kg
h_{cw}	Water side heat transfer coefficient for convection	
h_{fg}	Latent heat of water	kJ/kg_w
h_p	Planck constant	eV-s
I	Current	Amp
k	Thermal conductivity	W/m-K
L_A	Purchased energy with solar collectors	kW-hr
L_o	Total purchased energy without solar collectors	kW-hr
m	Mass	kg
N	Number	
n	Day number	-
Nu	Nusselt number	
ø	Latitude	Degrees
P	Pressure	kPa
P	Electrical energy	kW-hr
P_{comp}	Compressor work	kW
Pr	Prandtl number	
Q	Heat transfer rate	kW
Re	Reynolds number	
RH	Relative Humidity	%
R_{speed}	Rotational Speed	RPH

s	Entropy	kJ/kg-K
t	Time	Hr
T	Temperature	$^{\circ}$C
$t_{95\%}$	T-distribution (probability of 95%)	
TC	Total Cost	$
t_s	Local Solar Time	hr
TSF	Thermal Solar Fraction	-
U	Overall heat transfer coefficient	W/m^2-$^{\circ}$C
U_f	Uncertainty in a function f	
$\tilde{U}_L$	Modified overall heat loss coefficient	W/m^2-$^{\circ}$C
V	Volume	m^3
V	Voltage	
VCC	Vapor Compression Cycle	-
w	Humidity ratio	kg$_w$/kg$_a$
α	Sun's Altitude	Degrees
β	Temperature coefficient of the solar cell	W/$^{\circ}$C
γ	Sun's Azimuth angle	Degrees
γs	Surface-solar azimuth angle	Degrees
δ	Sun's declination angle	Degrees
ε	Effectiveness	
η	Efficiency	-
θz	Sun's zenith angle	Degrees
λ	Wavelength	µm

ρ	Reflectivity	
Σ	Surface tilt angle	Degrees
τ	Transmissivity	-
ω	Solar hour angle	Degrees

Subscripts	**Description**
a	aperture
air	Air
amb	ambient
batt	batteries
c	photovoltaic cell
coll	solar collector
$coll_{in}$	collector input
$coll_{out}$	collector output
Comp	compressor
d	direct component of the solar irradiance
e	electricity
elec	electrical
$elec_{coll}$	collector electrical
elect	electrical
evap	evaporator
exp	experimental
f	Fluid

fanExh	exhaust fan
fanSupp	supply fan
fg	vaporization
gen	generator
HT	heater
hx	heat exchanger
i	the ith node
i	Inlet
in	Inlet
init	initial
inv	inverter
isen	isentropic
L	Load
lat	Latent
m	mirror
min	minimum
op	operational
P	Pump
r	reference
ref	reference
reg	regeneration
sc	sub-cooling
sens	sensible

sh	superheat
sim	simulation
st	storage tank
sup	supply
sys	complete hybrid solar air conditioner system
tank	hot water storage tank
tank	hot water storage tank
tf	tube and fluid
th	thermal
ther	thermal
tot	Total
u	useful
VCC	vapor compression cycle
vol	volumetric

1. Background and Literature Review

1.1 Fundamentals of Solar Radiation:

1.1.1 Solar Radiation Geometry

Understanding the motion of the sun with respect to an observer is very essential, especially in the design phase of a system utilizing solar energy. In order to be able to collect the solar energy available at any location, one should be able to predict the sun's position relative to the collecting devices. This knowledge would help utilize the solar energy in the most effective way. The information can be used to estimate the energy intercepted by various surfaces and predict the performance of the collecting devices.

The Earth-Sun Angles are the hour angle ω, the declination angle δ and the latitude angle $\emptyset$, Figure 1 .
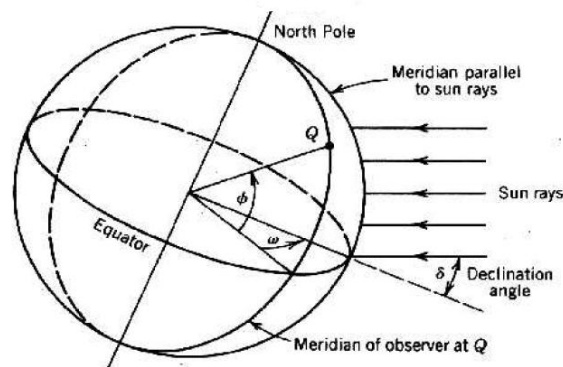
Figure 1: Earth-Sun Angles (Stine and Geyer, 2001)

The hour angle is the angular distance between the meridian of the observer and the meridian whose plane contains the sun. It is considered be zero at solar noon. Equation

(1) shows how the hour angle is calculated knowing the solar time, t_s. The solar time is based on the 24-hour clock and must be used in all the solar radiation calculations.

$$\omega = 15(t_s - 12) \tag{1}$$

The declination angle is the angle between the earth's equatorial plane and the line that connects the center of the earth and the sun. This angle is found by using Equation (2) (Threlkeld *et al.*, 1998).

$$\delta = 23.45 \sin \left[360 \left(\frac{284 + n}{365} \right) \right] \tag{2}$$

The latitude angle is the angle between the earth's equatorial plane and the line connecting a point on the earth's surface to the center of the earth.

Figure 2 shows the Observer-Sun Angles, which are the sun's Zenith angle θ_z, sun's Altitude α and sun's Azimuth angle γ.
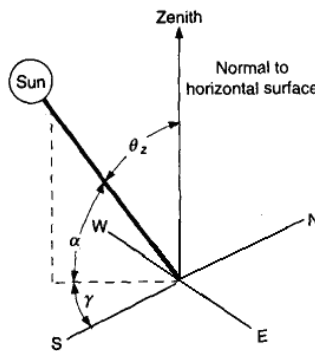
Figure 2: Observer-Sun Angles

2

The Sun's Altitude Angle is the angle between the direct ray from the sun and the observer horizontal plane. Knowing the declination angle, hour angle and the latitude, the sun's altitude can be calculated, Equation (3).

$$\sin(\alpha) = \cos(\delta)\cos(\omega)\cos(\phi) + \sin(\delta)\sin(\phi) \tag{3}$$

Equation (4) is used to calculate the solar Zenith angle which is the complement of the Sun's Altitude Angle.

$$\theta_z = 90 - \alpha \tag{4}$$

The solar Azimuth angle is measured clockwise on the observer horizontal plane from the south axis to the projection of the sun's ray. Equation (5) shows how the solar Azimuth angle is calculated.

$$\cos(\gamma) = \frac{\cos(\delta)\cos(\phi)\cos(\omega) - \sin(\delta)\sin(\phi)}{\cos(\alpha)} \tag{5}$$

The sign convention of these various angles can be found in Table 1.

Table 1: Sign convention of the Earth-Sun Angles and Observer – Sun Angles

Title	Symbol	Zero	Range	Positive Direction
Latitude	ø	Equator	± 90°	Northern Hemisphere
Declination	δ	Equinox	± 23.45°	Summer
Hour Angle	ω	Noon	± 180°	Afternoon
Sun Altitude	α	Horizontal	[0-90]°	Upward
Sun Zenith	θz	Vertical	[0-90]°	Toward Horizon
Sun Azimuth	γ	South	± 180°	Clockwise

Knowing the sun-earth angles, the relation of sun's rays to a tilted surface can be established. Equation (6) shows how the surface-solar azimuth angle is defined.

3

$$\gamma_s = |\gamma - \psi| \tag{6}$$

for East, South, West and North, the values for the vertical surface azimuth angles used are -90°, 0°, 90° and 180°, respectively.

Based on the surface tilt angle Σ, 0° for horizontal and 90° for vertical surfaces, the sun's incidence angle on the surface can be calculated as shown in Equation (7).

$$\cos(\theta) = \cos(\alpha)\cos(\gamma_s)\sin(\Sigma) + \sin(\alpha)\cos(\Sigma) \tag{7}$$

1.1.2 Solar Radiation Components and Resources

The sun can be treated as a blackbody at an effective temperature of 5760K. The maximum spectral intensity occurs in the green portion of the visible light at 0.48 μm. The sun's extraterrestrial spectral irradiance distribution is shown in Table 2.

Table 2: The sun's extraterrestrial spectral irradiance

Spectral Range	Percentage of the total extraterrestrial solar irradiance [0.120-100] μm [%]
UV - below 0.40 μm	8.7
Visible region [0.40 - 0.70] μm	38.2
Infrared region – above 0.7 μm	53.1

However, the solar irradiance undergoes considerable attenuation as it passes through the atmosphere as a result of absorption and scattering. The spectral distribution of solar irradiance on the ground can be seen in Figure 3. Even on a cloud free day with unpolluted sky, about 30% of the incident energy on earth is lost (Kreith and Kreider, 1978). Practically, all of the solar radiation reaching the earth's surface falls in the wavelength band from 0.3 – 2.5 μm.
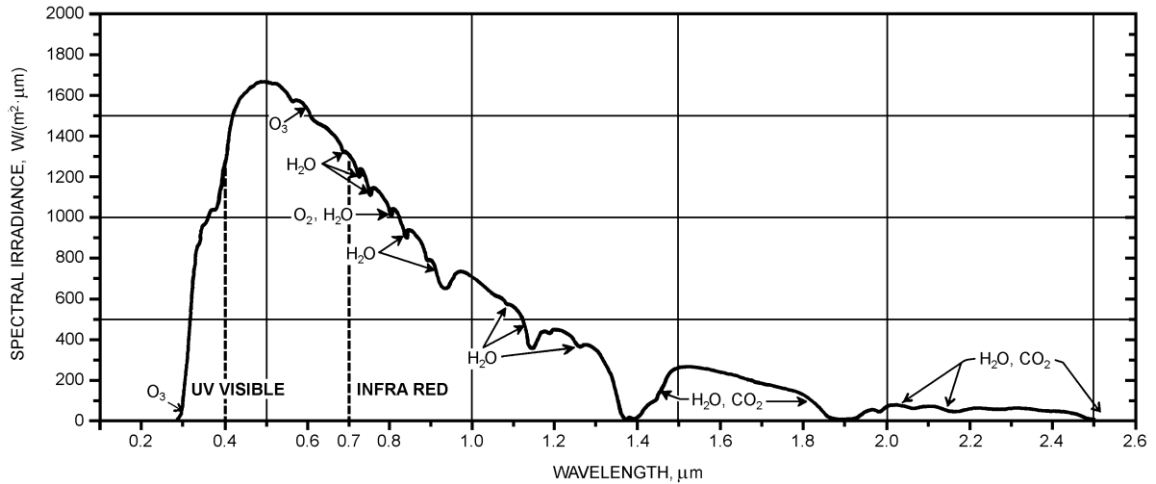
Figure 3: Spectral distribution of solar irradiance at sea level for air mass = 1 (ASHRAE, 1999)

The total solar flux striking a surface generally consists of three components: direct, diffuse and reflected. A pyranometer is used to measure the total radiation, whereas a pyrheliometer is used to measure the direct component, Figure 4. The direct normal or beam component is that received from the sun without having been scattered by the atmosphere. The diffuse radiation is that received from the sun after its direction has been changed due to scattering by the atmosphere. The reflected radiation is that which is received after being reflected from surrounding surfaces or the ground.

Figure 4: Pyranometer and Pyrheliometer

Analysis to predict long-term performance of solar energy systems rely on the availability of solar radiation data. These data include measurements of global horizontal irradiance,

diffuse irradiance, and direct irradiance in W/m^2. Table 3 shows several US resources for solar radiation data.

Table 3: Several US sources for solar radiation data

Source	Brief Description
The US National Solar Radiation Data Base (NSRDB)	Contains hourly solar radiation data for 239 National Weather Service Stations from1961 to 1990 (TMY2)
Measurement and Instrumentation Data Center (MIDC)	Provides irradiance and meteorological data from stations throughout the United States (NREL)
Baseline Measurement System (BMS)	Provides live solar radiation data from approximately 70 instruments at the NREL South Table Mountain site and historical measurements dating to 1981(NREL).
Renewable Resource Data Center (RRDC)	Provides information about biomass, geothermal, solar, and wind energy resources (NREL)
Cooperative Networks for Renewable Resource Measurements (CONFRRM)	Provides solar radiation and wind measurement data for select U.S. locations (NREL)
Historically Black Colleges and Universities Solar Radiation Monitoring Network:	Provides 5-minute measurements of solar irradiance for six stations in the southeastern United States from 1985 to 1996. (NREL)
Solar Radiation Data Manual for Flat Plate and Concentrating Collector	Data for 50 states. (NREL)

1.2   Solar Energy Collection Technologies:

1.2.1   Solar Thermal Collectors

Solar collectors can be regarded as a special kind of heat exchangers in which solar radiation energy is transferred to the internal energy of the transport medium. These solar thermal collectors can be divided into two main groups based on their motion as shown in Table 4 (Kalogirou, 2004). The first group is the non tracking collectors in which the collector is fixed at certain title angle, usually within 5 to 10 degrees with respect to the

latitude angle. This group includes concentrating and non-concentrating collectors. In the non-concentrating collectors, the same area is used to intercept and absorb the solar radiation. Two type of collectors fall into the non-concentrating category: flat plate collectors (FPC) and evacuated tube collectors (ETC). The second group is the tracking collectors in which a reflected or a refracted surface is used to intercept and focus the solar radiation into a smaller receiving area.

Table 4: Classification of solar thermal collectors (Kalogirou, 2004).

Motion	Collector type	Absorber type	Concentration ratio	Indicative temperature range (°C)
Stationary	Flat plate collector (FPC)	Flat	1	30−80
	Evacuated tube collector (ETC)	Flat	1	50−200
	Compound parabolic collector (CPC)	Tubular	1−5	60−240
Single-axis tracking			5−15	60−300
	Linear Fresnel reflector (LFR)	Tubular	10−40	60−250
	Parabolic trough collector (PTC)	Tubular	15−45	60−300
	Cylindrical trough collector (CTC)	Tubular	10−50	60−300
Two-axes tracking	Parabolic dish reflector (PDR)	Point	100−1000	100−500
	Heliostat field collector (HFC)	Point	100−1500	150−2000

The stationary collectors can be used for low and moderate temperature applications, such as domestic water heating, building heating and air conditioning. They can utilize both beam and diffuse solar irradiation. The main advantage of these collectors is that they require little maintenance. On the other hand, with tracking collectors, higher working fluid temperatures can be achieved. The concentrator helps increase the solar radiation flux and reduce the receiver area, hence reducing the heat loss. In addition, the thermal efficiency is higher especially at higher temperatures. Since these collectors utilize mainly the beam radiation, they are required to track the sun. The tracking mechanism should be reliable and tracks with a certain degree of accuracy. There are two methods in which the collector can track the motion of the sun. The first one is the altitude-azimuth method which is a two-axes tracking method. The second is the one-axis

tracking method which requires the tracking device to track the sun in either East to West or North to South motion. If the collector is orientated in an East - West orientation, very little collector adjustment is required and the full aperture always faces the sun at noon time. It requires an approximate ± 30°/day motion (Goswami *et al.*, 2000). However, the collector's performance decreases during early and late hours of the day due to the cosine effect. On the other hand, if the collector is oriented in a North - South direction, the cosine loss is less in the morning and evening and the collector performs less efficiently at noon. This orientation requires about 15°/hr motion (Goswami *et al.*, 2000).

1.2.2 Photovoltaic Cells

Photovoltaic (PV) conversion is the direct conversion of sunlight into electricity. The photovoltaic devices can be made from various types of semiconductor materials. Semiconductors are materials with valence band partly filled and have intermediate band gaps (≤ 3 eV). Table 5 shows various PV materials with their respective band gaps and maximum theoretical efficiencies (Roger and Ventre, 2005). They can be divided into intrinsic (pure) and extrinsic (doped with impurities) semiconductors. Based on the dopant material, *n*-type or *p*-type semiconductors can be created. When the dopant material has more electrons in the valence band than the semiconductor, *n*-type semiconductors are created. If on the other hand, the semiconductor is doped with material with a deficiency of electrons in its outer shell, *p*-type is created. When a *p* and an *n* type material are joined together, creating a *p-n* junction, excess electrons from *n* layer jump to fill the holes in the *p* layer. This leads to the formation of a positive charge on the *n* side close to the junction and a negative charge on the *p* side. This makes the *p-n* junction behave like a diode since the negative charges on the *p* side restrict the

movement of additional electrons from the *n* side to the *p* side, while the positive charges

at the junction on the *n* side made the movement of additional electrons from the *p* to the

n side easier.

Table 5: Theoretical conversion efficiency limits for several PV materials at 25°C (Roger and Ventre, 2005).

Material	E_g	η_{max}
Ge	0.6	13%
CIS	1.0	24%
Si	1.1	27%
InP	1.2	24.5%
GaAs	1.4	26.5%
CdTe	1.48	27.5%
AlSb	1.55	28%
a-Si:H	1.65	27%
CdS	2.42	18%

When solar irradiance strikes the solar cell, the light photon is absorbed by a valence

electron increasing its energy by the amount of energy of the photon, Equation (8).

$$E_p = h_p f = \frac{h_p c}{\lambda}(Joules) = \frac{1.24}{\lambda(\mu m)}(eV) \tag{8}$$

If the energy of the photon is equal to or larger than the band gap of the semiconductor,

the electron with excess energy will jump into the conduction band. The excess energy

over the band gap increases the kinetic energy of the photon. However, if the photon

energy is less than the band gap, the electron will not be able to jump into the conduction

band and the excess energy gained is dissipated as heat which increases the cell

temperature. For example, for Ge, band gap of 0.6, photons of sunlight at a wavelength

of 0.51 may be converted to electricity at a maximum efficiency of 100% while photons

at lower wavelengths will be converted at lower efficiencies.

Figure 5 shows a typical I-V and power characteristics of a PV module. The maximum current, short circuit current, is obtained when the voltage in the circuit is zero. Conversely, the maximum voltage, open circuit voltage, is produced when there is a break in the circuit which means that the resistance is infinitely high and there is no current. The figure shows the maximum power which corresponds to the maximum rectangle area under the I-V curve. The voltage and the current corresponding to the maximum power are V_{mp} and I_{mp}, respectively.
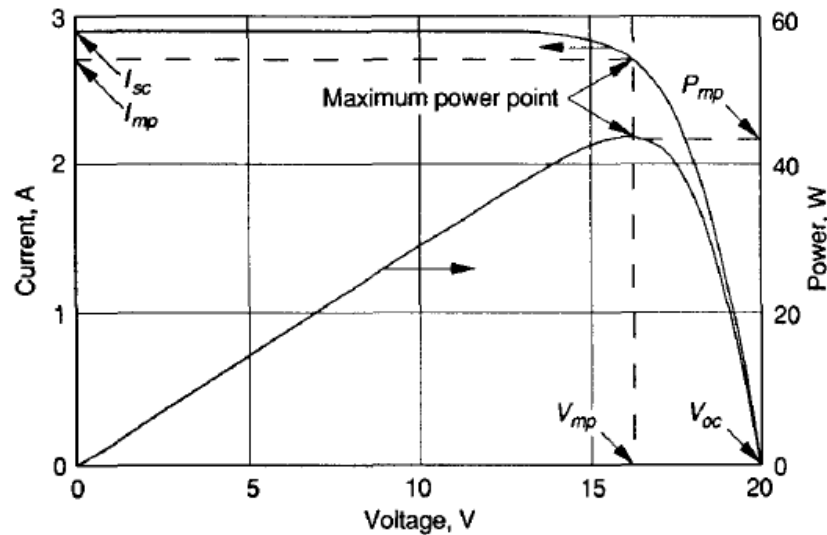
Figure 5: Typical I-V and power characteristics of a PV module (Duffie and Beckman, 1991)

Figure 6 shows an equivalent circuit of an illuminated PV cell with internal series and shunt resistances. This circuit can also represent an equivalent circuit of a module of PV cells or an array of PV modules.
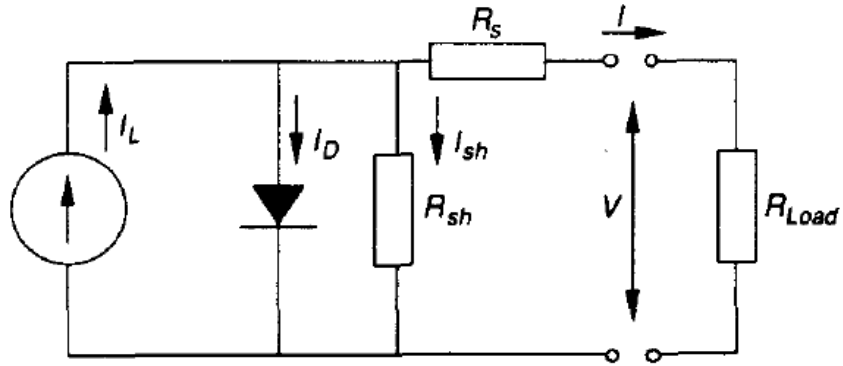
Figure 6: Equivalent circuit of a PV cell (Duffie and Beckman, 1991)

It has to be noted that the amounts of current and voltage available from the cell depend on the solar irradiance level. Figure 7 shows I-V characteristics of real and ideal PV cells under different irradiance levels.
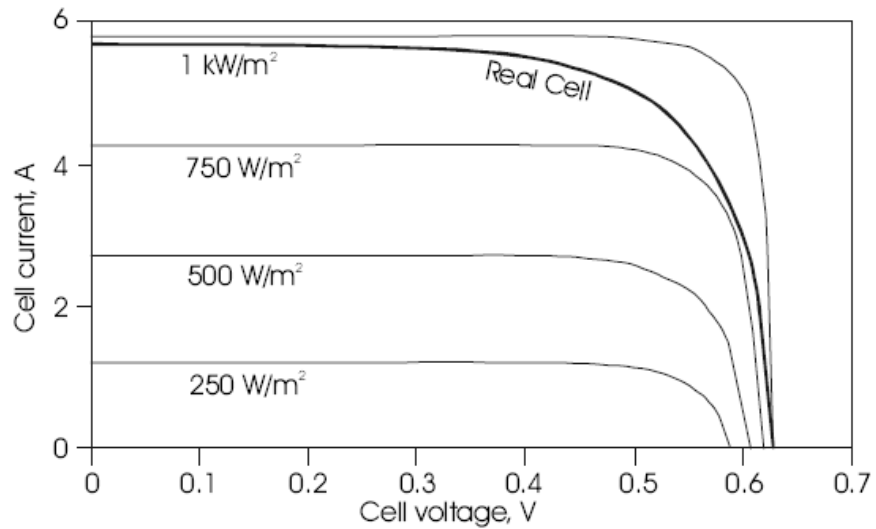
Figure 7: I-V characteristics of PV cells under different irradiance levels (Roger and Ventre, 2005)

One of the factors that affect the performance of a PV cell is the cell temperature. The open circuit voltage is directly proportional to the absolute temperature of the cell. In addition, the reverse saturation current is highly temperature dependent while the short circuit current remains nearly constant. The PV cell efficiency decreases with increasing

temperature, the cells might also exhibit long term degradation if the temperature exceeds a certain limit. A simple linear model can be used to predict the cell's efficiency as a function of temperature. (Royne et al., 2005).

$$\eta = a(1 - bT_c) \tag{9}$$

Where a and b are parameters describing a particular cell. The electrical power output is then given by Equation (10).

$$P_{elec} = \eta T_c \tag{10}$$

The effect of the temperature on the power output can be seen in Figure 8.
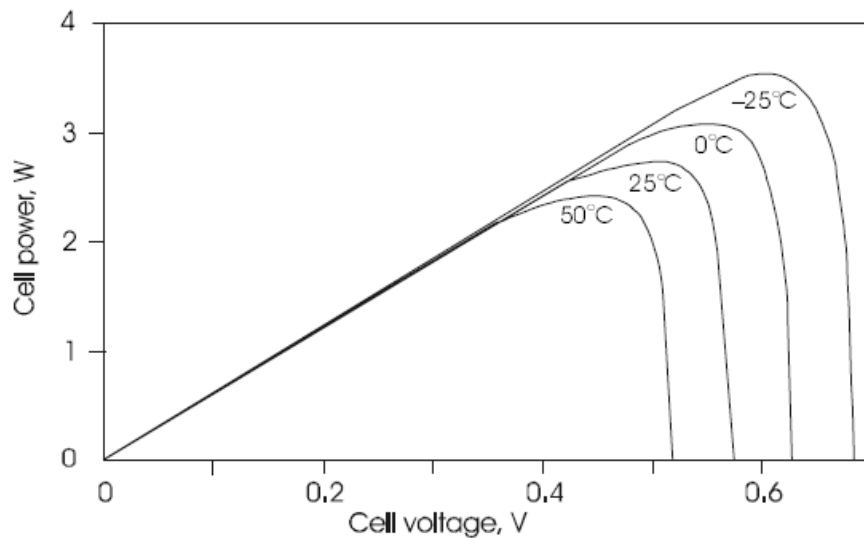
Figure 8: Temperature dependence of the cell's power output (Royne et al., 2005)

A typical photovoltaic cell produces less than 3 watts at approximately 0.5 volt DC (Roger and Ventre, 2005). Therefore, cells must be connected in series-parallel configurations to produce enough power to meet the load. Series connection results in addition of voltages whereas parallel connection results in addition of currents, Figure 9.

12
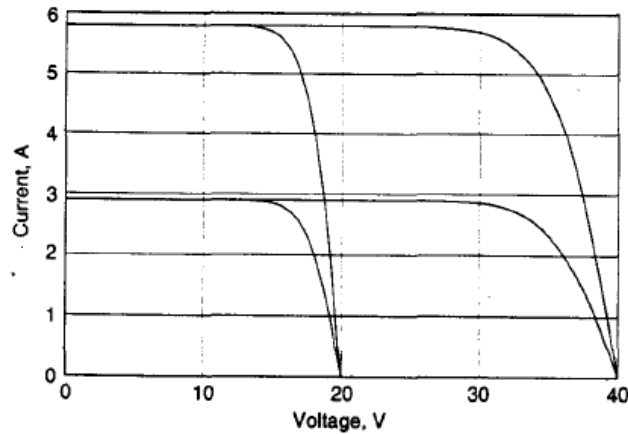
Figure 9: I-V curves of PV cells connected various series and parallel arrangements
(Duffie and Beckman, 1991)

1.2.3 Photovoltaic/Thermal Collectors

A Photovoltaic/Thermal collector (PVT) is a combination of photovoltaic cells with a solar thermal collector which converts solar irradiance into electricity and heat simultaneously, Figure 10. Since most of PV cells' efficiencies are less than 25%, which means that the cells would convert less than half of the solar irradiance into electricity, the rest is converted to heat. Therefore, it is important to operate the PV cells under low temperatures to increase their efficiency hence their electrical outputs. This makes cooling PV cells, either passively or actively, attractive especially when designing concentrating PV systems. The cooling media could be fluid (mostly water, air or both). In addition, by combining the two collection technologies in one collector, the amount of energy converted per unit surface area is larger than that of the side by side PV panel and thermal collector.
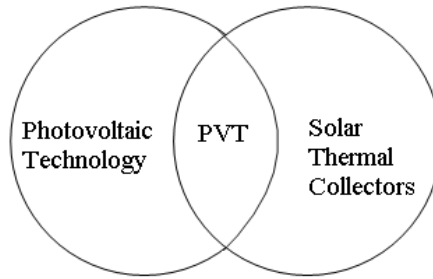
Figure 10: The combination of the PV technology with thermal collectors

PVT collectors might be categorized based on their geometry into three groups: flat PVT, concentrating PVT and building integrated PVT, Figure 11 .
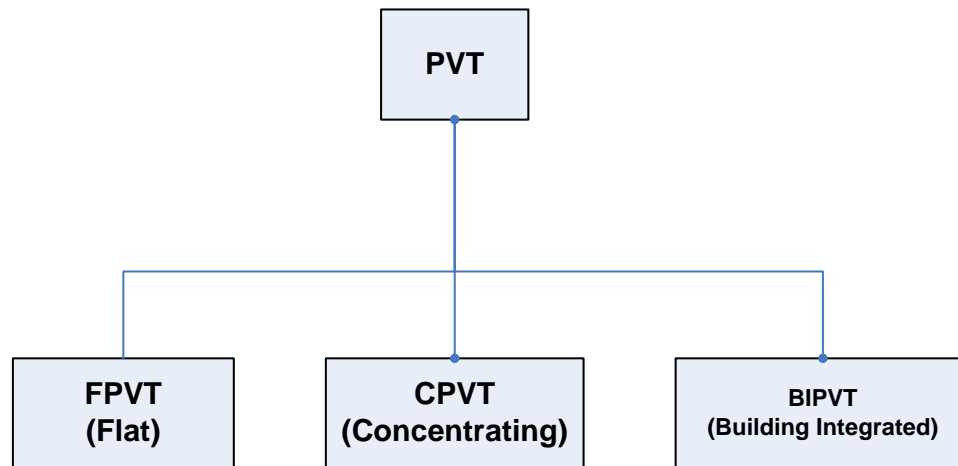
Figure 11: PVT Types

1.2.3.1 Flat PVT Collectors

The flat PVT (FPVT) is basically a flat thermal collector with the PV panel attached on the top of the absorber. The thermal output of FPVT should be expected to be less than that of a flat thermal collector, since part of the available solar irradiance is converted to electricity by the PV cells. Moreover, the optical absorptivity of the PV cells is less than that of a black absorber. The PV material also represents an additional thermal resistance between the absorber plate and the working fluid. On the other hand, the electricity

production should be expected to be higher than a standalone PV module since the PV cells are operating at a lower temperature.

A significant amount of research on PVT collectors has been carried out since mid 1970s. Their performance has been investigated theoretically and experimentally. The theoretical studies include analytical and numerical modeling of the collector. Florschuetz (1979) extended the Hottel-Whillier-Bliss analytical model of the thermal flat collector to the analysis of the FPVT. Zondag (2002) presented four numerical models to predict the performance of PVT collectors: one 3D dynamic model and three steady state models (1, 2 and 3D). The results showed that more energy is produced per unit of surface area using PVT collectors. Based on a control-volume finite-difference approach, an explicit dynamic model was developed for a single-glazed flat-plate water-heating PVT collector by Chow (2003). This explicit dynamic model is capable of producing hourly performance results and instantaneous thermal and electrical gains and efficiencies. Lazarova et al. (2005) investigates the performance of a glazed collector with crystalline-Si cells. Their results indicate that it is possible to obtain more energy per unit of surface area compared to the thermal and the photovoltaic solar collectors separately. Vokas et al. (2006) presented an analytical model where the flat thermal collector's equations are modified to account for the PV laminate. The electrical and thermal performance of the flat PVT has also been investigated experimentally. Fujisawa and Tani (2001) used three different collector configurations, PV and thermal, hybrid collector and hybrid + PV, to find an optimal design to minimize the auxiliary energy for a residential photovoltaic-thermal binary utilization system. Zondaga et al (2003) evaluated nine different water

type PVT collectors. They found that the channel-below-transparent-PV design gives the best efficiency.

The thermal output of the PVT has been mainly utilized for domestic hot water applications (Zondag et al., 2002, 2003; Chow et al., 2006; Fujisawa and Tani, 2001; Tiwari and Sodha, 2006; Kalogirou and Tripanagnostopoulos, 2006) or direct floor heating (Fraisse et al., 2007). An investigation using Transient Systems Simulation (TRNSYS) was conducted to study the industrial application of two experimentally tested PVT systems using a-Si and pc-Si (Kalogirou and Tripanagnostopoulos, 2007). It was found that in order to keep the electrical and thermal efficiency of PVT systems at an acceptable level, they should be used for applications that need heat in medium temperature level (60-80°C).

Vokas et al. (2006) investigated the collector performance with respect to three different geographical regions for domestic cooling and heating. The approximation methods F-chart heating and F-chart cooling were used for the study of PVT collector for the coverage of the domestic heating load and the summer cooling load, respectively. It was concluded that flat PVT collectors have the potential to cover a remarkable portion of the domestic heating and cooling loads

1.2.3.2 Concentrating PVT Collector

The concentrating PVT (CPVT) has not received as much attention as the flat types with regards to modeling, testing and exploring new applications. Brogren et al. (2001) studied the optical performance of a CPVT using low concentrating Compound Parabolic Concentrator (CPC) with mono-crystalline silicon cells. It was concluded that the electric

output could be increased by 20% by using optimized anti-reflection coating and reflectors for high latitude. Moreover, Nilsson et al. (2007) investigated the electrical and thermal characteristics of an asymmetric CPC with mono-crystalline silicon cells built for high latitudes. Assoa et al. (2007) studied a new concept where air and water were used to cool a CPC with polycrystalline silicon cells. They investigated the performance of the collector numerically and experimentally to find the effect of various parameters on the performance. In addition, the performance of a single axis tracking system using a parabolic trough of 37 concentration ratio with mono-crystalline silicon cells was experimentally investigated by Coventry (2005). He studied the impact of the illumination and temperature non-uniformities across the PV cells on the overall electrical performance of the collector. Moreover, a miniature dish concentrator of concentration ratio up to 400 with triple-junction PV cells was theoretically investigated by Kribus et al. (2006). Later, Mittelman et al. coupled the miniature dish collector with LiBr/H_2O absorption cycle (Mittelman et al., 2007).

1.3 <u>Solar Cooling Processes:</u>

Utilizing solar energy to drive cooling processes is very attractive since the seasonal variation of available solar energy is in phase with the space cooling requirements of buildings. Solar radiation can be converted into thermal energy via thermal solar collectors and used to drive thermally driven cooling cycles, i.e. absorption and adsorption cycles. The solar radiation might also be converted into electrical energy via PV panels and used to power electrically driven cooling cycles, i.e. vapor compression cycle and Peltier cooling systems.

Therefore, the solar cooling technology is classified into two categories: thermally driven cooling cycles and electrically driven cooling cycles. The solar thermal cooling is further divided into three sub-categories: open cycles, closed cycles and thermo-mechanical cycles as shown in Figure 12.
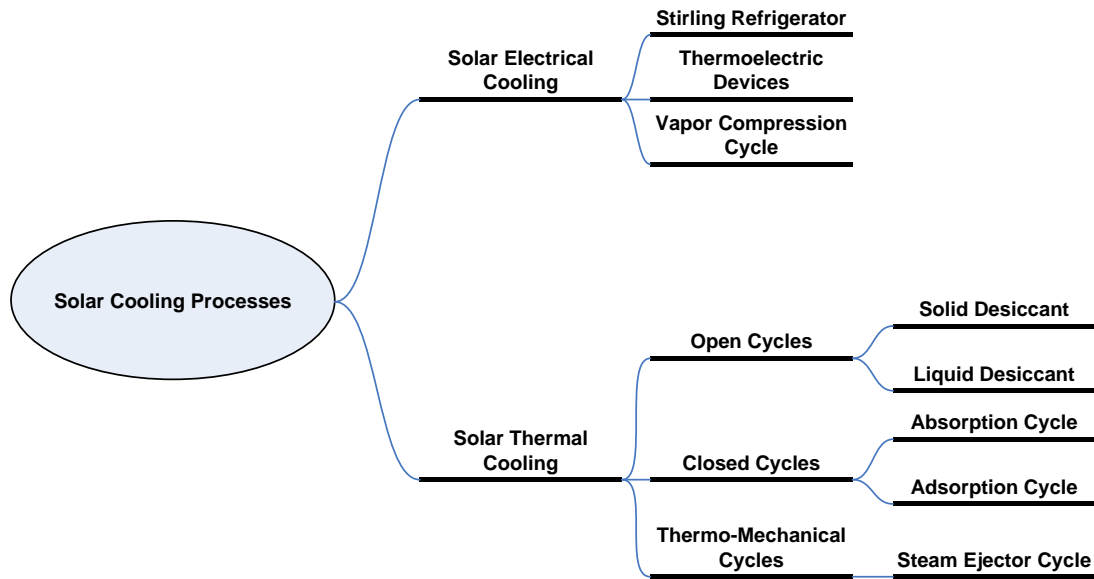
Figure 12: Solar cooling processes classifications

1.3.1 Electrically Driven Cooling Cycles

1.3.1.1 Vapor Compression Cycle

The basic vapor compression cycle (VCC) consists of a compressor, expansion valve and two heat exchangers, Figure 13. It makes use of the boiling and condensing of a working fluid at different temperatures and hence at different pressures. The cooling effect is obtained by transferring the heat from the conditioned space into the fluid at the lower temperature and pressure. This heat causes the working fluid to boil in the evaporator. The vapor is then mechanically compressed to a higher pressure and temperature. This

state has to correspond to a saturation temperature at which its latent heat can be rejected so that it changes back to a liquid in the condenser. In order to reduce the working fluid's pressure from the condenser pressure to the evaporator pressure, a pressure reducing valve is used. Since this process is considered adiabatic, this valve must also cause a corresponding drop in temperature and some of the fluid will flash off into vapor to remove the energy for this cooling. The volume of the working fluid therefore increases at the valve by this amount of flash gas.
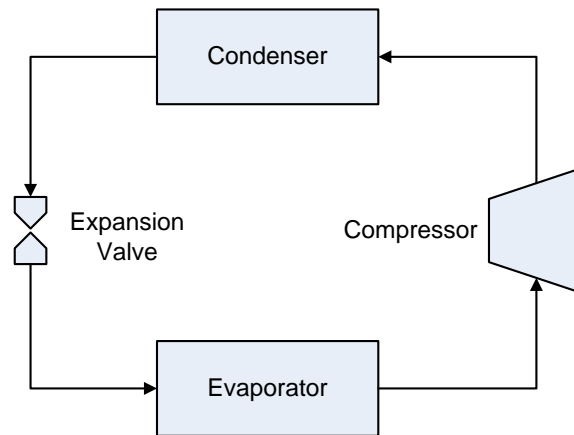
Figure 13: Schematic of a VCC

The overall energy conversion efficiency of the solar powered vapor compression cycle is predominantly determined by the efficiency of the PV devices. It can be obtain by simply multiplying the PV efficiency by the VCC Coefficient of Performance COP. One might argue that the solar driven VCC would not be of interest unless the PV conversion efficiencies exceed that of the grid. In spite of the fact that the grid-powered VCC has a higher energy conversion efficiency than the solar powered VCC, solar driven VCC is still attractive. That is because the primary energy source of the solar powered VCC is the sun, which is a renewable source of energy with minimum impact on the environment. Moreover, the efficiency of the PV cells is in a continuous rise.

1.3.1.2   Thermoelectric Heat Pump

A thermoelectric heat pump is basically a solid-state active heat pump which transfers heat from one side of the device to the other. It operates based on the Peltier effect, in which the direction of the heat flux is determined by the polarity of the applied DC voltage. Figure 14 shows a schematic of a single thermoelectric device. A junction is formed by using two different semiconducting materials, a *p*-type and an *n*-type. The *p*-type contains positive charge carriers (holes) while the *n*-type contains the negative charge carriers (electrons). When the DC voltage is applied in the appropriate direction through the junction, the charge carriers move away from the junction causing a cooling effect at the junction.

The thermoelectric heat pumps are attractive due to many reasons. They have no moving parts which make them reliable and silent in operation. They use no refrigerants and can be made in small sizes. However, their low efficiency have limited their use.
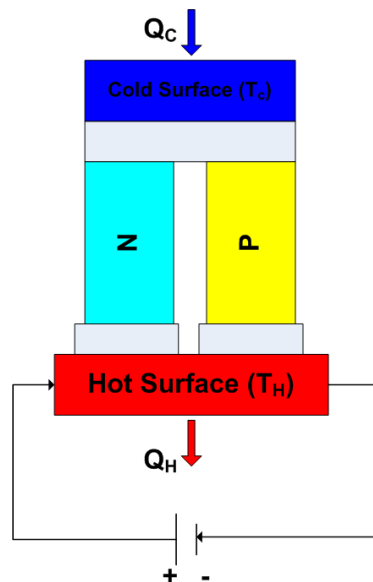
Figure 14: Schematic of a single thermoelectric device

1.3.1.3   Stirling Refrigerator:

The Stirling cycle can be implemented as an engine or a heat pump. The cycle consists of four processes in series: isothermal compression, constant volume heating, isothermal expansion, and constant volume cooling. It is a closed cycle which utilizes a gas that moves back and forth between the cooling and heating spaces. Some of the most commonly used working fluids are air, helium, and hydrogen.

1.3.2   Thermally Driven Cooling Cycles:

Thermal energy produced by the solar thermal collector can be transformed into useful cooling through the thermo-chemical or thermo-physical processes, using thermally activated cycles. The thermally driven cooling cycles can be divided into two main categories: open cycles and closed cycles.

Open sorption cycles refer to solid or liquid desiccant systems. The main purpose of these systems is to transfer moisture from one airstream to another by using two main processes, Figure 15. The first process is the sorption process in which the moisture is transferred from the airstream into the desiccant material. The driving potential of this process is the difference in the water vapor pressure between the humid air and the desiccant material. When the desiccant material is dry and cold, its surface vapor pressure is lower than that of the moist air, so the moisture is adsorbed from the airstream into the desiccant material. The sorption process increases the air temperature because of the release of the heat of adsorption. After the desiccant material becomes wet, desorption of the moisture by increasing the desiccant material's temperature is required. This is

accomplished by the second process, the regeneration process. After that, the desiccant material has to be cooled in order to absorb the moisture again.
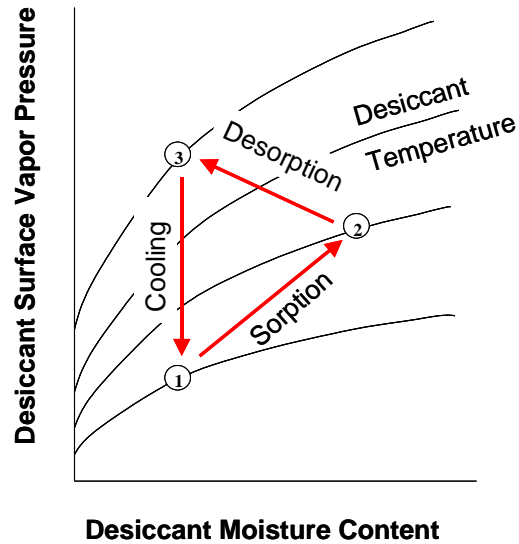
Figure 15: Processes of moisture transfer by desiccant material

The same process can take place inside a close cycle using different working fluid pairs. Adsorption and absorption cycles represents the close thermally driven cooling cycles.

1.3.2.1   Solid Desiccant:

The purpose of the solid desiccant solar cycle is to reduce the moisture content of the ambient fresh air. A typical approach for using solid desiccants for dehumidifying air streams is to impregnate them into a light-weight honeycomb or corrugated matrix that is formed into a wheel. The desiccant wheel rotates slowly between the process and the regeneration airstreams. It is divided into two sections where the process air flows through one section of the wheel to be dehumidified, while a reactivation airstream passes through the other section to regenerate the wheel.

In order to achieve both dehumidification and cooling using solar thermal energy, the desiccant wheel is mostly combined with the evaporative process, Figure 16. The basic process in providing conditioned air can be understood with the aid of Figure 17. The hot and humid process air passes through the rotating desiccant wheel where its dry-bulb temperature increases and its humidity decreases (1-2). Then, the process air is cooled by passing through a heat recovery wheel (2-3). After that, the air is humidified and thus further cooled by a controlled humidifier (3-4) according to the set-values of supply air temperature and humidity. The exhaust air stream of the conditioned space is cooled by evaporative cooling (5-6) and humidified as close as possible to saturation. The state is the one which guarantees the maximum potential of indirect cooling of the supply air stream through the heat recovery exchanger wheel (7-8). Finally, the regeneration air stream is heated for use in regenerating the desiccant wheel, which allows for continuous operation of the dehumidification process.

The COP$_{thermal}$ of a desiccant cooling system is defined as the ratio between the enthalpy change from ambient air to supply air, multiplied by the mass flow, and the external heat delivered to the regeneration heater, Equation (11).

$$COP_{thermal} = \frac{\dot{m}\left(h_{amb} - h_{sup}\right)}{Q_{reg}}$$
(11)

The value of the COP of the desiccant cooling system depends strongly on the conditions of ambient air, supply air and return air. Under normal design conditions, a COP of about 0.7 is achieved and the cooling capacity is in the range of about 5-6 kW per 1000 m^3/h of supply air (Henning, 2007a).
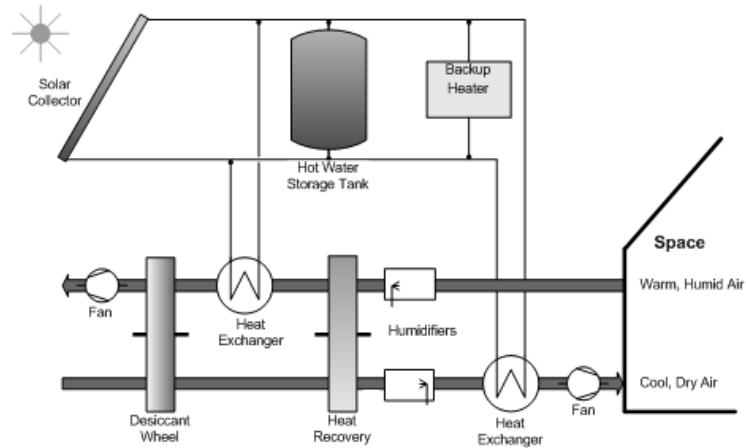
Figure 16: Schematic of a desiccant cooling ventilation cycle (Henning, 2007b)
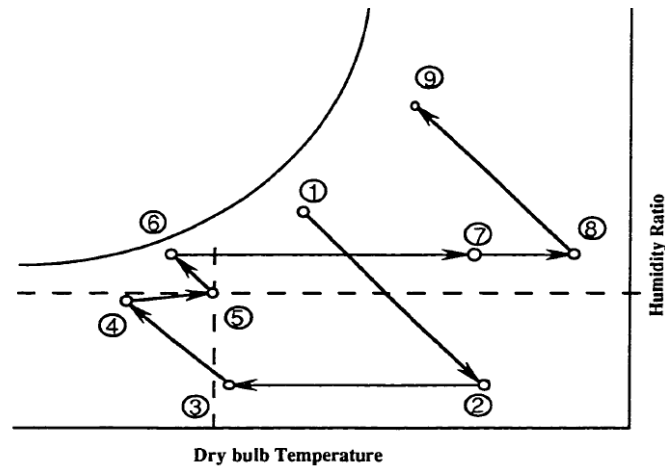
Figure 17: Pennington cycle for cooling and dehumidification

1.3.2.2 Liquid Desiccant:

Liquid and solid desiccants behave in the same principle so that their water vapor pressure is a function of temperature and moisture content. However, they differ in their reaction to moisture. Solid desiccants mostly adsorb the moisture, which means there is no chemical reaction, whereas liquid desiccant materials usually absorb the moisture by undergoing a chemical or physical change.

The system usually consists of a conditioner and a regenerator, Figure 18. In the conditioner, the liquid desiccant is sprayed into the air in order to directly absorb the

moisture from the process air. The liquid falls into a sump to be pumped and sprayed back into the air. While absorbing moisture, the liquid desiccant becomes warmer and its partial vapor pressure increases. In addition, its concentration decreases because of the increase in the water content so regeneration is needed. A small amount of liquid desiccant is taken continuously from the sump to the regenerator to remove the water that is absorbed. The construction of the regenerator is similar to that of the conditioner; the desiccant is also sprayed into the air. The desiccant is heated so that its partial pressure is higher than that of the air. Therefore, the moisture is transported to the regeneration air. As the liquid desiccant solution returns to the sump of the conditioner, it is drier, more concentrated, and still at high vapor pressure and temperature. Therefore, it is cooled to the required temperature by a cooling tower or a chiller before being sprayed into the process air. The favorable feature of the liquid desiccant cycle is the fact that the liquid desiccants can be regenerated at temperatures below 80°C. Typically liquid desiccant working fluids are lithium chloride (LiCl), calcium chloride ($CaCl_2$), and lithium bromide (LiBr).
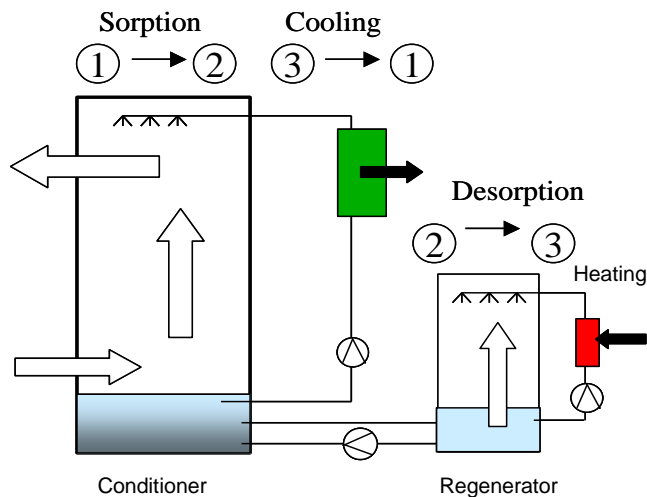
Figure 18: Schematic of a liquid desiccant system

1.3.2.3 Absorption:

Absorption cycles are considered one of the oldest refrigeration technologies. The refrigerant side of the absorption cycle essentially works under the same principle as the vapor-compression cycle. However, the mechanical compressor used in the vapor-compression cycle is replaced by the thermal compressor in the absorption cycle. The thermal compressor consists of the absorber, the desorber, and the solution pump, Figure 19.
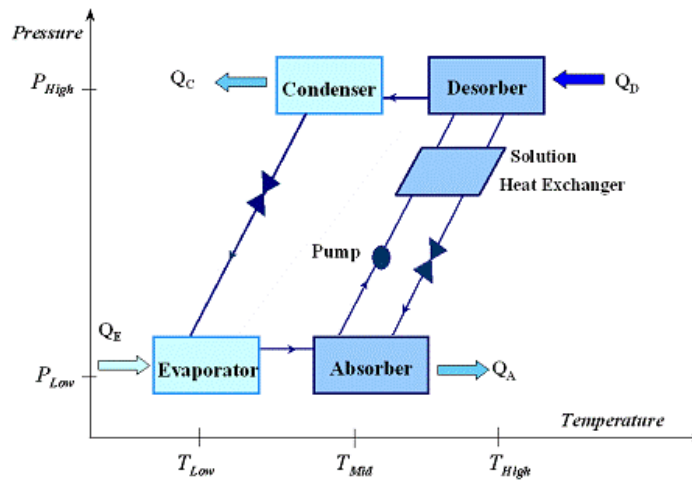
Figure 19: Diagram of an absorption cycle

In the absorber, the absorbent-rich solution is diluted with the refrigerant. During this process, the absorber is cooled in order to keep its pressure in a low level. Then the solution pump increases the pressure of the absorbent/refrigerant mixture to the high pressure level. The power consumption of the solution pump is relatively small compared to that consumed by the mechanical compressor. Since the refrigerant is more volatile than the absorbent, it leaves the solution when adequate heat is added in the desorber. The attractive feature of the absorption cycle is that any types of heat source, including solar heat and waste heat, can be utilized in the desorber. The refrigerant vapor leaves the

26

desorber to be condensed in the condenser, expanded through the expansion device, and evaporated in the evaporator, causing the cooling effect. Then the refrigerant vapor is again absorbed in the absorbent-rich solution.

Typical cooling COPs, Equation (12), of the single-effect, double-effect, and triple-effect absorption cycles are 0.7, 1.2, and 1.7, respectively, (Grossman, 2002). The most common refrigerant-absorbent pairs used in the absorption cycle are water/lithium bromide (H_2O/LiBr) and ammonia/water (NH_3/H_2O). Because the H_2O-LiBr system has a high volatility ratio, it can operate at low pressures and, therefore, at lower generator temperatures. However, the operation of the H_2O/LiBr-based absorption cycle is limited in the evaporating temperature and the absorber temperature, due to the freezing of the water and the solidification of the LiBr-rich solution, respectively. Therefore, they are operated at evaporator temperatures of 5°C or higher (Goswami et al., 2000) and are mostly water cooled. The operation of the NH_3/H_2O-based absorption cycle is not limited in either the evaporating temperature or the absorption temperature. Consequently, the ammonia-water system has the advantage that it can be operated at very low temperatures. A rectifying column after the boiler is required to remove water vapor from ammonia as much as possible which helps prevent ice crystals from forming for temperature much below 0°C. However, ammonia is toxic, a Safety Code Group B2 fluid (ASHRAE standard 34, 1992) and its usage is limited to the large capacity system, which requires mandatory supervision.

$$COP_{thermal} = \frac{Q_{evap}}{Q_{gen}}$$ (12)

27

1.3.2.4   Adsorption:

As depicted in Figure 20, the adsorption cycle is composed of two sorption chambers, an evaporator, and a condenser. The water is vaporized under low pressure and temperature in the evaporator, producing the cooling effect. Then the water vapor enters the sorption compartment where the solid sorbent, such as silicate gel, adsorbs the water vapor. This compartment has to be cooled to accomplish the adsorption process and to reject the heat of adsorption. Simultaneously, in the other sorption compartment, the water vapor is released by regenerating the solid sorbent via heating. The water vapor is then returned to the evaporator after it has been condensed and throttled. By alternating the cooling and heating water between the two compartments, this process can be continuous.

The adsorption cycle typically can achieve a COP of 0.3 to 0.7, depending upon the driving heat temperature. Some of the working fluid pairs that have been used are: Zeolite/water, Activated carbon/methanol, Activated carbon/H_2O and Silica gel/H_2O. Some of the adsorption cycle advantages are the simple mechanical construction and elimination of the crystallization problem. In addition, there is no internal solution pump and electricity consumption is reduced to a minimum. The disadvantages are the comparatively large volume, weight, and high cost.
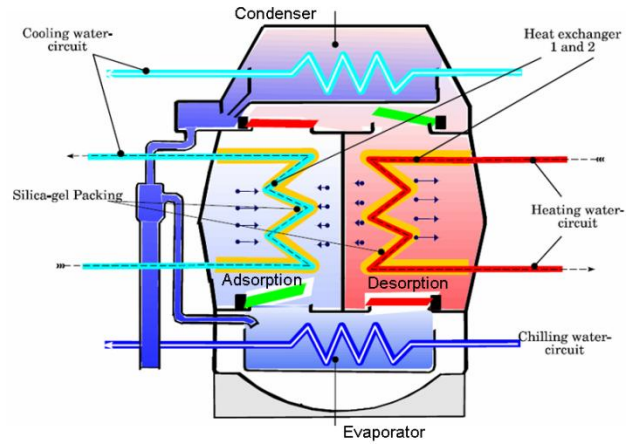
Figure 20: Adsorption cycle (GBU, 1995)

Dieng and Wang (2001), Anyanwu (2003), Sumathy et al. (1999), and Khattab (2006) provided literature reviews of the solar adsorption cooling technologies using various adsorption pairs and their performances. Table 6 summarizes the performance of the solar adsorption cooling technologies using various adsorption pairs as reported by the four authors.

Table 6: Performance of solar adsorption cycles

Adsorption Pair	Cycle COP	System COP (COP_{sr})	Solar Collector	Cycle Conditions	Reference
Activated carbon/methanol	0.43	0.1–0.12	Flat plate (A: 6 m^2)	T_{evap}: −3°C T_{cond}: 25°C T_{gen}: 110°C	Pons and Guilleminot (1986, 1987) Pons and Grenier (1987)
Activated carbon/methanol		0.1–0.12	A: 1 m^2		Boukari et al. (1992)
Activated carbon/methanol		0.1–0.12	A: 0.9 m^2	T_{evap}: −6°C T_{gen}: 70°C–78°C	Sumathy and Zhongfu (1999)
Activated carbon-35 methanol		0.16			Passos et al. (1989)
Domestic charcoal/ methanol		0.14–0.16			Khattab (2004, 2006)
$SrCl_2/NH_3$		0.05–0.08			Erhard et al. (1998)
Activated carbon/NH_3	0.25	0.05			Critoph (1993)
Activated carbon/H_2O	0.39	0.07	A: 2 m^2		Wang et al. (2000)
Zeolite/H_2O	0.8	0.10–0.12	Flat plate (A: 1.5 m^2)		Tchernev (1979), Pons and Guilleminot (1986, 1987)
Zeolite/H_2O		0.11	A: 20 m^2	T_{evap}: 1°C T_{cond}: 30°C T_{gen}: 118°C	Grenier et al. (1988)
Silica gel/H_2O		0.16			Hildbrand et al. (2004)
Silica gel/H_2O		0.10–0.13			Luo et al. (2007)
Silica gel/H_2O		0.2–0.3	Vacuum tube (A: 170 m²)		Henning and Glaser (2003)

1.3.2.5 Ejector Cycle:

The steam ejector cycle represents the thermo-mechanical cooling system. Figure 10 illustrates the steam ejector cycle which consists of three heat exchangers, a pump, an expansion valve and an ejector. The refrigerant is converted to a high pressure vapor in

the generator and is passed through the ejector. In the ejector, the refrigerant is accelerated creating a pressure lower than that of the evaporator. During this process, the refrigerant vaporizes in the evaporator by absorbing heat, causing cooling effect, and migrates to the ejector. The two streams are mixed creating one stream at intermediate pressure. Then, the vapor is condensed and separated to be sent to the high and low pressures of the cycle using a pump and an expansion valve, respectively.

Most of the steam ejector cycle requires steam at pressures in the range of 0.1–1 MPa, and temperatures in the range of 120°C–180°C (Huang et al. 1985; Badawy 1998). However, Loehrke (1990) proposed and demonstrated that the steam ejector cycle could be operated using low-temperature solar heat by reducing the operating pressure under atmospheric pressure. Khattab and Barakat (2002) later proved this concept by developing a detailed mathematical model of the solar steam ejector cycles operating at low pressure and low temperature for the air-conditioning application.
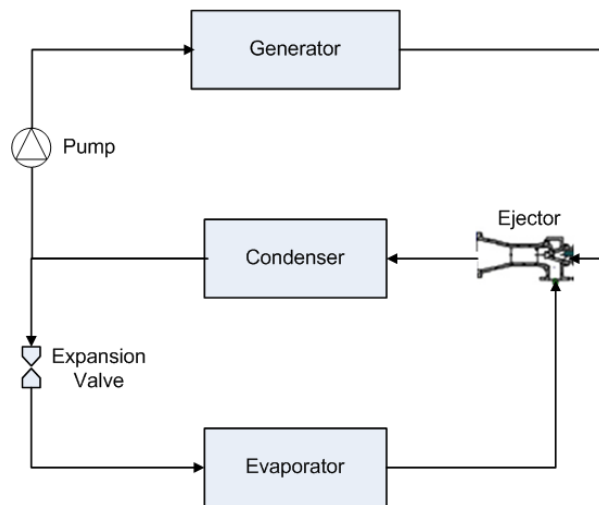
Figure 21: Steam Ejector Cycle

Table 7 summarizes the performance and several working fluids suggested for the solar ejector cycle.

Table 7: Summary of the solar ejector cycles

Working Fluid	Overall COP	Ejector Cycle COP	Solar Collector	Conditions	Reference
R-113	N/A	0.42	N/A	T_{gen}: 87.1°C, T_{evap}: 18°C, T_{cond}: 42.3°C	Nehad (1998)
R-141b	0.22	0.5	A: 68 m^2 η_{sc}: 0.5	T_{gen}: 95°C, T_{evap}: 8°C Incident solar radiation: 700 W/m^2	Huang et al. (1998)
R-141b	0.19–0.28	0.31 – 0.52	η_{sc}: 0.39–0.54	T_{gen}: 85°C–95°C, T_{evap}: 8°C, T_{cond}: 32°C Incident solar radiation: 700 W/m^2	Huang et al. (2001)
R-141b	N/A	0.39	A: 80 m^2 η_{sc}: 0.2	T_{gen}: 80°C, T_{evap}: 8°C, T_{cond}: 32°C Hot storage tank volume: 4 m^3	Vidal et al. (2006)
R-142b	0.11	0.21 (annual average) 0.34 (max)	η_{sc}: 0.52	T_{gen}: 105°C, T_{evap}: –10°C, T_{cond}: 30°C	Dorantesa et al. (1996)
R-142b	0.13–0.65	0.32–1.52	η_{sc}: 0.39–0.42	T_{gen}: 100°C–106°C, T_{evap}: 4°C, T_{cond}: 50°C	Arbel and Sokolov (2004)
Isobutane	0.22	0.48	A: 50 m^2 η_{sc}: 0.48	T_{gen}: 70°C–120°C, T_{evap}: 15°C, T_{cond}: 5°C + T_{amb} Hot storage tank volume: 2 m^3	Pridasawas and Lundqvist (2007)
Water	N/A	0.18 – 0.59	N/A	T_{gen}: 120°C–140°C, T_{evap}: 5°C–10°C, T_{cond}: 26.5°C–36.3°C	Eames et al. (1995)
Water	N/A	0.53	N/A	T_{gen}: 110°C–120°C, T_{evap}: 7°C–12°C, T_{cond}: 30°C–40°C	Grazzini and Rocchetti (2002)

1.4   Solar Air Conditioning in Hot and Humid Climates

It is very important to consider the ambient conditions and the types of loads when designing an air conditioner (A/C). Regardless of the climate zone, the temperature and humidity have to be controlled in order to maintain space comfort conditions. In hot and humid regions, removal of moisture from the air using conventional air conditioners represents a considerable portion of the air conditioning load. Conventionally, air conditioning systems have to lower the air temperature below its dew point to accomplish dehumidification. This approach makes the compressor operate at higher pressure ratio, hence reducing the cycle coefficient of performance (COP). In addition, an auxiliary

heater might be required to sensibly heat the air before it is supplied to the conditioned space.

Desiccant assisted air conditioners offer a solution to meet the humidity and temperature requirements of buildings via decoupling latent and sensible loads. Extensive studies have been carried out on desiccant air conditioners. These studies focus mainly on two key aspects: improving desiccant materials' performance and innovative system configurations. The first aspect involves the modification of conventional desiccant materials (Chung and Chung, 1998; Knez and Novak, 2001; Yano and Yoshiaki, 2003) and the fabrication of new desiccant materials (Ladisch, 1997; Beery and Ladisch, 2001; Mathiowitz et al., 2001; Khedari et al., 2003; Jia et al., 2006). The second aspect involves the modification of the basic rotary desiccant air conditioner introduced by Pennington (1955), as illustrated in Figure 22. For example, the ambient air can be used in the regeneration side of the cycle and return air can be re-circulated with no fresh air back up to provide the so called recirculation cycle (Waugaman et al., 1993). Another heat exchanger could also be added to the recirculation cycle as in Dunkle cycle (Dunkle, 1965). The common feature of these cycles is that evaporative cooling is used to handle the sensible heat. This requires the process air stream to be over-dried in order to permit its cooling using the evaporative cooling process. This motivates the introduction of the desiccant assisted VCC air conditioners where the latent load is handled by the desiccant wheel and the sensible load is handled by the VCC. The performance of various desiccant air conditioners operating under different conditions has been investigated as shown in Table 8. One can notice that studies on the desiccant A/Cs focus mainly on silica gel. In

addition, the studies where VCCs are used do not have detailed analysis of the operation

of the VCC.
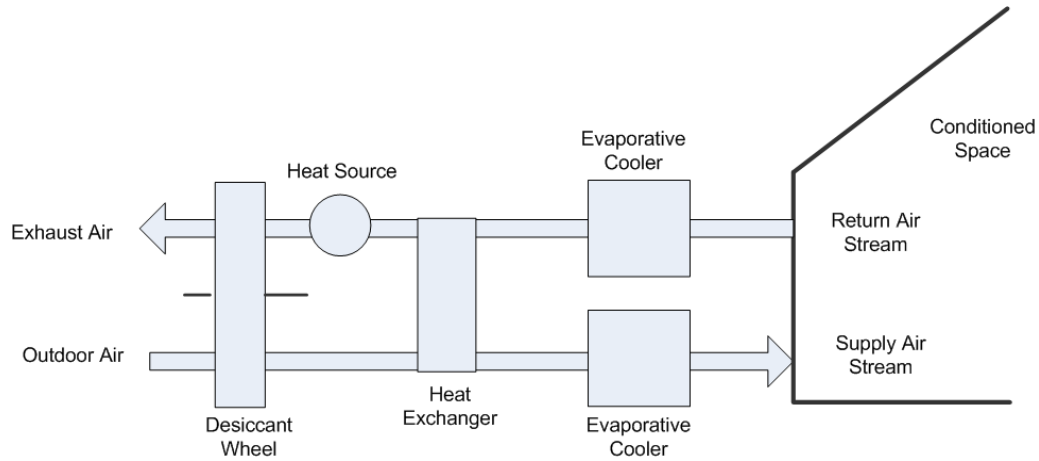
Figure 22: Pennington cycle

Table 8: Investigations of the performance of the desiccant air conditioner

Authors	Exp.	Sim.	System	Desiccant	Conditions	Results
Kodama et al., 2001	✓		DW+SW+EC	Silica Gel	T-reg = [60-140] ^{o}C ω_dw = [1-19] RPH Ts = [18-27] ^{o}C ws = [4.4-13.8] gw/kga	Optimal Speed
Ge et al., 2008	✓		DW+SHX+EC Two-stage DW ARI summer and humid conditions	Silica Gel	t-dw = [40,70,100]mm T-reg = [50-90] ^{o}C ω_dw = [2-20] RPH V*=[360] m^3/hr T-return = [26.7]^{o}C w-return =[11.1]gw/kga	MR COP_{th}
Enteria et al., 2010	✓		DW+SHX+EC	Silica Gel	T-amb = [30]^{o}C R-amb=[60]% V*=[200] m^3/hr T-return = [26]^{o}C Rh-return =[55]% T-reg= [60-75] ^{o}C	COP
Panaras et al., 2010	✓	✓	DW+SW+EC	Silica Gel	T-amb = [24-40]^{o}C w-amb=[4-14]gw/kga T-reg = [50-80]^{o}C w-reg=[3-15]gw/kga V*=[600-1200] m^3/hr	COP

Enteria et al., 2010	✓		DW+SW	Silica Gel	T-amb = [30]°C w-amb=[16]gw/kga T-return = [26]°C w-return=[12]gw/kga ω_dw = [5-90] RPH T-reg = [60-80]°C V*=[100-200] m³/hr	MRC COP_{latent} $COP_{sensible}$ COP_{total}
Antonellis et al., 2010	✓	✓	DW	Silica Gel	T-amb = [18-27]°C w-amb=[4.3-13.8]gw/kga ω_dw = [2-28] RPH T-reg = [60-140]°C	MRC Optimal - Config.
Heidari et al., 2010	✓	✓	DW+SW+EC	Silica Gel	ω_dw = [12-96] RPH T-reg = [60-120]°C	COP [sim] T_{supply} [sim]
Enteria et al., 2010	✓		DW+SHX+EC	Silica Gel	T-amb = [30]°C w-amb=[16]gw/kga T-return = [26]°C w-return=[12]gw/kga T-reg = [60-75]°C V*Sup=[200] m³/hr V*Return=[100] m³/hr	COP
Subra-manyam et al., 2004	✓		DW + VCC DW around the VCC's evaporator	Metal Silicate	V*=[250-750] m³/hr T-amb = [32]°C R-amb=[65]% T-return = [26]°C Rh-return =[65]%	MRC P-suction P-discharge COP_{vcc}
Ghali, K., 2008		✓	DW+SHX+VCC	Silica Gel	t-dw = [200]mm	Economic feasibility
Jeong et al., 2010	✓	✓	DW [exp] Four-partition wheel DW+VCC [sim]	Silica Gel	T-amb = [28]°C w-amb=[16-22]gw/kga T-inter = [14-26]°C ω_dw = [1-17] RPH V*=[30-130]m³/hr T-reg = [40-60]°C	Δω Outlet temp. T_{evap} [sim] P_{Comp} [sim] COPvcc

Evaporative Cooler = EC

Sensible Wheel = SW

Desiccant Wheel = DW

Vapor Compression Cycle = VCC

Moisture Removal = MR

Moisture Removal Capacity = MRC

Sensible Heat Exchanger= SHX

1.5   Summary of Background and Literature Review

There are two common ways of utilizing solar energy in air conditioning (A/C) applications. One is to convert the solar radiation to electricity and use an electrically driven A/C. The other is to convert the solar radiation to thermal energy and use a thermally driven A/C. In the first approach, the low efficiency of solar radiation conversion to electricity, typically 10-15%, results in a low overall system COP. In the second approach, the low COP of the thermally driven cycles, Table 9, leads to a low overall system COP. These bottle necks results in an overall system COP less than unity for both approaches. A comparison of possible combinations of the solar technologies with the cooling processes is shown in Figure 23. It has to be mentioned that typical values for the collectors' efficiencies and cycles' COP are used in this comparison and does not necessarily represent state of the art technologies. The purpose is to obtain a conservative value of the overall system COP. In addition, the residential and small commercial application has to be kept in mind when selecting the performance values of the solar air conditioners.

Table 9: Overview of the thermally driven cooling cycles

Process Type	Closed		Open		Thermo-mechanical
Cycle	Adsorption cycle	Absorption cycle	Solid desiccant	Liquid desiccant	Ejector cycle
Sorbent type	Solid	Liquid	Solid	Liquid	—
Working fluids (refrigerant/ sorbent)	H_2O/silica gel	H_2O/LiBr; NH_3/H_2O	H_2O/silica gel; water/LiCl/ cellulose	Water/CaCl$_2$; Water/LiCl	Steam, FC
Thermal COP	Average 0.59	0.50–0.73 (single stage) <1.3 (two stage)	0.51	0.74	0.85
Typical operating temperature	53°C–82°C	<97°C (most) 60°C–110°C (single stage) 130°C–165°C (two stage)	45°C–95°C	67°C	118°C
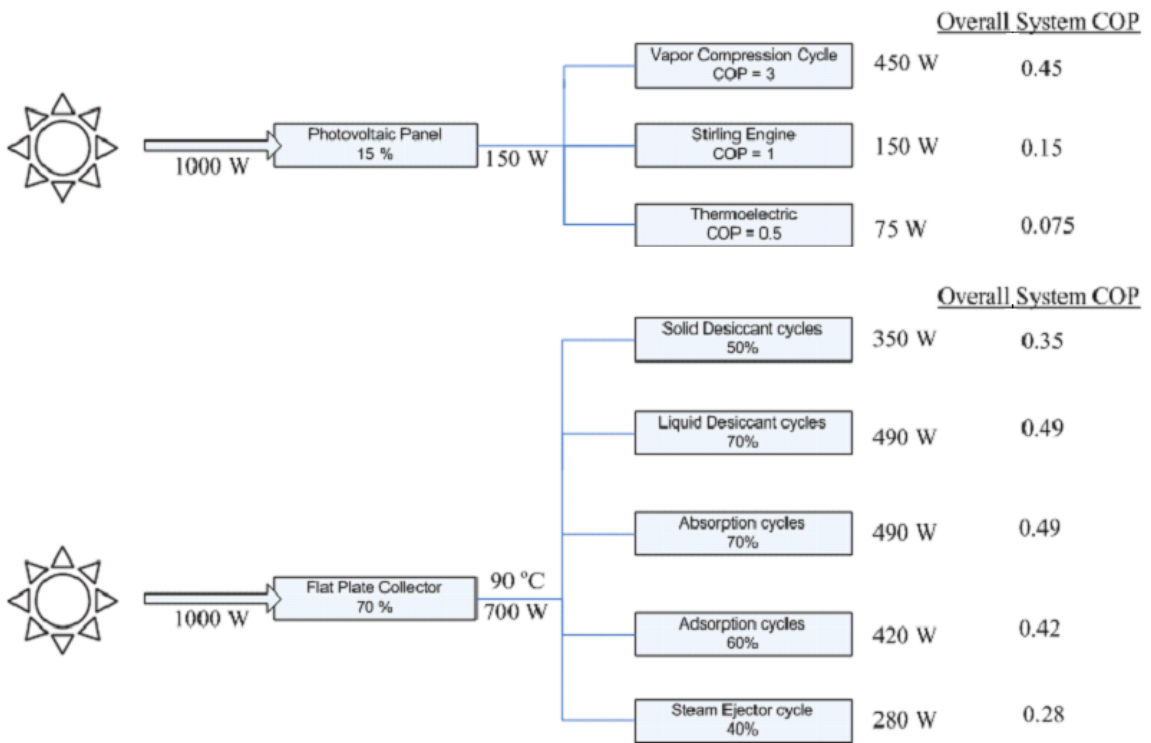
Figure 23: Various combinations between solar collectors and cooling processes

The review of the pertinent literature shows that not only there is a limitation on the literature available on CPVT, but also their applications. There have been a few attempts to utilize the thermal output in applications other than domestic water heating. The

literature review also shows that whether the solar electric A/C or the solar thermal A/C is selected, the overall system COP is less than unity. This indicates that there is a need to investigate innovative approaches.

1.6   Research Objectives

The objective of this thesis is to search for an efficient way of utilizing solar energy in air conditioning applications. The solar air conditioner is intended to be used for residential and small commercial buildings. The solar air conditioner is required to maintain acceptable indoor conditions. It is also required to operate under very hot and humid conditions with a high coefficient of performance. Thus, this work consists of modeling, experimental, and post analysis tasks to find the high performance innovative solar A/C configuration.

Conceptual and Modeling Tasks:

- Select the most suitable air conditioning technology based on the air conditioning loads
- Select the most appropriate solar collector based on the geographical location and type of air conditioner
- Establish a model to predict the performance of the proposed solar air conditioner

Experimental tasks

- Design and construct a test facility
- Measure the performance of the selected cooling sub-system under various operating conditions

Post Analysis Tasks

- Validate the simulation model using the experimental data
- Optimize the system's performance and total cost

1.7   <u>Thesis Structure</u>

The thesis starts with the fundamentals of solar radiation, which are essential information required for any solar driven system. Then, the available solar collection technologies and solar cooling processes are discussed. The pertinent literature is reviewed while focusing on hot and humid conditions. After that, the background information and literature review is summarized in order to identify the challenges and gaps in solar air conditioning. In Chapter 2, the novel hybrid solar air conditioner, which addresses the weaknesses of the current solar air conditioners, is presented. Chapter 3 describes the different system components and their simulation models. The proposed system model is used in a parametric study to identify the important design variables that affect the system performance. Then, it is used to compare the novel hybrid solar conditioner to the most common solar air conditioner. The experimental investigation is discussed in Chapters 4 and 5. Chapter 4 focuses on the desiccant wheel cycle investigation, which includes the desiccant wheel, enthalpy wheel, and the water-air heat exchanger. In Chapter 5, the vapor compression cycle and the conditioned space is added to the experiment. Chapter 6 investigates the various optimization algorithms to minimize the cost and the energy consumption of the proposed hybrid solar air conditioner. The gathered experimental data, presented in Chapters 4 and 5, is used to validate the models discussed in Chapter 2. New components models are discussed and validated in order to simulate the actual components used in the experiment.   The thesis concludes with a list of major contributions and recommendations for future work.

2. The Novel Hybrid Solar Air Conditioner

2.1   **The Design Approach**

In order to design a solar air conditioner, one has to take into consideration the meteorological conditions, the types of solar collectors available, the conditioned space loads, and the type of the solar air conditioner. As previously mentioned, both approaches that are used for solar air conditioning have limitations in their coefficient of performance and degrades when handling sensible and latent loads simultaneously. Therefore, the purpose of a new design should solve these two problems while maintaining the acceptable comfort conditions inside the conditioned space. This lead to the idea of using a hybrid solar collector to drive a hybrid air conditions that control the temperature and humidity separately.

The novelty of this design is to use a concentrated photovoltaic/thermal (CPVT) collector to drive a thermally and an electrically driven cycles for air conditioning application, simultaneously. A desiccant wheel cycle (DWC), which is driven by the thermal output of the collector, is used to accommodate the latent load. A vapor compression cycle (VCC), which is powered by the electric output of the collector, is used to accommodate the sensible load.
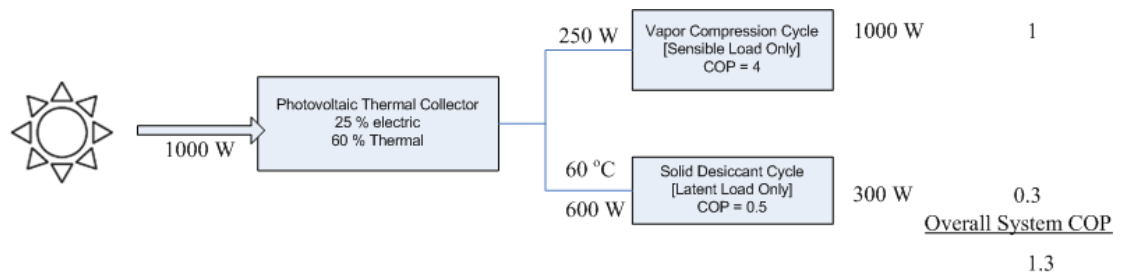
Figure 24: COP of the proposed hybrid solar air conditioner

Figure 24 shows the proposed system's overall COP that could be achieved by coupling the CPVT collector with the two selected cooling processes. The high COP is attributed to both the solar sub-system and the cooling sub-system. The photovoltaic cells are operated under concentration and cooled by forced convection. This allows the PV cells to operate at high efficiency and increases their electric output. Therefore, the PV efficiency and electrical output is higher than that of a photovoltaic panel shown in Figure 23. However, the thermal output of the collector is lower than that of a flat plate collector as shown in Figure 23. That is due to the presence of PV cells which have lower solar radiation absorptivity than a blackened flat plate and represent an additional thermal resistance. In the cooling sub-system, operating the DW to only handle the latent load and operating the VCC to only handle the sensible load, allows each cycle to operate at its most preferable conditions. The DW does not have to over-dry the process air stream to allow its cooling using evaporative coolers. In addition, the VCC does not have to operate at lower evaporator temperature in order to condense the moisture out of the supply air stream. Since the VCC only handling the sensible load, its size can be reduced. This addresses one of the most common problems in hot and humid climates which is over-sizing the VCC to handle both latent and sensible loads. Operating the VCC at higher evaporator temperature also reduces the pressure ratio across the compressor, hence increases its efficiency.

2.2   The Solar Sub-System

The system is divided into two main sub-systems: a solar sub-system and a cooling sub-system. The solar sub-system consists of the solar collectors, a thermal storage, an electrical storage, an inverter, controllers and a regulator to distribute DC power from the

collector array to/from the battery array. The solar sub-system is depicted in Figure 25. As the figure shows, storage for each form of the energy outputs of the collector is used. The main purpose of these storages is to serve as a buffer reservoir to provide nearly constant outputs. An electric heater is also used to ensure that the temperature supplied to the desiccant wheel is sufficient for regeneration.
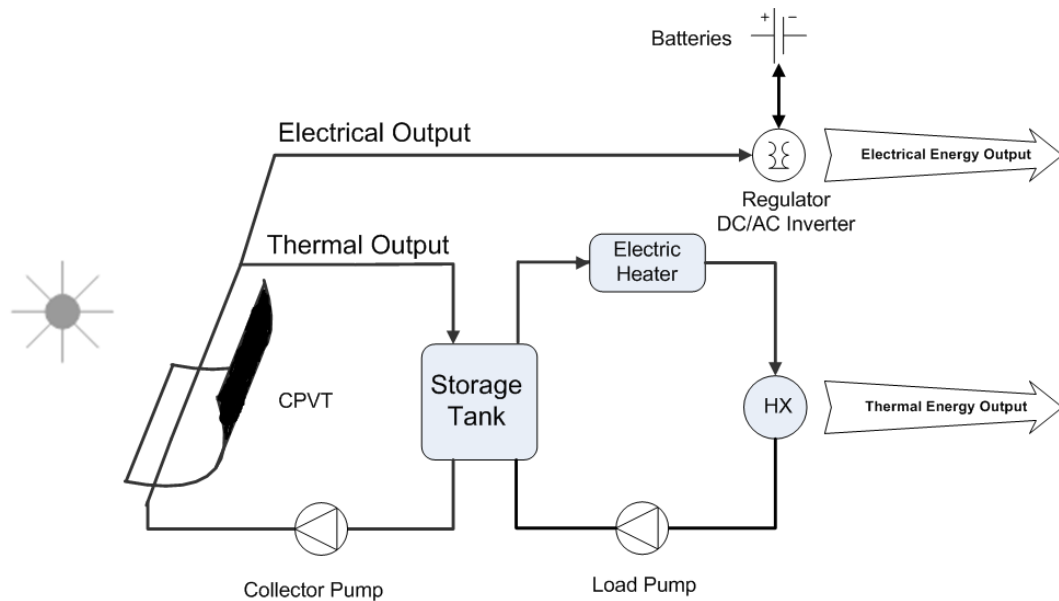
Figure 25: The solar sub-system

2.3   The Cooling Sub-System

The cooling sub-system includes the VCC, DW, an Enthalpy Wheel (EW), the conditioned space and the required fans and controllers, as shown in Figure 26. The conditioned space in this study represents a residential home. As indicated by the figure, the thermal output of the solar sub-system is used to regenerate the DW by heating the building exhaust air stream in the water-air heat exchanger (WAHX). Moreover, the electrical output of the solar sub-system is used to drive the sensible VCC. This hybrid air conditioner separates the latent and sensible loads where the latent load is accommodated

in the DW and the sensible load is dealt with in the VCC. Separating the latent and sensible loads allow the VCC to operate at higher evaporating temperature since no dehumidification is required. Even though the liquid desiccant open cycles are preferred to the solid desiccant ones in terms of thermal Coefficient of Performance (COP) , a DWC is selected in this study. The main reason is that the DWC can be operated using low heat source temperatures which eliminate the need to operate the solar sub-system at high temperatures that could degrade the performance of the PV cells. It is also more compact, and less subject to corrosion.

The figure also shows that part of the air leaving the building is ducted to the DWC to be exhausted while the remaining air is re-circulated to be mixed with the fresh preconditioned air. In order to utilize the conditioned exhaust air stream, the EW is used to sensibly cool the hot and dry supply air leaving the DWC and reduce the sensible load on the VCC. The EW also pre-heats the exhaust air stream reducing the amount of heat needed at the WAHX. The cooling sub-system is coupled with the solar sub-system to construct the complete hybrid solar air conditioner as shown in Figure 27.
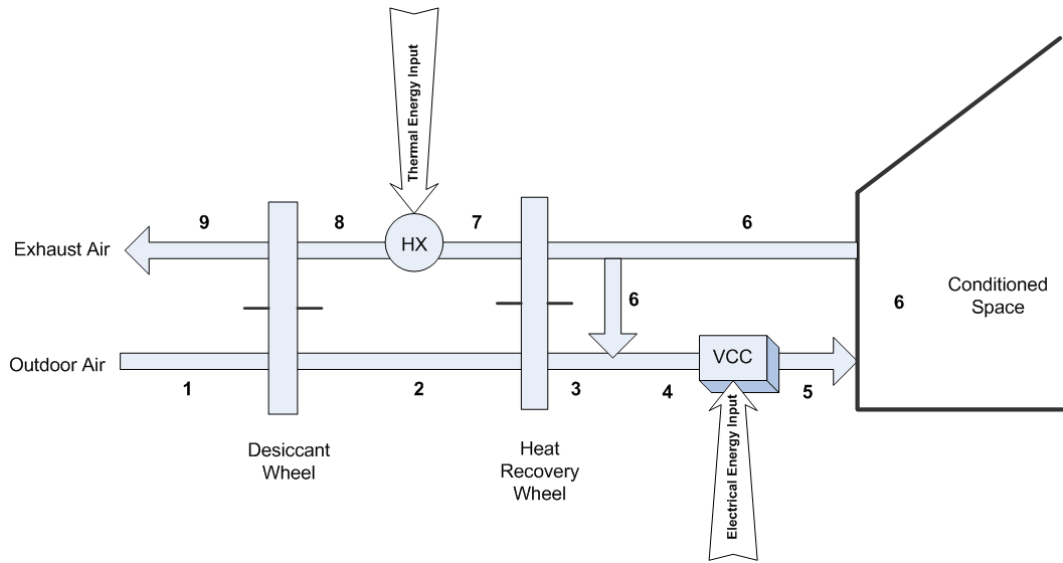
Figure 26: The cooling sub-system
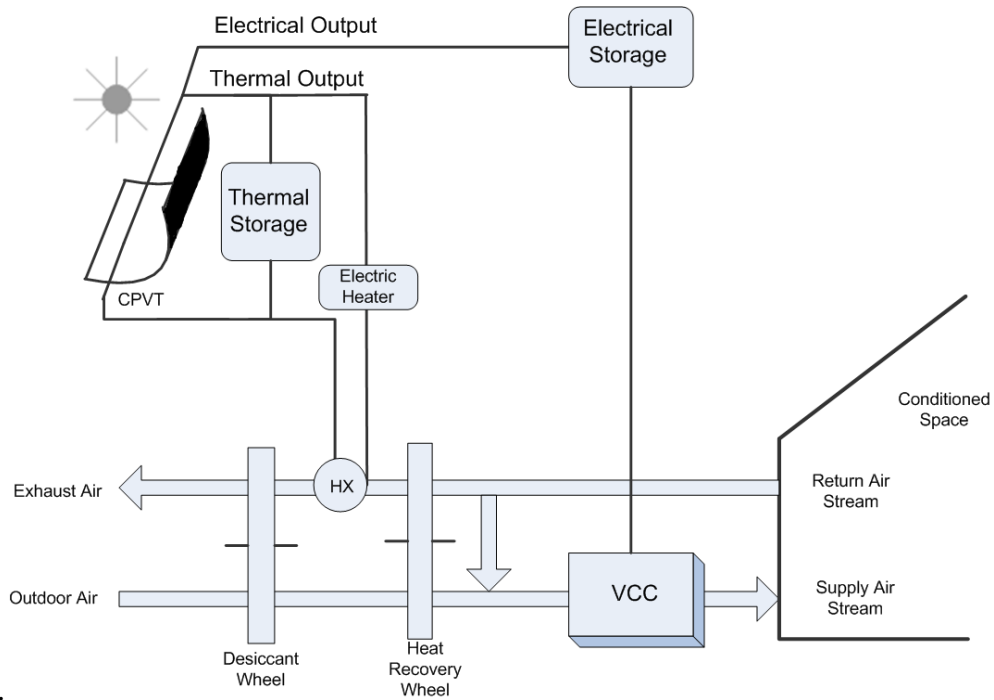
Figure 27: Schematic of the hybrid solar cooling system.

3. Simulation of the Hybrid Solar Air Conditioner

3.1   **Modeling Approach**

Modeling the hybrid solar conditioner involves modeling various mechanical, thermal, and electrical components. Therefore, the transient systems simulation (TRNSYS) program is selected to facilitate this task. TRNSYS program is a widely used modular thermal process simulation program (Duffie and Beckman, 1991; Zhai and Wang, 2009). TRNSYS has a library of subroutines, called TYPEs, which model the system components. In order to construct the complete system, these TYPEs have to be linked together. Therefore, it is useful to construct an information flow diagram for the system to facilitate the identification of the various components used and the flow of information between them. The information flow diagram for the hybrid solar air conditioner is created as shown in Figure 28.
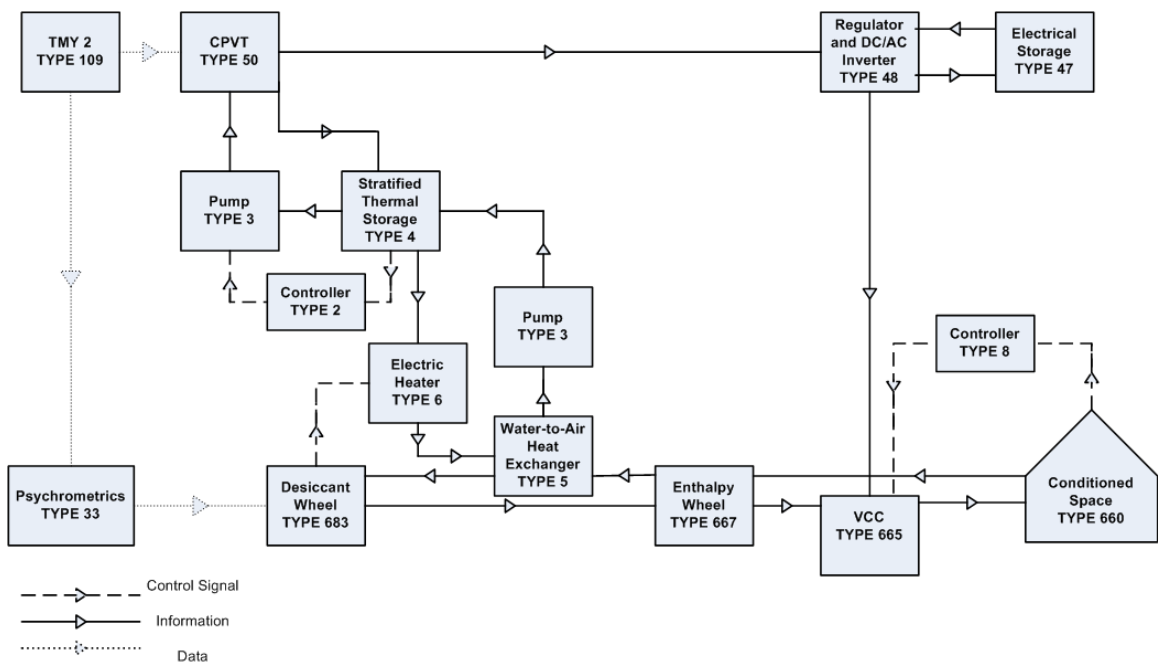
Figure 28: System information flow diagram.

The modeling approach is shown in Figure 29. By calculating the supplied electrical and thermal energies and the air conditioner required heat and power, the solar fraction for each form of energy can be calculated. A thermal solar fraction (TSF) and an electrical solar fraction (ESF) can be calculated by using Equations (13) and (14), respectively.

$$TSF = \frac{Q_{provided}}{Q_{required}} = 1 - \frac{Q_{external}}{Q_{required}} \tag{13}$$

$$ESF = \frac{P_{provided}}{P_{required}} = 1 - \frac{P_{external}}{P_{required}} \tag{14}$$
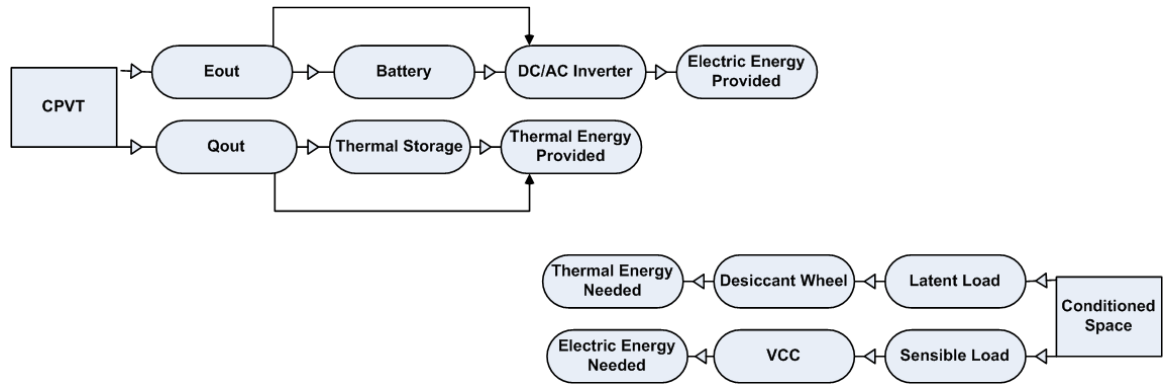
Figure 29: Modeling approach.

The CPVT collector is modeled based on the work of Evans et al., (1978). The thermal output is modeled by modifying the Hottle-Whillier-Bliss equation, which is commonly used for solar thermal flat plate collectors, Equation (15).

$$Q_{Coll_{out}} = A_a \widetilde{F_R} \left[G\ (\tau\alpha) - \frac{\widetilde{U_L}}{C}(T_{F,i} - T_{amb}) \right] \tag{15}$$

The electrical output of the CPVT is calculated using Equation (16)

$$P_{Coll_{out}} = P_r[1 + \beta(T_c + T_r)] \tag{16}$$

The thermal storage is modeled using a stratified cylindrical storage tank with 10 nodes. The temperature of each node is determined by applying an energy balance, Equation (17).

$$m_i \frac{dT_i}{dt} = \left(\frac{UA}{C_p}\right)_i (T_{amb} - T_i) + F_i^S \dot{m}_s (T_s - T_i) + F_i^L \dot{m}_L (T_L - T_i)$$
$$+ \begin{cases} \dot{m}_i (T_{i-1} - T_i) & if \ \dot{m}_i > 0 \\ \dot{m}_{i+1}(T_i - T_{i+1}) & if \ \dot{m}_{i+1} < 0 \end{cases} \tag{17}$$

F is the source/load control function used to determine which node receives the input liquid (Duffie and Beckman, 1991). The electrical storage used is an array of lead acid batteries. The charging and discharging of the batteries is described by the Shepherd model.

Moreover, the VCC is modeled based on a commercially available 17.5 kW air conditioning unit using R-410A (Trane, 2008). The manufacturer's data for heating and cooling are arranged in a format that TRNSYS can recognize. The VCC is sized based on ASHRAE 1% design conditions for Abu Dhabi, U.A.E., Table 10 (ASHRAE, 2001). The COP of the VCC (COP$_{VCC}$) can be defined as shown in Equation (18).

$$COP_{VCC} = \frac{Q_{Evap}}{P_{Comp} + P_{fan,Cond} + P_{fan,Evap}} \tag{18}$$

Table 10: ASHRAE design conditions for Abu Dhabi, U.A.E.

Air Conditioning (1%)		Desiccant Cooling (1%)	
DB	42.5°C	DP	28.8°C
MWB	23.4°C	W	0.025 kg$_w$/kg$_a$
		MDB	32.8°C

In addition, the DWC is sized using ASHRAE 1% design conditions for Abu Dhabi, shown in Table 10. The desiccant material used in the DW is silica gel. The performance

of the DW is based on the F_1-F_2 iso-potential lines method. These iso-potential lines are functions of the wheel's inlet temperatures and humidity ratio, Equations (19) and (20). The outlet conditions of the supply air can be calculated using the effectiveness for each line, Equations (21) and (22). The values of η_{F1} and η_{F2} used in this simulation are 0.08 and 0.95, respectively. The state numbers refer to the moist air conditions at state points shown in Figure 26.

$$F_{1,k} = -\frac{2865}{(T_k + 273.15)^{1.49}} + 4.344(W_k)^{0.8624} \tag{19}$$

$$F_{2,k} = \frac{(T_k + 273.15)^{1.49}}{6360} - 1.127(W_k)^{0.07969} \tag{20}$$

$$\eta_{F1} = \frac{F_{1,2} - F_{1,1}}{F_{1,8} - F_{1,1}} \tag{21}$$

$$\eta_{F2} = \frac{F_{2,2} - F_{2,1}}{F_{2,8} - F_{2,1}} \tag{22}$$

In this simulation, the humidity ratio of the supply air leaving the DW is specified and then the required regeneration temperature is calculated. Figure 30 shows the performance of the DW for the month of June using Abu Dhabi's Typical Meteorological Year (TMY2) data. The backup heater is activated when the tank temperature is not sufficient to regenerate the DW. The COP of a desiccant wheel (COP_{DWC}) can be defined as the ratio of the latent load removed to the heat delivered to the water-air HX, as given by Equation (23):

$$COP_{DWC} = \frac{\dot{m}h_{fg}(W_1 - W_2)}{\dot{Q}_{reg}} \tag{23}$$

The EW is modeled based on the constant effectiveness method, Equation (24).

$$Q_{EW} = \varepsilon \, C_{min}(T_6 - T_2) \tag{24}$$

where C_{min} is the minimum heat capacity rate of the two streams entering the EW. The sensible effectiveness used in the simulation is 0.75.
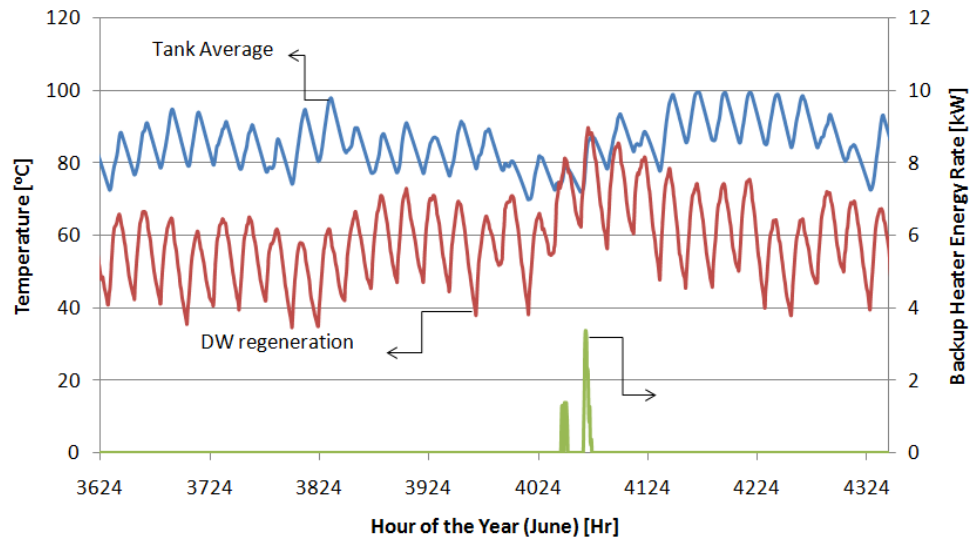
Figure 30: Simulated performance of the DW for the month of June

The performance of the cooling sub-system is simulated at T_{amb} = 45°C and w_{amb} = 15 gw/kga. Figure 31 shows the psychrometric processes with state points corresponding to the states indicated in Figure 26.
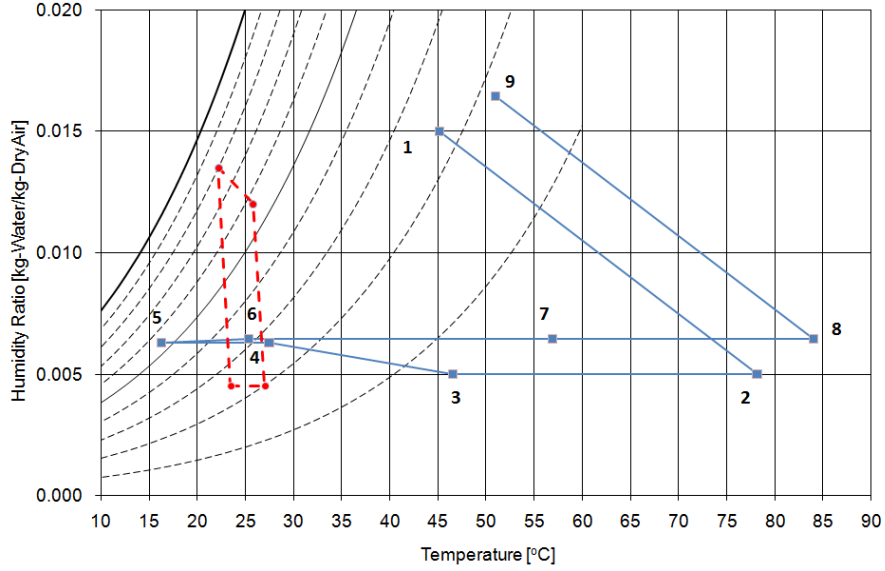
Figure 31: Air state points in various locations in the cooling sub-system.

The complete system COP can be defined as shown in Equation (25). The COP is defined as the total air conditioner capacity, sensible and latent, divided by the total energy input into the system.

$$COP = \frac{Q_{VCC} + Q_{DWC}}{G_d A_a + P_{grid} + Q_{heater}} \tag{25}$$

The overall performance of the hybrid air conditioner is compared to two solar driven air conditioners, a VCC driven by PV panels and an absorption cycle (ABS) driven by Evacuated Tubes (ETC). The COPs of these systems are defined by Equation (26) and (27).

$$COP_{ETC+ABS} = \frac{Q_{cooling}}{G_{tot} A + Q_{heater}} \tag{26}$$

$$COP_{PV+VCC} = \frac{Q_{cooling}}{G_{tot} A + P_{grid}} \tag{27}$$

50

3.2   <u>Parametric Study</u>

A Typical Meteorological Year 2 (TMY2) data file is used to obtain the solar irradiance and various weather conditions for Abu Dhabi (Meteonorm, 2007). The initial configuration of the solar sub-system consists of a 1 m^3 hot water storage tank and 12 batteries. The initial operation conditions are a water mass flow rate (MFR) through the collectors array of 1,800 kg/hr and water MFR through the water-air heat exchange of 1,500 kg/hr.

The water MFR through the collector array is varied to investigate its effect on the thermal and electrical outputs. It has to be noted that, in PVT system applications, the production of electricity is the main priority. Figure 32 shows that as the water MFR through the collector array increases, the thermal output decreases and the electrical output increases until both reach a nearly constant values. As the water MFR increases, the increase in the water temperature across the collector decreases, which leads to lower PV cells temperature. The lower the PV cell temperature, the higher the efficiency, hence the electricity production.
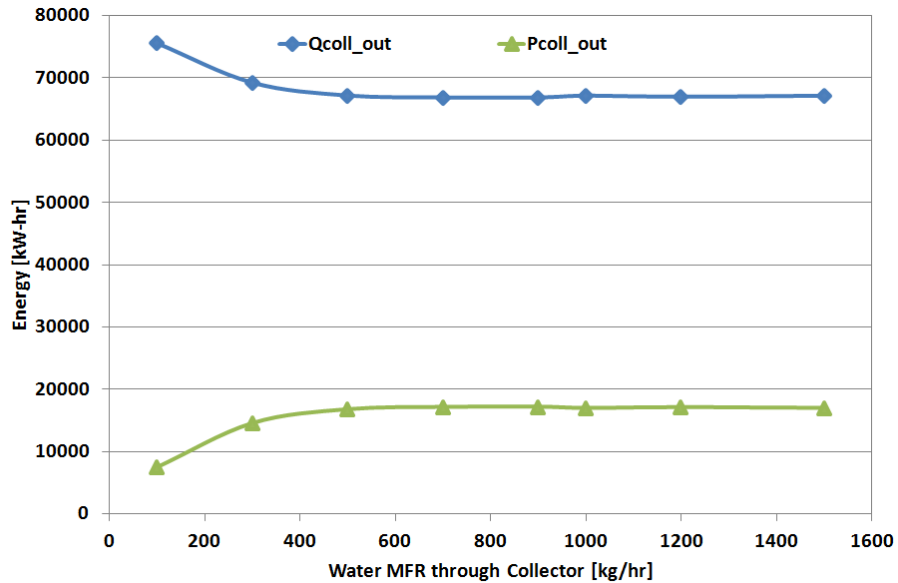
Figure 32: The effect of the collector MFR on its outputs.

The volume of the hot water storage tank is varied to investigate its effect on the collector outputs and the amount of energy delivered to the DWC through the WAHX. As indicated by Figure 33, the collector electrical and thermal outputs are not affected. However, the amount of energy delivered to the DWC increases with increasing thermal storage size. The results show that increasing the thermal storage volume beyond 2 m^3 does not have significant effects on the energy delivered to the DWC.
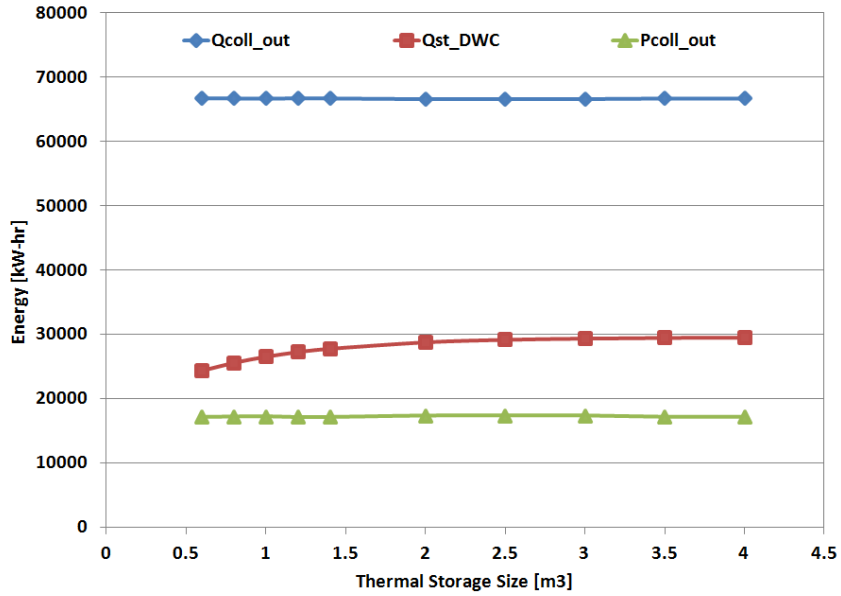
Figure 33: Thermal storage size vs. energy delivered.

Two power conditioning devices are used for the collector's electrical output. The first one is a regulator, which distributes DC power from the collector array to/from the battery banks. The second device is the inverter which converts the DC power to AC to be used by the VCC. These two components are represented by a TRNSYS TYPE 48 as shown in Figure 28. Based on the VCC required energy, TYPE 48 will decide on whether to use the collector output or the grid. The priority is given to utilizing the electrical output of the collector directly to drive the VCC and the surplus is directed to charge the batteries. Figure 34 shows the effect of increasing the electrical storage size on the electrical energy needed from the grid. As the number of batteries increases the needed grid energy decreases.
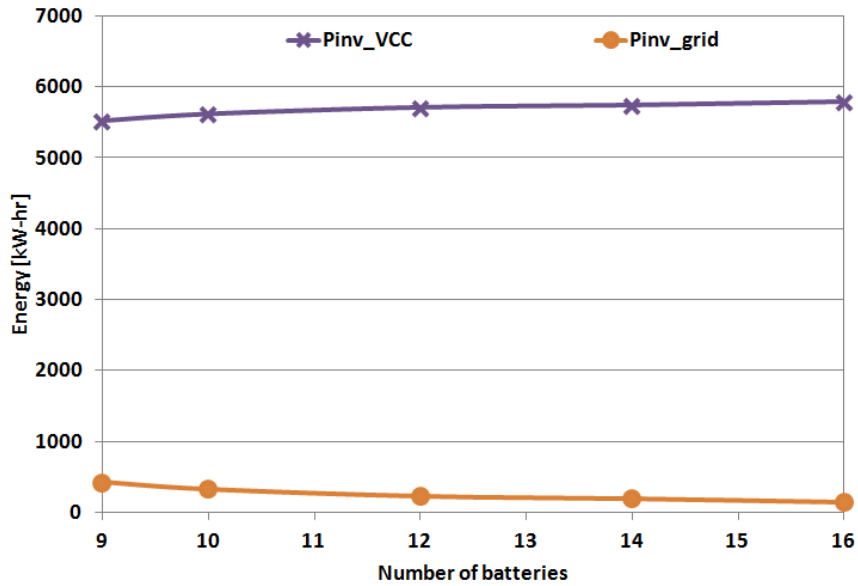
Figure 34: Effect of the electrical storage size on the electrical energy delivered.

One of the key parameters of any solar cooling system that highly affects its performance and initial cost is the collector area. The effect of the CPVT collector area on the amount of external electrical energy needed is shown in Figure 35. The results show that as the collector area is increased, the system becomes less dependent on the grid.
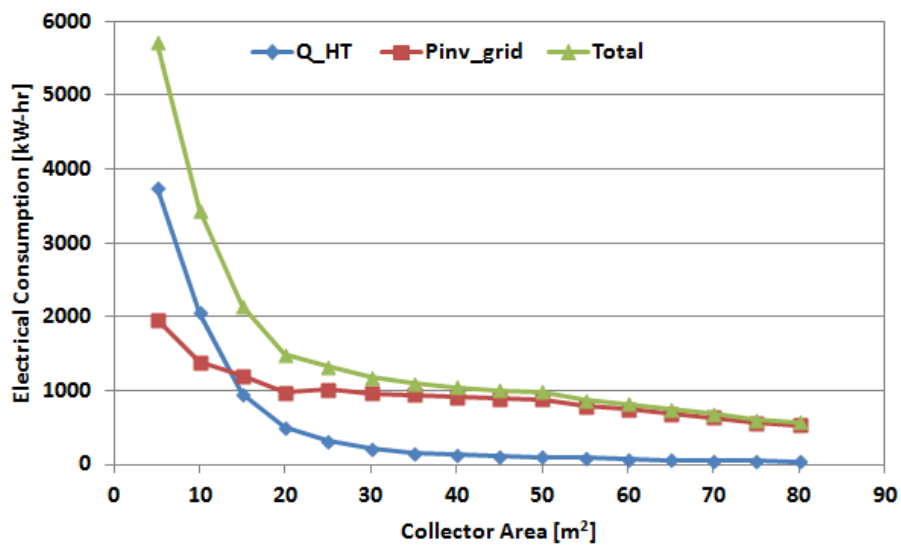
Figure 35: The effect of the collector area on the external energy needed

3.3   Overall System Performance

The main advantage of the hybrid air conditioning can be clearly seen in Figure 36. The heating season is considered to be from December to February, whereas the cooling season is from March to November. The figure shows the sensible and latent loads on the VCC. It indicates that when the DWC accommodates the latent load, the VCC has to accommodate the sensible load only. The latent load that is shown is due to the re-circulating of the space air which includes moisture from the internal latent load sources and infiltration. As previously described, by treating latent and sensible loads separately, the VCC can be operated at higher evaporating pressure hence reducing the cycle pressure ratio and increasing the compressor efficiency. If the DWC is to be eliminated, the standalone VCC has to accommodate the extra latent load introduced by ventilation in addition to the space internal latent load, Figure 37. This requires decreasing the evaporator's temperature below the dew point of the incoming air in order to condense the moisture. It can be seen that the latent load is higher during summer since the air temperature is higher; hence its capability of holding more moisture increases.
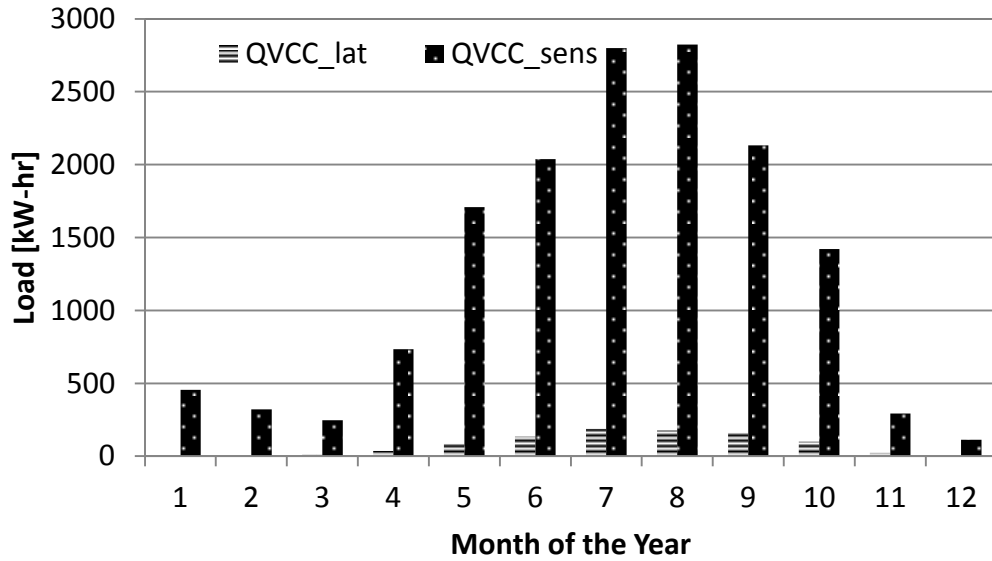
Figure 36: Monthly sensible and latent loads on the VCC (VCC + DWC).
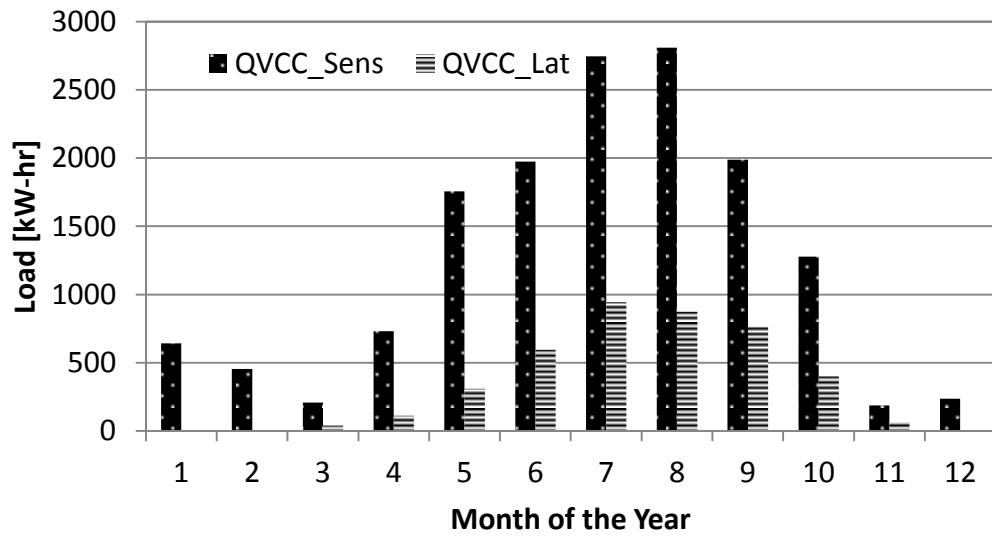
Figure 37: Monthly sensible and latent loads on the VCC (VCC only).

Figure 38 shows the results of comparing the proposed system to a VCC powered by PV panels and an absorption cycle driven by ETCs. The overall system COP of the solar hybrid air conditioner is above unity when cooling is needed the most. The current thermally driven solar air conditioners have low system COPs due to the limitation on the thermally driven cooling cycles. In addition, the electrically driven solar air conditioners

have low system COPs due the low electrical conversion efficiency of the PV cells. However, the proposed system eliminates these penalties by keeping the CPVT at high electrical yield by concentrating the solar irradiance and by the forced convective cooling of the PV cells. In addition, separating the latent and sensible loads contributes in increasing the COP of the VCC since it is performing at its most preferable conditions.
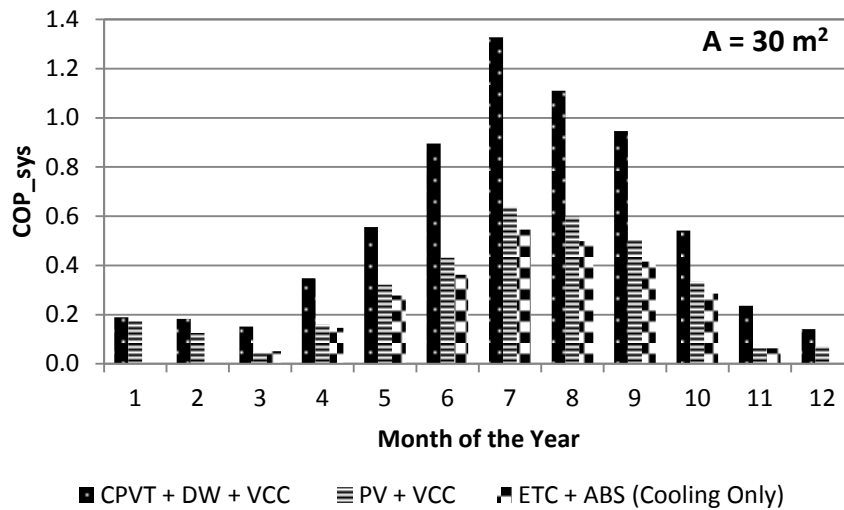
Figure 38: Comparison of the monthly performance of three solar air conditioners

Another advantage of the solar hybrid air conditioner can be seen when the hourly space temperature and humidity ratio are plotted in the psychrometric chart, as shown in Figure 39. The figure shows how effective the combination of the DWC and VCC is in obtaining the comfort level inside buildings located in hot and humid locations. It can be seen that the hourly conditions inside the building range from a temperature of 20°C to 25°C and a humidity ratio within 0.006-0.010 kg_w / kg_a. The performance of the system is compared to the performance of the solar electric air conditioners. The hourly space conditions for one year simulation for the standalone VCC powered by PV panels can be seen in Figure 40. The results indicate that the VCC alone is not as effective as the proposed system in

57

precisely controlling the temperature and humidity ratio of the conditioned space. The indoor conditions are found to be more scattered compared to hybrid solar air conditioner.
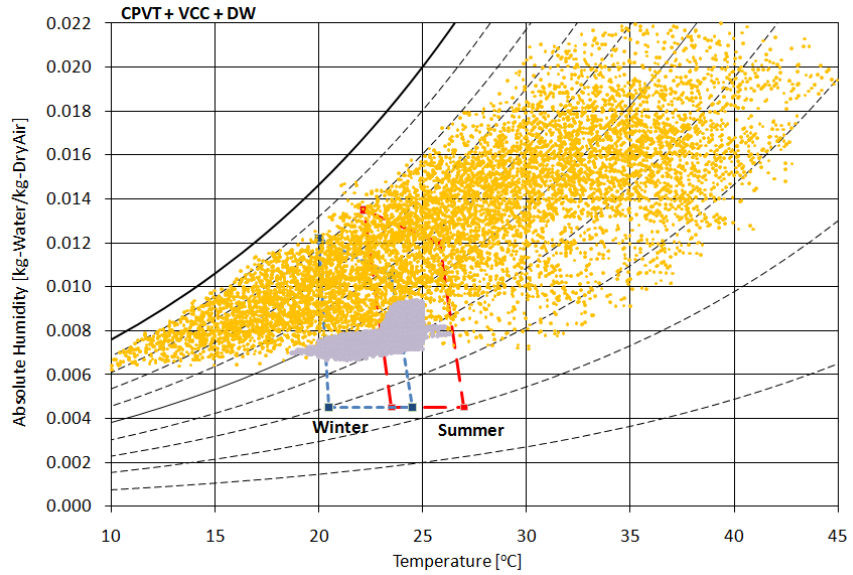
Figure 39: The hourly ambient conditions for Abu Dhabi and indoor space conditions for one year simulation (CPVT+VCC+DW).
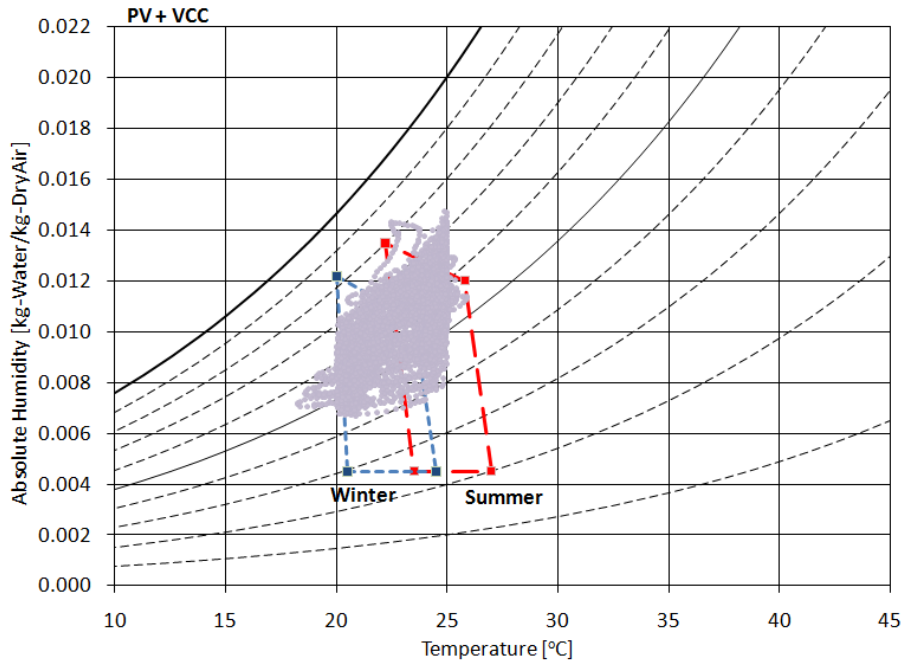
Figure 40: The hourly space conditions for one year simulation (PV + VCC)

3.4   Conclusions of the Hybrid Solar Air Conditioner Simulation

The simulation of the hybrid solar air conditioner involves processing meteorological information and modeling of various electrical and thermal components. The simulation of the novel solar powered air conditioner, which consists of a hybrid air conditioner and a hybrid solar collector, was carried out using TRNSYS simulation program. The results of the parametric study show that the CPVT collector area is the most important parameter that affects the system performance. The results also show that integrating a DWC with a conventional VCC is more effective than the standalone VCC in ensuring comfort of buildings in hot and humid climates. In addition, the simulation shows that the COP of the hybrid solar air conditioner is higher than that of a VCC powered by PV panels and a solar absorption system. The average cooling COP of the hybrid solar air conditioner, the solar VCC, and the solar absorption cycle are found to be 0.68, 0.34 and 0.29, respectively.

4. Desiccant Wheel Cycle Experimental Investigation

4.1 Experiment Apparatus

Prior to investigating the performance of the complete hybrid air conditioner, it is important to understand how the desiccant wheel cycle would perform under different operating conditions. It is also important to identify the most important variables that affect the cycle's performance. The desiccant wheel cycle is shown in Figure 41. The cycle consists of a desiccant wheel (DW), an enthalpy wheel (EW), and a water to air heat exchanger (WAHX).
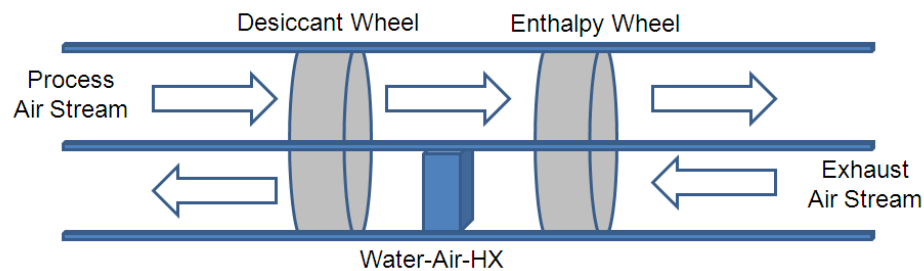
Figure 41: Desiccant wheel cycle schematic

Figure 42 shows the experimental setup used to investigate the performance of the desiccant wheel cycle (DWC). The fans had 3-phase motors which were controlled using variable frequency drivers. The volumetric flow rate was found using 76 mm nozzles, which were installed according to ASHRAE standards 41.2 (ASHRAE, 1992). The nozzle calibration results can be found in Appendix A. The air mixer was used to avoid air stream stratification. A hot water storage tank equipped with resistance heating elements was used to heat the exhaust air stream in the WAHX. The air duct, the DW, the EW were insulated in order to minimize the heat loss to the environment. The supply air stream temperature and humidity ratio were controlled using a vapor compression cycle,

an electric heater, a steam humidifier, and a desiccant wheel. The exhaust air stream inlet conditions, state 6, were fixed at a temperature of 25°C and a humidity ratio of 10 gw/kga. The purpose of the test is to investigate the effect of the process air inlet conditions, the DW rotational speed, and the regeneration air conditions on the cycle performance.
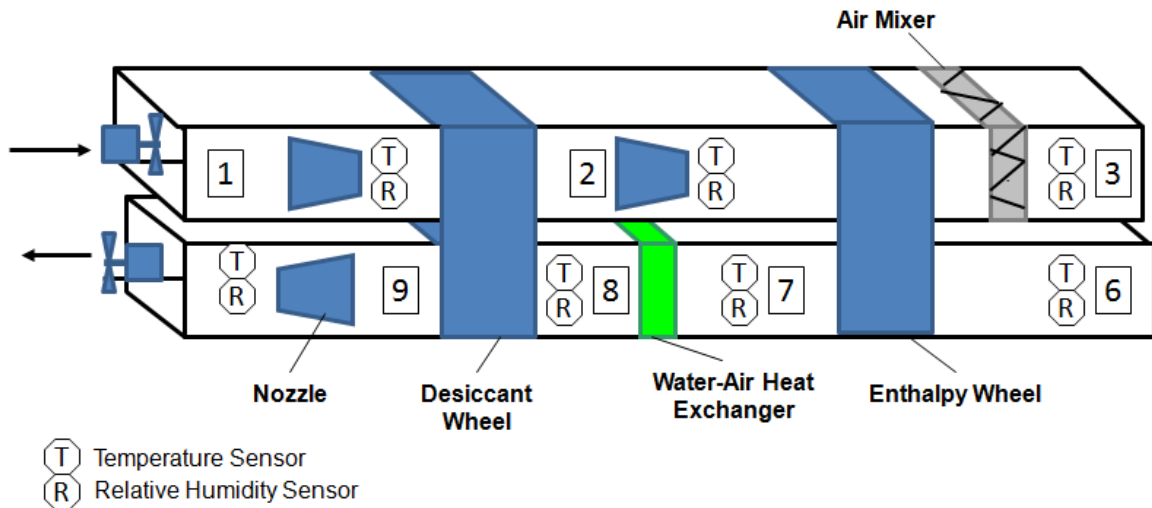
Figure 42: Experimental setup

4.2   Equipment

4.2.1   Desiccant Wheel

The desiccant wheel selected utilizes a new desiccant material based on zeolite, developed by Mitsubishi Plastics (Mitsubishi Plastics, 2010). The AQSOA, AQua SOrb zeolitic Adsorbent, utilizes Ferroaluminophosphate (FAM) Zeolite. This material has a unique isotherm shape. It has the property of changing the desiccant water content in a small change in relative humidity as shown in Figure 43. This adsorbent can also be regenerated using a low temperature heat source.
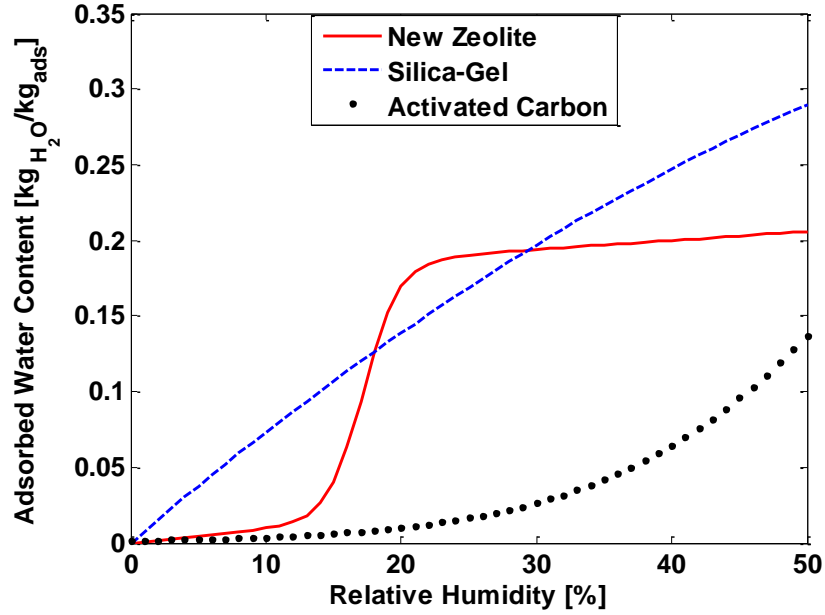
Figure 43: Isotherms of various desiccant materials

FAM-Z01 is selected in order to balance between the regeneration temperature and the amount of water vapor adsorbed. FAM-Z01 adsorbs less water vapor per one unit mass of adsorbent than FAM-Z02, Figure 44, but it can be regenerated using a lower temperature heat source. Even though, FAM-Z01 adsorbs similar amount of adsorbate as FAM-Z05, it starts the adsorption process at lower relative humidity. This is found to be more attractive for the hot and humid weather conditions. Figure 45 shows that FAM-Z01 can be regenerated with a low temperature heat source, as low as 45°C, which is lower than that needed for other commonly used desiccant material, i.e. Silica-Gel.
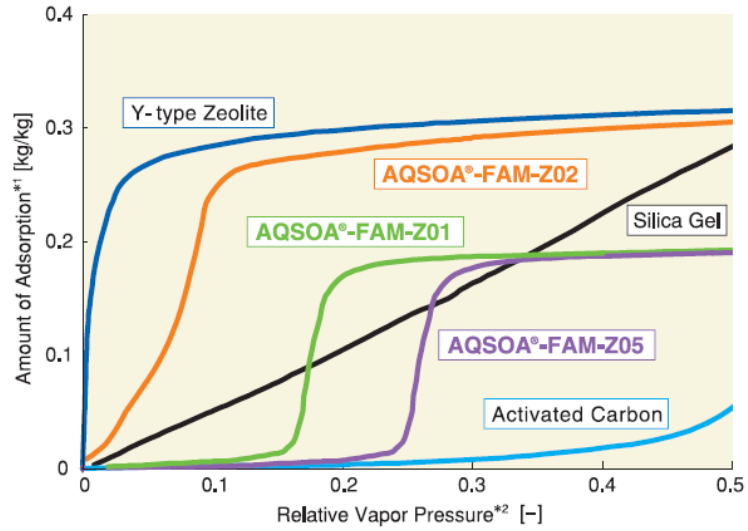
Figure 44: Isotherms of different adsorbents (Mitsubishi Plastics, 2010)
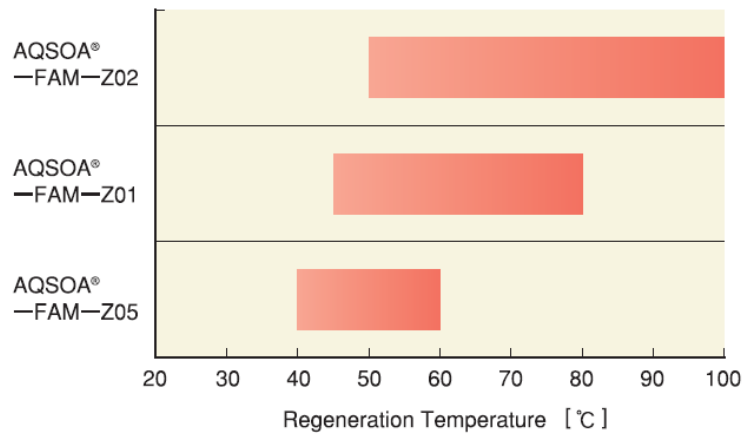
Figure 45: Recommended regeneration temperature (Mitsubishi Plastics, 2010)

The specifications of the DW used in the experiment are listed in Table 11 and the actual DW used is shown in Figure 46.

Table 11: Specifications of the desiccant wheel selected

Desiccant type	AQSO-FAM-Z01
Process/Reactivation Area Ratio	50:50 split
Thickness	200 mm
Wheel Diameter	350 mm

Figure 46: FAM-Z01 desiccant wheel

4.2.2 Enthalpy Wheel

The enthalpy wheel utilizes Molecular Sieve 3Å material, provided by Desiccant Rotors International. It has a sensible effectiveness of 83%. The specifications of the EW are listed in Table 12. The actual wheel is shown in Figure 47.

Table 12: Enthalpy wheel specifications

Material	Molecular Sieve 3Å
Process/Reactivation Area Ratio	50:50 split
Thickness	200 mm
Wheel Diameter	500 mm

Figure 47: The enthalpy wheel

4.2.3 The Water-Air-Heat Exchanger

The WAHX has to fit the air duct and deliver the required heat to maintain the regeneration temperature. The dimensions of the selected HX are 305 mm (Height) x 356 mm (Width) x 89 mm (Thickness). The capacity at the operating conditions is estimated to be 2.1 kW.

Figure 5: Water-Air-Heat Exchanger

4.3   Instrumentation

Details of the instrumentation used are provided in Table 13. The output signals of these instruments were recorded and analyzed using LabView. The purpose of the test is to investigate the effect of the process air inlet conditions, the DW rotational speed, and the regeneration air conditions on the cycle performance. Table 14 shows the test conditions used.

Table 13: List of the instruments

Instruments	Location	Quantity	Accuracy	Range
Temperature Measurements	Air side	7 (grids)	±0.5 °C	10-150 [°C]
	Water side	3 (points)	±0.5 °C	10-150 [°C]
Differential Pressure	Air side-supply (Nozzles)	2	±1 % [FS]*	0-500 [Pa]
	Air side-exhaust (Nozzle)	1	±1 % [FS]	0-500 [Pa]
RH Measurements	Air side	7	±1 %[RD]**	0-100 [%]
Mass Flow Meters (Coriolis Type)	Water side	1	±0.1 5%[RD]	0-0.5 [kg/s]

* FS = Full Scale   ** RD = Reading

Table 14: Test matrix

Test #	T_{amb} [°C]	w_{amb} [g_w/kg_a]	$\dot{m}_{air}$ [kg_a/s]	T_{reg} [°C]	R_{speed} [RPH]
1	25	16.2	0.085	55	5,10,15,20,25,30,35,40,45,50
2	30	16.2	0.085	55	5,10,15,20,25,30,35,40,45,50
3	35	16.2	0.085	55	5,10,15,20,25,30,35,40,45,50
4	30	14	0.085	55	5,10,15,20,25,30,35,40,45,50
5	30	20	0.085	55	5,10,15,20,25,30,35,40,45,50
6	30	16.2	0.1	55	5,10,15,20,25,30,35,40,45,50
7	30	16.2	0.085	45	5,10,15,20,25,30,35,40,45,50
8	30	16.2	0.085	65	5,10,15,20,25,30,35,40,45,50

4.4   Performance Indices

The rate of moisture removal from the process air stream is represented by the Moisture Removal Capacity (MRC), Equation (28).

$$MRC = \dot{m}_1(w_1 - w_2) \tag{28}$$

The performance of the DW is also investigated using the latent load removed from the process air stream compared to the heat provided to regenerate the wheel. The Latent Coefficient of Performance (COP_{Lat}) is calculated using Equation (29).

$$COP_{Lat} = \frac{MRC \cdot h_{fg}}{Q_{Reg}} = \frac{\dot{m}_1(w_1 - w_2)h_{fg}}{\dot{m}_9(h_8 - h_7)} \tag{29}$$

The performance of the EW is given by the effectiveness, Equation (30).

$$\varepsilon_{HW} = \frac{\dot{m}_9(T_7 - T_6) + \dot{m}_1(T_2 - T_3)}{2\,\dot{m}_{min}(T_2 - T_6)} \tag{30}$$
$$\text{where } \dot{m}_{min} = min(\dot{m}_1, \dot{m}_9)$$

In order to ensure the validity of the test results, the ratio of the moisture removal rate from the process air stream to the moisture rejection rate to the exhaust air stream should be maintained within 5%, (ASHRAE 139, 2007). The ratio is given by the Moisture Mass Balance (MMB) ratio calculated using Equation (31).

$$MMB = \frac{MRC}{MRR} = \frac{\dot{m}_1(w_1 - w_2)}{\dot{m}_9(w_9 - w_8)} \tag{31}$$

The ratio of the process air stream change in total energy to that of the exhaust air stream defines the total energy balance (TEB) of the DW, Equation (32). It has to be noted that in an ideal case the process through the DW is an isenthalpic process. In this experiment, the TEB is maintained within 10%.

$$TEB = \frac{\dot{m}_1(h_2 - h_1)}{\dot{m}_9(h_8 - h_9)} \tag{32}$$

4.5   Uncertainty Analysis

The purpose of the uncertainty analysis is to estimate the uncertainty in the calculated

results based on the uncertainties in the primary measurements. Therefore, each

performance index has uncertainty that depends on its independent variables. In order to

calculate the uncertainty of a function f, with independent variables $x_1, x_2, x_3, ..., x_n$,

Equation (33) is used.

$$U_f = \pm \sqrt{\sum_{i=1}^{n} \left(\frac{\partial f}{\partial x_i}\right)^2 U_{x_i}^2} \tag{33}$$

where U_{x_i} is the uncertainty of the independent variables. The independent variable

uncertainty is associated with precision and bias errors. The precision error (P) is a

measure of the random variation found during repeated measurements, whereas the bias

error (B) is the difference between the average value and the true value (Figliola and

Beasley, 2000). The error on a particular measurement is combined using the Root Sum

Square (RSS), Equation (34).

$$U_x = \sqrt{B^2 + (t_{95\%}P)^2} \tag{34}$$

where t is an estimator set to 1.96, corresponding to a probability of 95%. The bias error

is estimated by comparison and it is provided by the sensor manufacturer, otherwise

calibration is needed. However, the precision error is quantified through repeated

measurements and a statistical analysis of the recorded data. The sample standard

deviation, Equation (35), needs to be calculated using the mean value defined by Equation (36).

$$S_x = \sqrt{\frac{\sum_{i=1}^{n}(x_i - \bar{x})^2}{n-1}} \tag{35}$$

$$\bar{x} = \frac{\sum_{i=1}^{n} x_i}{n} \tag{36}$$

Then, the standard deviation of the means, Equation (37), can be used to estimate the precision interval of the mean.

$$S_{\bar{x}} = \frac{S_x}{n^{\frac{1}{2}}} \tag{37}$$

4.6   Results and Discussion

Prior to analyzing the results, the moisture mass balance ratio and the total energy balance are checked to make sure that they are within the acceptable range. Figure 48 show the MMB for all the tests. The MMB values are maintained within 5% except for a few outliers. Figure 49 show the TEB for all the tests. It has to be mentioned that there is no standard requirements for the range of acceptable TEB values. However, various precautions were taken in order to maintain the TEB values within 10%. The value of TEB deviates out of the range due to the decrease of the enthalpy difference at lower rotational speeds. The small enthalpy difference for both air steams, the process and the regeneration air streams, makes the ratio sensitive to small changes in either stream. This indicates that it is harder to maintain the ratio at lower rotational speed given that different energy losses to the environment are expected from the two air streams.
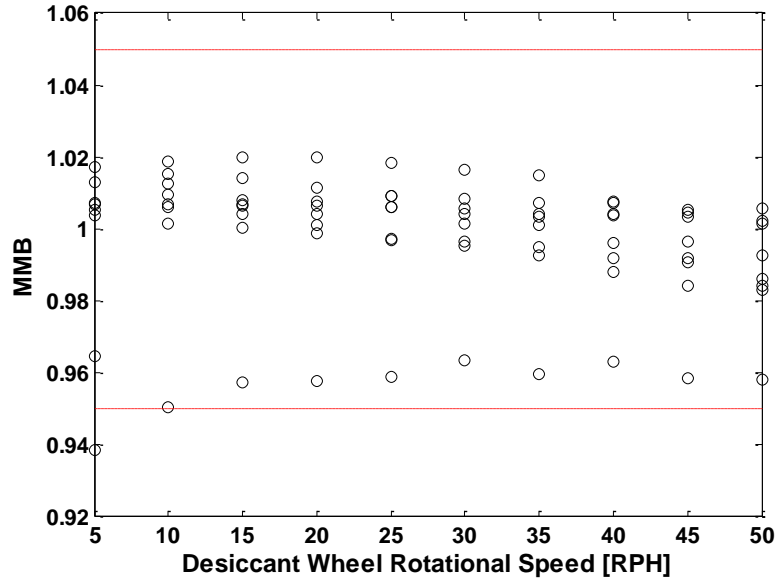
Figure 48: Moisture Mass Balances of all the tests
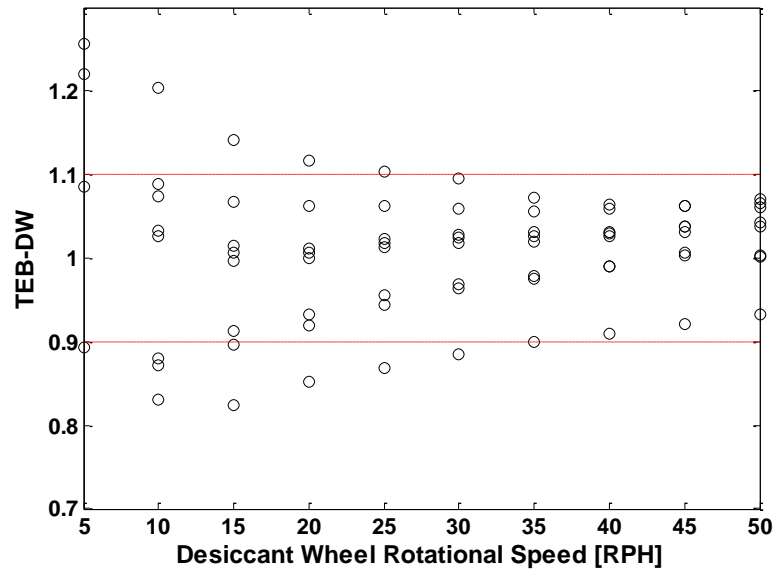
Figure 49: Total Energy Balances of all the tests

The effect of the ambient air temperature on the DWC MRC and COP_{Lat} were investigated. The MRC, Figure 50, and the COP_{Lat}, Figure 51, increase with decreasing ambient temperature. For the same humidity ratio, the lower the dry-bulb temperature is, the higher the relative humidity (RH). This indicates that the desiccant material water vapor content will be higher as shown by the isotherm line, which makes the MRC value

higher. For the same regeneration temperature, the COP_{Lat} would follow the same trend. Equation (29) indicates that the shape of the COP_{Lat} lines should be similar to that of the MRC. However, it has to be remembered that the regeneration temperature is kept constant and not the regeneration heat. In order to maintain a constant regeneration temperature, different regeneration heat is required based on the DW process air stream outlet conditions and the EW's effectiveness.
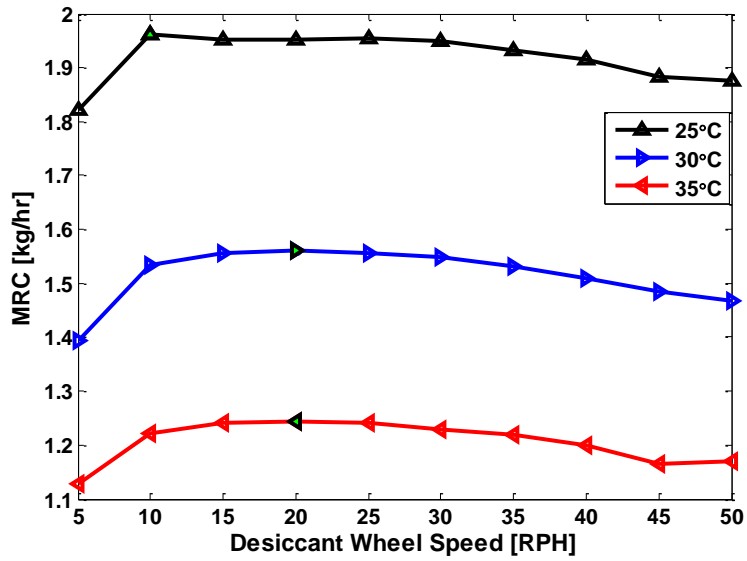
Figure 50: Effect of process air temperature on MRC
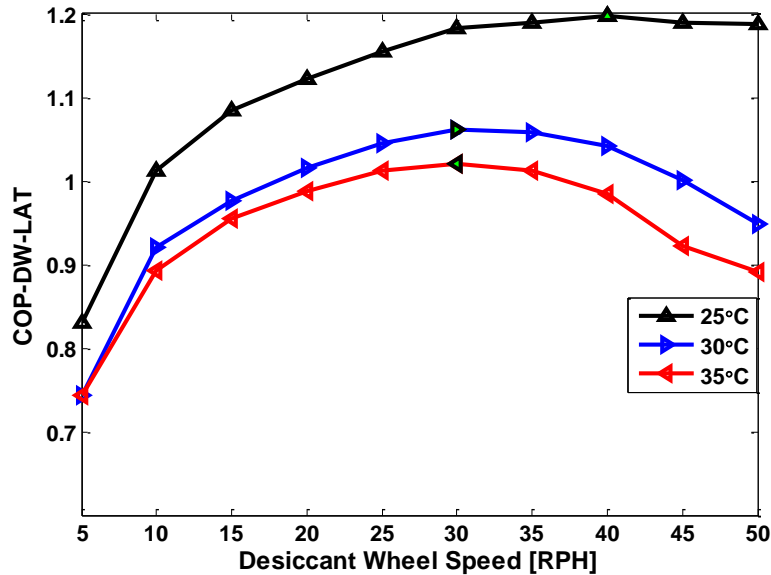
Figure 51: Effect of process air temperature on COP_{Lat}

71

Another important variable to investigate is the humidity ratio of the DW process inlet. It was found that the higher the humidity ratio is, the higher the MRC, Figure 52, and COP_{Lat}, Figure 53, values are. That is because at the same temperature, the higher the humidity ratio is, the higher the water vapor pressure. High water vapor pressure difference between the moist air and the desiccant surface increases the adsorption process. However, the condition of the moist air at the DW's process outlet is not necessarily drier. When the process air inlet is more humid, the humidity difference across the DW is higher as shown in Figure 54, which makes the MRC value higher. However, the process air outlet is more humid as shown in Figure 55.
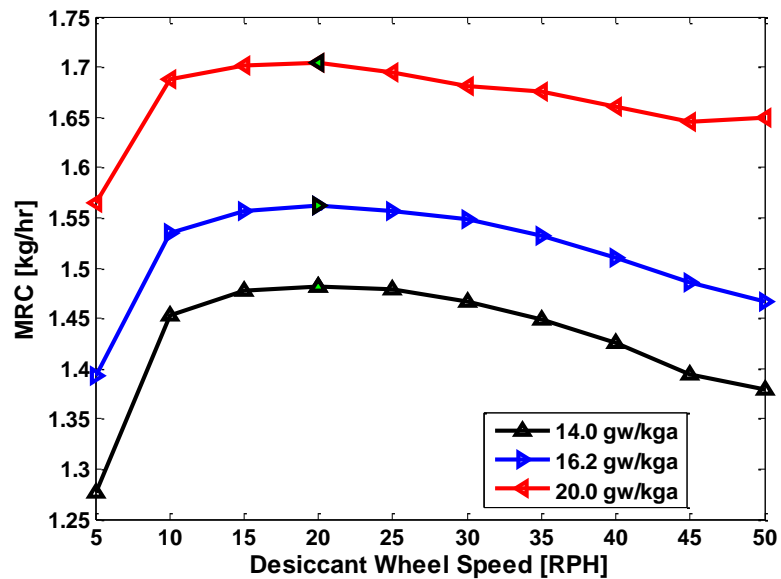
Figure 52: Effect of process air humidity ratio on MRC
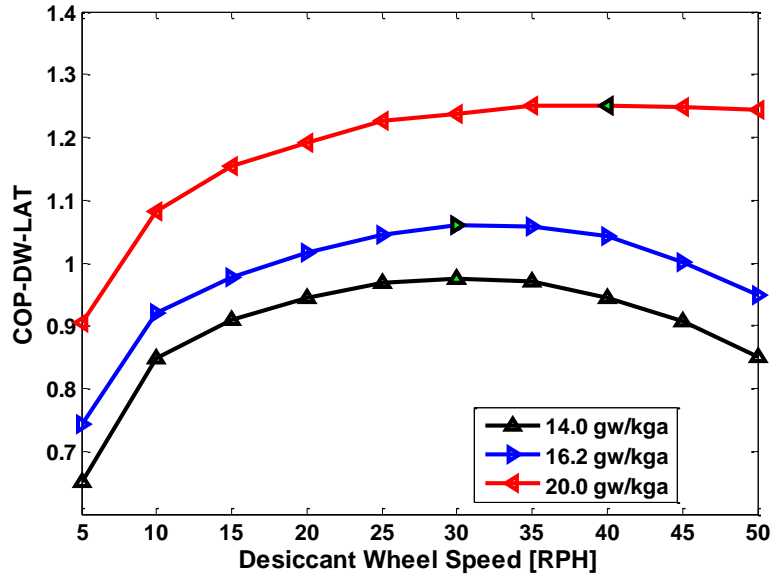
Figure 53: Effect of process air humidity ratio on COP_{Lat}
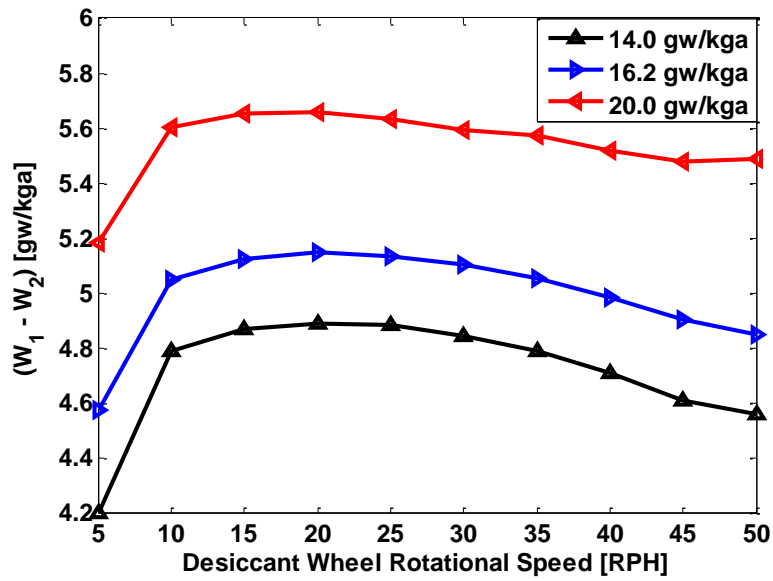
Figure 54: Effect of process air humidity ratio on process air humidity difference
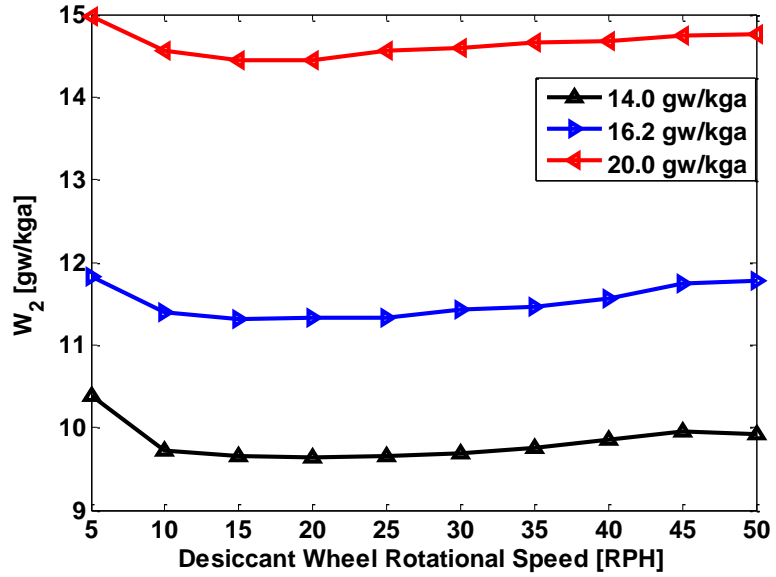
Figure 55: Effect of process air humidity ratio on DW's process outlet humidity ratio

Investigating the effect of increasing the ventilation mass flow rate was possible due to utilizing variable speed fans. Figure 56 shows that as the mass flow rate across the DW is increased, the MRC value increases. In order to maintain the same regeneration temperature, more heat is required for the higher mass flow rate. Therefore, the COP_{Lat} for the higher mass flow rate reduces as shown in Figure 57.
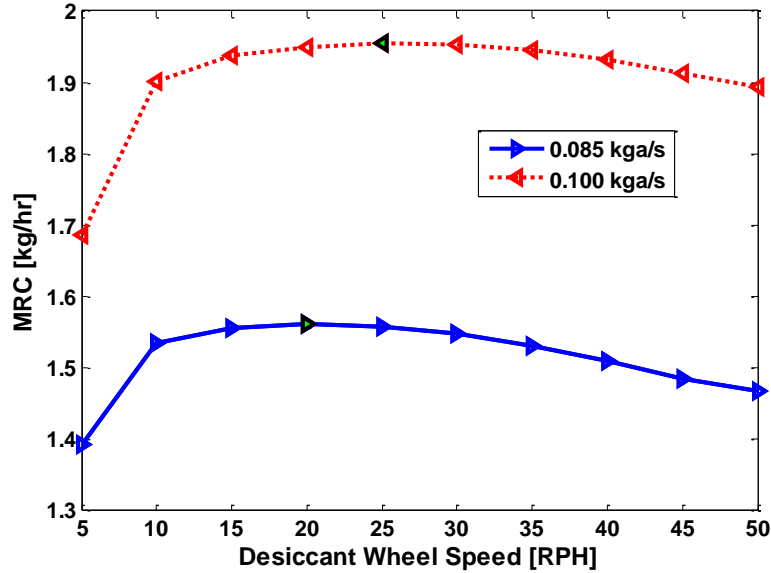
Figure 56: Effect of the ventilation flow rate on MRC
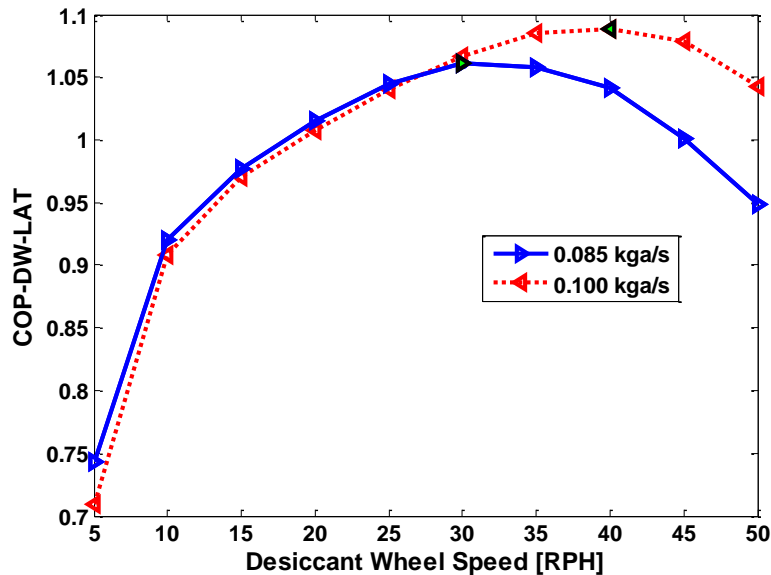
Figure 57: Effect of the ventilation flow rate on COP_{Lat}

Increasing the regeneration temperature allows the DW to be dried thoroughly and increases its capacity to adsorb water vapor, Figure 58. When the regeneration airstream's temperature is increased, the moist air relative humidity decreases. Lower RH value indicates lower water content in the desiccant material as shown by Figure 43. However, there is a decrease in the COP_{Lat}, Figure 59, because of the increase in the regeneration heat required to increase the regeneration temperature.
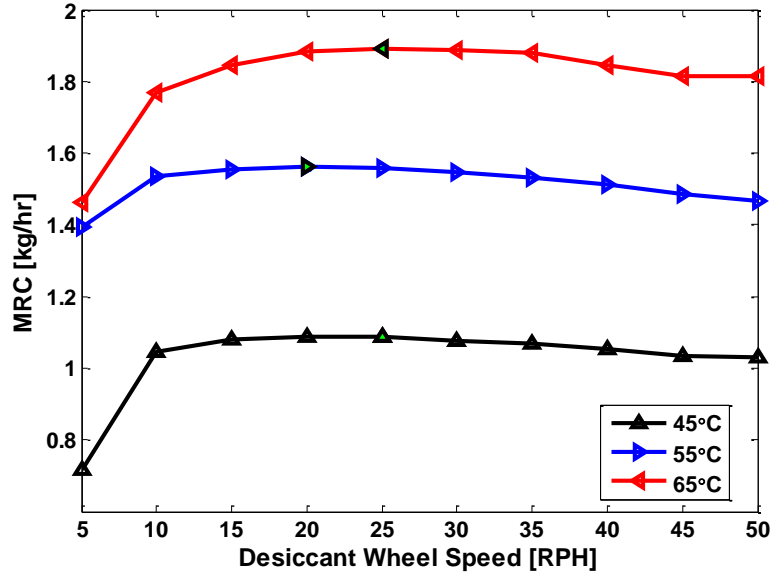
Figure 58: Effect of regeneration temperature on MRC
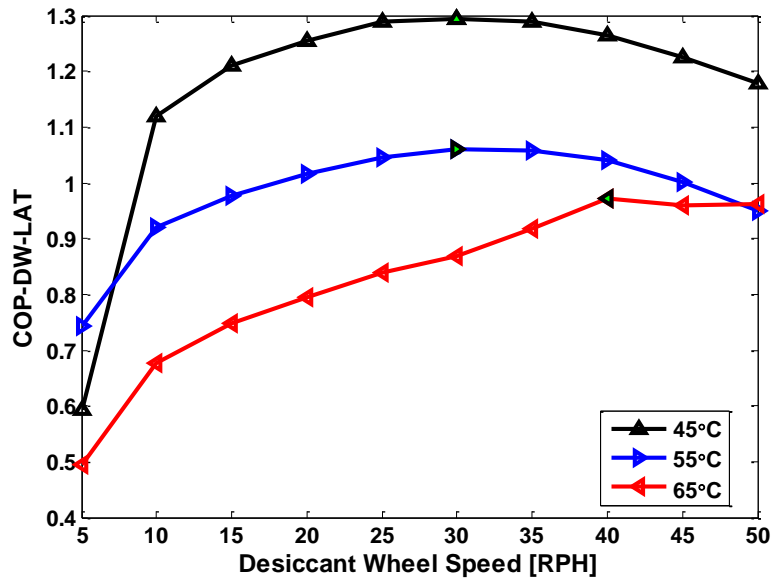
Figure 59: Effect of regeneration temperature on COP_{Lat}

The average effectiveness of all tests was found to be 0.71, Figure 60. The ratio of the process air temperature change to that of the exhaust air is found to be within 10% for most of the test runs, Figure 61. Test number 6, which corresponds to the case of higher mass flow rate, has the lowest ratio. This is expected to be due to the higher leakage between state 2 and 7 through the EW's rubber sealant.
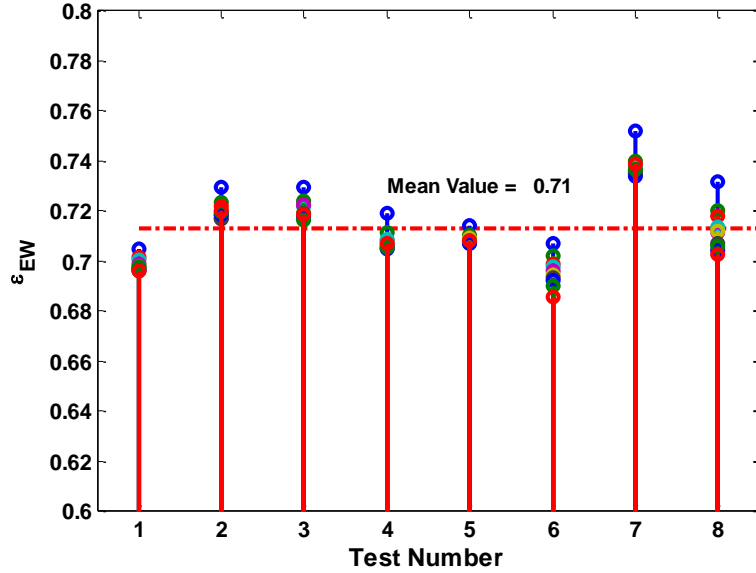
Figure 60: The enthalpy wheel's effectiveness
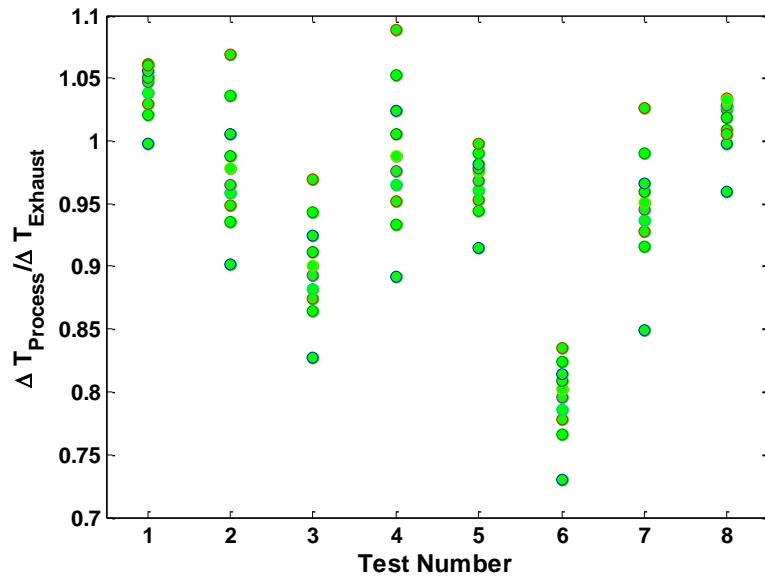
Figure 61: Temperature difference ratio at the EW

Part of the high COP_{Lat} value is due to the shape of the isotherm. This desiccant material has a rapid shift in water vapor uptake and can be regenerated using a low temperature heat source. The other part is due to the reduction in the regeneration heat by using the EW. Figure 62 shows the desiccant wheel COP_{Lat} with EW compared to that without the EW at DW rotational speed of 25 RPH. The value with the EW is found experimentally whereas the value without the EW is calculated using the experimental data.

77
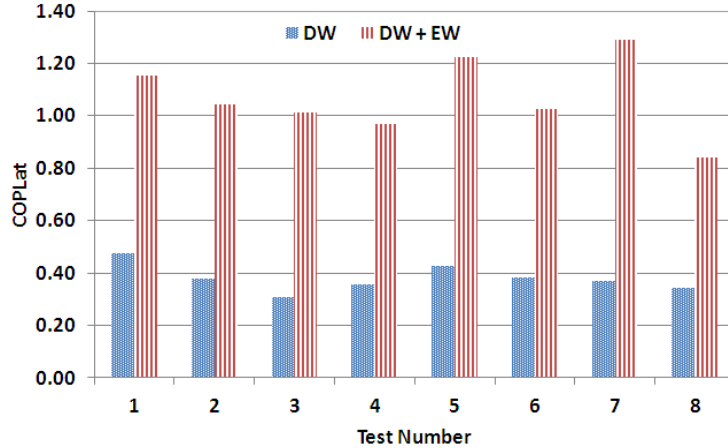
Figure 62: COP$_{Lat}$ with and without the enthalpy wheel

The performance indices' uncertainty analysis was performed at desiccant wheel rotational speed of 25 RPH. Table 15 shows the average value to each performance index and its percentage. As the table indicates, the highest uncertainty was the desiccant wheel total energy balance uncertainty. Its high uncertainty was caused mainly by the small change in the enthalpy across the desiccant wheel. The uncertainty in the enthalpy change for the two air streams was around 22% of the enthalpy change values.

Table 15: The desiccant wheel cycle testing uncertainties

Performance Index	Uncertainty	%
MRC	0.12	7.6
COP$_{lat}$	0.13	11.6
ε_{EW}	0.02	2.9
MMB	0.11	10.8
TEB	0.32	32.0

4.7 Conclusions of the Desiccant Wheel Cycle Testing

Understanding how the desiccant wheel cycle (DWC) performs as function of various variables is important for validation of a simulation tool. Testing the DWC allows the

identification of the most important variables to control. It also makes it easier to couple the DWC with other air conditioning cycles in order to obtain the desired outputs.

The performance of the desiccant wheel cycle was experimentally investigated. The effect of the process air stream conditions, the regeneration temperature, the mass flow rate, and the desiccant wheel rotational speed on the cycle performance was studied. The results show that for the tested conditions, the highest desiccant wheel capacity was obtained for the lowest process air stream temperature, and for the highest air mass flow rate. This does not necessary ensure sufficient dry conditions at the desiccant wheel process air stream outlet. In addition, the highest latent coefficient of performance for the desiccant wheel was obtained for the lowest regeneration temperature case. Both performance indices did not vary much with rotational speed between 20-30 RPH. Moreover, the average enthalpy wheel effectiveness for all the tests was found to be 0.71.

5. The Hybrid Air Conditioner Experimental Investigation

5.1 <u>Experimental Facility</u>

The experimental facility for testing the complete hybrid air conditioner was constructed by expanding the experimental facility of the desiccant wheel cycle to include the conditioned space and the vapor compression cycle. Figure 63 shows a schematic of the experiment setup. It mainly shows the air loop. There were also a hot water loop, which was connected to the WAHX, and a refrigerant loop, which was connected to the evaporator. Three fans were utilized for the fresh ambient air, the conditioned space circulation, and the conditioned space exhaust. All the fans were sized to maintain the design mass flow rate given the estimated system pressure drop. All the fans were variable speed fans controlled by frequency controllers. The conditioned space volumetric flow rate was found using a 178 mm nozzle, which was installed according to ASHRAE standards 41.2 (ASHRAE, 1992). Air mixtures were used at different locations to avoid stratification.
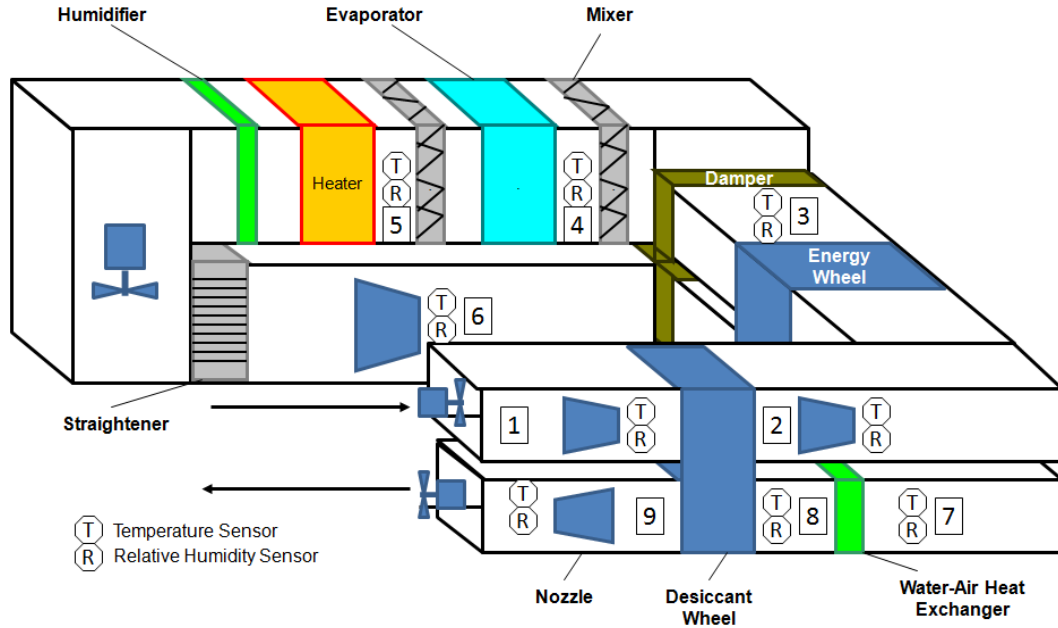
Figure 63: Schematic of the experiment setup

5.2   Equipment

5.2.1   Vapor Compression Cycle

The VCC system capacity is 4.5 kW, based on ASHRAE Standard's test A conditions
(ASHEAE, 2010). The charge optimization study can be found in Appendix C. The cycle
utilized R-410A as its working fluid. The compressor was a variable speed compressor
with a displacement volume capacity of 13.2 cc. Figure 64 shows the compressor and its
inverter. An electronic expansion valve was also used as a metering device.
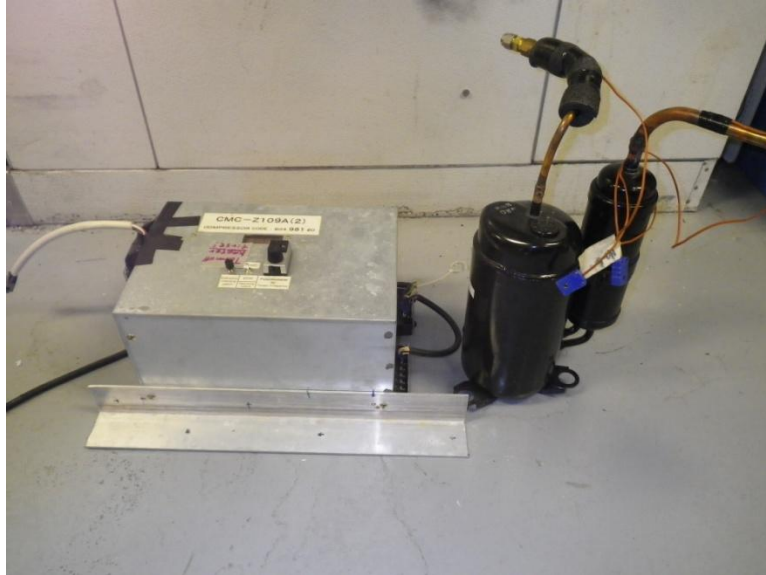
Figure 64: The variable speed compressor and its inverter

5.2.2 Conditioned Space

The conditioned space is represented by an electric heater and a humidifier. The electric air heater is used to represent the space sensible load. The selected heater has a 5 kW of heating capacity, model DH-5000-240-1 supplied by Tutco Heating Solutions, Figure 65. The heater is rated at 240 V single phase power.
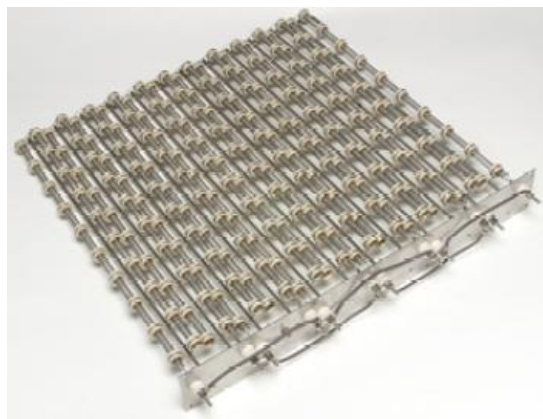
Figure 65: Electric air heater to represent the space sensible load.

The humidifier is used to represent the latent load of the conditioned space. The selected humidifier is capable of delivering 23 liter/day.

5.3   Instrumentations

A summary of the instruments used in this experiment with their respective range and accuracy is shown in Table 16.

Table 16: Instruments' range and accuracy

Instruments	Location	Quantity	Accuracy	Range
Temperature Measurements (T-Type Thermocouples)	Air side	9 (grids)/9 TCs each	± 0.5 °C	10-150 [°C]
	Refrigerant side	4 (points)	± 0.5 °C	5-150 [°C]
	Water side	3 (points)	± 0.5 °C	10-150 [°C]
Pressure Measurements	Refrigerant side	4 (points)	$\pm 0.125\%$ [FS]*	0-3447 [kPa]
Differential Pressure	Air side (nozzles)-supply	2	$\pm 1\%$ [FS]	0-498 [Pa]
	Air side (nozzles)-exhaust	1	$\pm 1\%$ [FS]	0-498 [Pa]
	Air side -conditioned space	1	$\pm 1\%$ [FS]	0-1245 [Pa]
RH Measurements	Air side	9	$\pm 1\%$ [RD]**	0-100 [%]
Mass Flow Meters (Coriolis Type)	Refrigerant side	1	$\pm 0.15\%$ [RD]	0-130 [g/s]
	Water side	1	$\pm 0.15\%$ [RD]	0-500 [g/s]
Power Meters	Compressor	1	$\pm 0.5\%$ [FS]	0-6 [kW]
	Electric air heater	1	$\pm 0.2\%$ [RD]	0-4 [kW]

* FS: Full Scale, ** RD: Reading

In this test, the effect of the ambient temperature, the ambient humidity ratio, and the ventilation rate on the indoor conditions was investigated. The test matrix for this experiment is shown in Table 17. The DW rotational speed is fixed at 25 RPH and the regeneration temperature is maintained at 55°C.

Table 17: Test matrix

Test #	T_{amb} [°C]	w_{amb} [g_w/kg_a]	$\dot{m}_{air}$ [kg_a/s]	R_{speed} [RPH]	T_{regen} [°C]
1	25	16.2	0.085	25	55
2	30	16.2	0.085	25	55
3	35	16.2	0.085	25	55
4	30	14	0.085	25	55
5	30	20	0.085	25	55
6	30	16.2	0.1	25	55

5.4   Results and Discussion

The hybrid A/C was compared to a standalone VCC, both operating at ARI's humid conditions (Ge et al., 2008). In the standalone VCC case, two operation conditions of the VCC were used: one was with no ventilation load and the other was with ventilation rate of 10% of the mass flow rate supplied to the conditioned space. The indoor conditions at steady state operation are shown in Figure 66. The figure shows that the standalone VCC was not able to maintain space comfort conditions at 0% and 10% ventilation rates. The space comfort conditions shown are based on ASHRAE thermal comfort zone (ASHRAE, 2009). This indicates that the standalone VCC has to be oversized in order to control the temperature and the humidity simultaneously. This result clearly show the problem of A/C over sizing that HVAC engineers face in hot and humid climates. The figure also shows that comfort conditions can be achieved by activating the DWC while using the same VCC capacity.
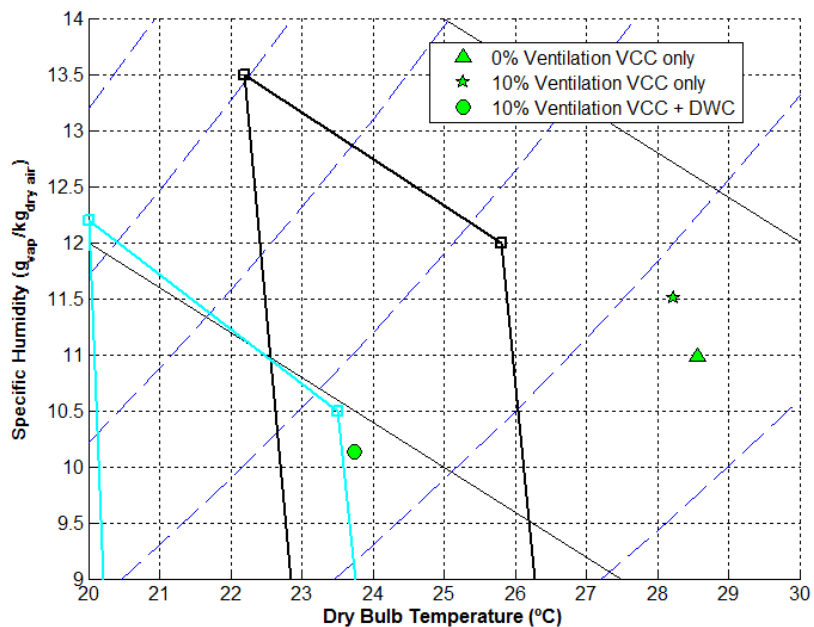
Figure 66: Indoor conditions for the hybrid A/C and the standalone VCC

The performance of the hybrid A/C was investigated at various ambient conditions. The temperature and the humidity ratio of these conditions are listed in Table 17. In addition, the ventilation rate was increased to see if the system was capable of maintaining the comfort conditions inside the space. Figure 67 shows the moisture mass balance of the hybrid A/C tests. The MMB is maintained within the acceptable range for all the tests.
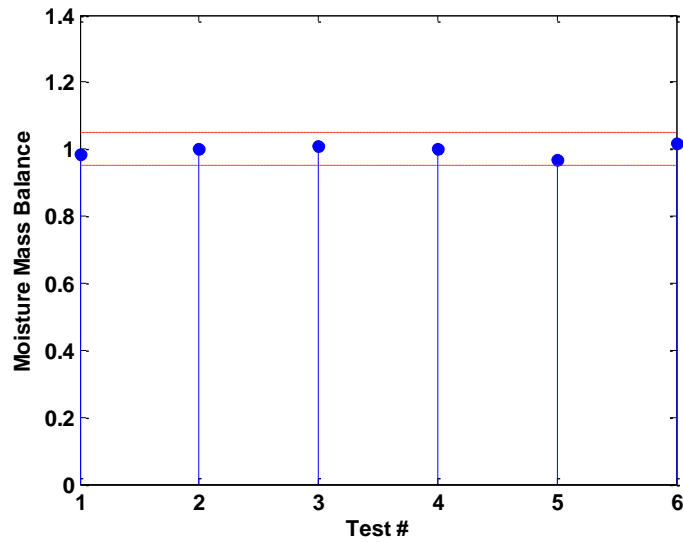
Figure 67: Moisture mass balance of all the tests

Figure 68 shows the moist air conditions at the inlet and the outlet of the desiccant wheel cycle (DWC). The DWC reduces the humidity content of the fresh air stream while maintaining acceptable temperatures. The DWC's outlet conditions have less scattering compared to the inlet conditions.
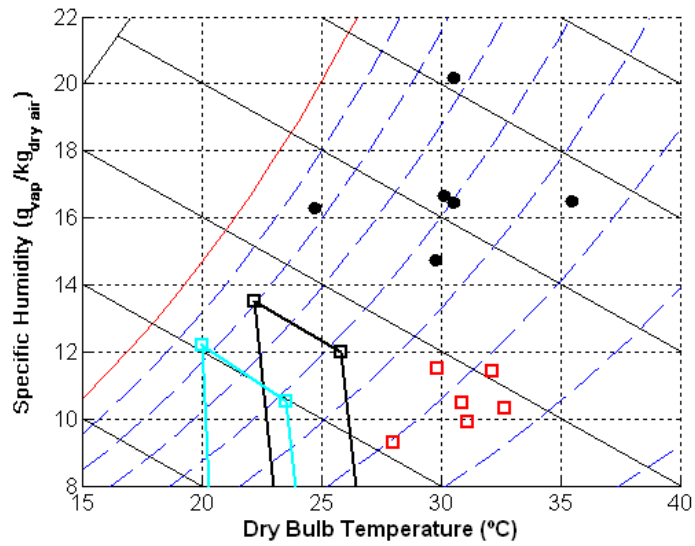
Figure 68: Inlet (Black Circles) and outlet conditions (Red Squares) of the desiccant wheel cycle

Figure 69 shows the indoor conditions of all the tests conducted. It can be seen that the hybrid A/C is able to maintain comfort in the conditioned space for various ambient and operating conditions.
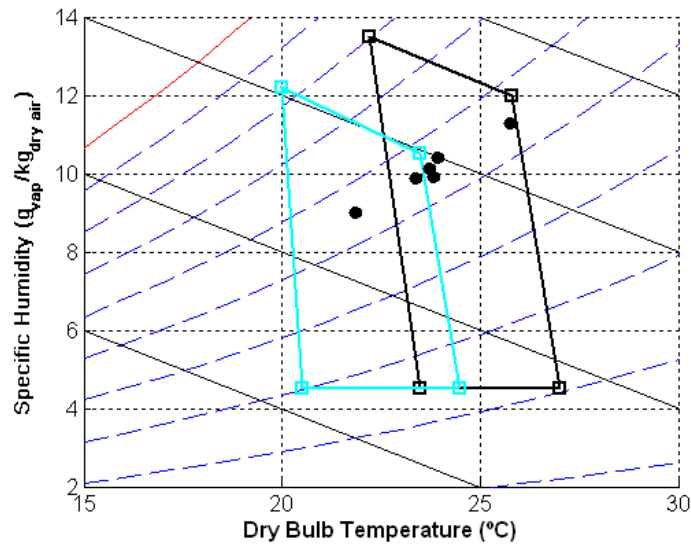
Figure 69: Indoor conditions for the hybrid A/C at various operating conditions

Moreover, the VCC can be operated differently when coupled with a DWC. Since the DWC accommodates the latent load, the VCC has to accommodate the sensible load

only. This allows the VCC to operate at higher evaporating pressure and temperature. Figure 70 shows the refrigerant state points on T-s and P-h diagrams.
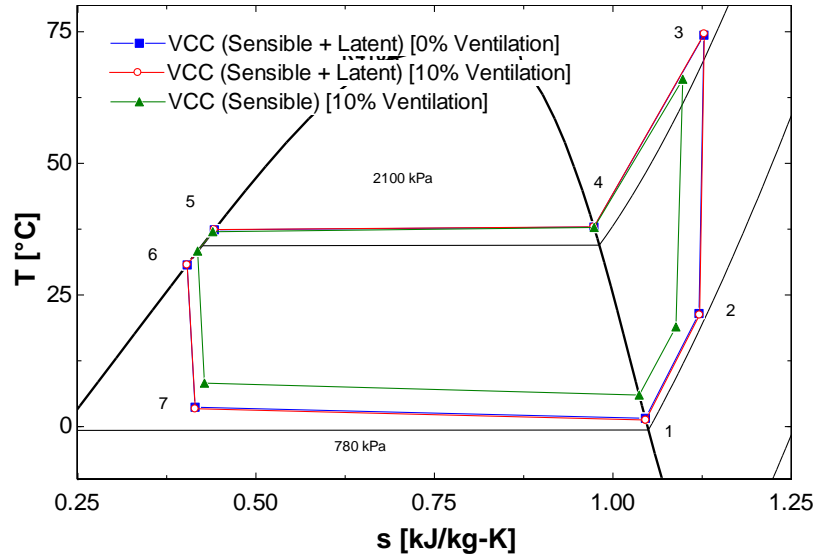
(a) T-s diagram
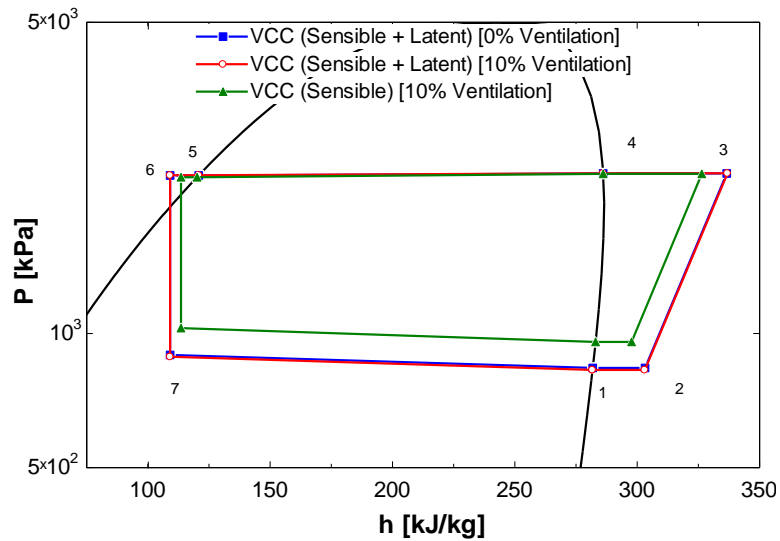
(b) P-h diagram

Figure 70: VCC refrigerant state points

The experimental data is used to estimate the performance of the hybrid solar A/C as shown in Table 18. The performance of the hybrid A/C under ARI's humid conditions is used. It has to be mentioned that the hybrid solar A/C coefficient of performance

(COP_{sys}) in Equation (38), is based on the electric energy since the collector's thermal output is considered as a byproduct and it is quantitatively higher than the electric output. The COP_{sys} is defined as the total cooling effect provided by the DW and the VCC divided by required solar energy captured by the hybrid solar collector. The DW latent capacity and the VCC capacity are given by Equations (39) and (40), respectively.

$$COP_{sys} = \frac{(Q_{DW} + Q_{VCC})}{P_{VCC}/\eta_{elec_{Coll}}} \tag{38}$$

$$Q_{DW} = \dot{m}_1(w_1 - w_2)h_{fg} \tag{39}$$

$$Q_{VCC} = \dot{m}_4(h_4 - h_5) \tag{40}$$

where $\eta_{eleccoll}$ is the collector electric efficiency, P_{VCC} is the electrical power consumed by the vapor compression cycle, h_{fg} is the latent heat of water, and h is the moist air enthalpy.

Three different collector efficiencies are used. The first one is assumed based on typical values, the second one is based on the available subroutine, TYPE 50, in transient system simulation program (TRNSYS), and the third is based on an experimentally verified parabolic trough collector (Coventry, 2005). The table shows that, in order to provide the energy required to run the cooling sub-system, 0.8 and 1.3 kW, a collector with an electrical efficiency of 0.2 would need 3.98 kW of solar energy input. It also shows that a COP_{sys} higher than unity could be achieved. Even for COP_{sys} values lower than unity, the value is about double what the current technology is.

Table 18: The hybrid solar air conditioner performance predictions

System	$E_{provided,Exp^*}$ [kW]	COP_{Exp}	$E_{required}$ [kW]	Collector Efficiency		E_{collin} [kW]	COP_{Sys}
VCC	4.22	5.3	0.8	Assumed	$\eta_{elec} = 0.2$	3.98	1.4
DW	1.4	1.05	1.3		$\eta_{ther}^{**} = 0.65$	-	
VCC	4.22	5.3	0.8	TRNSYS	$\eta_{elec} = 0.17$	4.68	1.2
DW	1.4	1.05	1.3		$\eta_{ther} = 0.64$	-	
VCC	4.22	5.3	0.8	Exp	$\eta_{elec} = 0.11$	7.24	0.8
DW	1.4	1.05	1.3		$\eta_{ther} = 0.58$	-	

* Exp: Experimental value, ** η_{ther}: Collector's thermal efficiency

Table 19 shows the uncertainties associated with testing the hybrid air conditioner. As one would expect, the uncertainties of the refrigerant side were smaller than their air counterparts, for the same performance index.

Table 19: The hybrid air conditioner testing uncertainties

Performance Index	Uncertainty	%
MMB	0.11	11.1
$Qvcc_{air}$	0.30	6.6
$Qvcc_{ref}$	0.05	0.9
$COPvcc_{air}$	0.46	8.4
$COPvcc_{ref}$	0.12	2.0

5.5   Conclusions of the Hybrid Air Conditioner Testing

The performance of the hybrid A/C system was experimentally investigated. Its performance was compared to that of a standalone VCC. The standalone VCC was not able to maintain the comfort conditions under ARI's humid conditions. However, the comfort zone is reached when the desiccant wheel cycle is activated. This indicates that the standalone VCC has to be oversized in order to control the humidity and temperature

simultaneously. At different ambient conditions, the hybrid A/C system is found to be very effective in keeping the indoor conditions within the comfort zone. Using the experimentally data, the overall coefficient of performance COP_{sys} of the hybrid A/C powered by a hybrid solar collector is calculated. A COP_{sys} value more than unity is found to be achievable.

6. Optimization Study

6.1 <u>Introduction</u>

In order for the solar air conditioners to become a real alternative to the conventional systems, their performance and total cost have to be optimized. Optimization cannot be simply replaced by a parametric study unless it is a single variable optimization problem. In reality, most of the optimization problems encountered are nonlinear, and finding the optimum design of a system involves dealing with multi-variables, multi-objectives and constrained problems. In order to determine the optimum design, the designer undergoes a trial and error process to guess how to change variables for the next step but this process is very time-consuming and expensive. Therefore, it is important to use existing or user defined optimization algorithms where less designer input is required. The purpose of this part of the thesis is to minimize the solar hybrid A/C's cost and energy consumption using systematic optimization techniques. This requires investigating the various optimization options and finding the most suitable approach to be used with TRNSYS simulations.

6.2 <u>Optimization Algorithms</u>

There are various ways in which optimization can be carried out for the solar hybrid air conditioner. One approach is using an existing component in TRNSYS, TYPE 583, which launches TRNSYS Optimizer (TRNOPT) (Klein et al., 2007). TRNOPT acts as an interface between TRNSYS and the GENOPT Optimizer (Wetter, 2001). GENOPT is a generic optimization algorithm developed by the Lawrence Berkeley

National Laboratory. It is designed to interface with black-box simulation programs. Therefore, the objective function is evaluated by TRNSYS which is iteratively called by GENOPT. Another method is coupling TRNSYS with MATLAB (The MathWorks, 2009). Based on a user developed interface, MATLAB can open TNRSYS's input file and alter the design variables. Then, MATLAB calls TRNSYS engine to run the modified input file and reads the output file to find the value of the objective function as illustrated in Figure 71. In this study, MATLAB is selected as an optimizer because it has an optimization tool box which handles single and multi-objective, single and multi-variable, unconstrained and constrained optimization problems. It also has a Genetic Algorithm (GA) optimization tool box for global optimization (The MathWorks, 2009). Therefore, the second approach allows more robustness and flexibility in formulating the optimization problem.
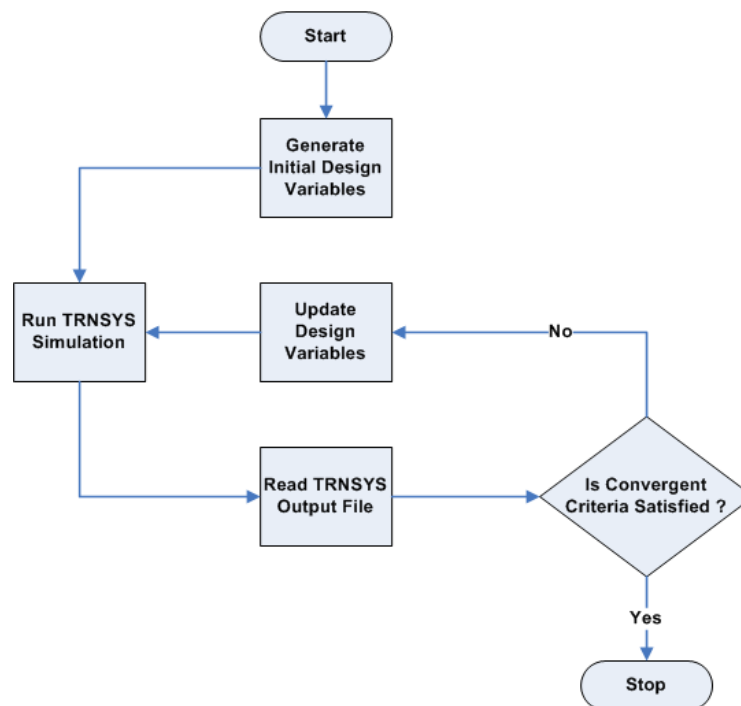
Figure 71: MATLAB optimization flow diagram

Different optimization algorithms are compared in order to find the most appropriate one for TRNSYS application. The algorithms are compared based on two measures: Robustness, which is related to the ability to find a global optimum and the dependence of performance on initial guess, and Efficiency, which deals with how many function evaluations are required.

Initially, some gradient based algorithms, *fminunc* and *fmincon*, were tried. However, it was found that the non-gradient methods were better. In this investigation, *fminsearch*, Pattern Search (PS) and GA are selected from MATLAB. *fminsearch* is usually used to find a local minimum for unconstrained nonlinear optimization. It uses the Nelder-Mead simplex algorithm, which does not require numerical or analytical gradient of the objective function (Arora, 2004).

The Pattern Search method is also used to solve the single objective optimization problems. It does not require any information about the gradient of the objective function (The MathWorks, 2009). At each step, the algorithm searches a set of points, called a mesh, around the current point and looks for a point where the value of the objective function is lower than that of the current point. Once the algorithm finds a point that improves the objective function, the new point becomes the current point at the next iteration. The mesh is formed by adding the current point to a scalar multiple of a set of vectors called a pattern.

GA is a population based method used to find global optimal solutions. It selects individuals at random from the current population to be parents and uses them to produce the children for the next generation. Over successive generations, the

population progress toward an optimal solution (The MathWorks, 2009). Figure 72 shows the working principle of GA.
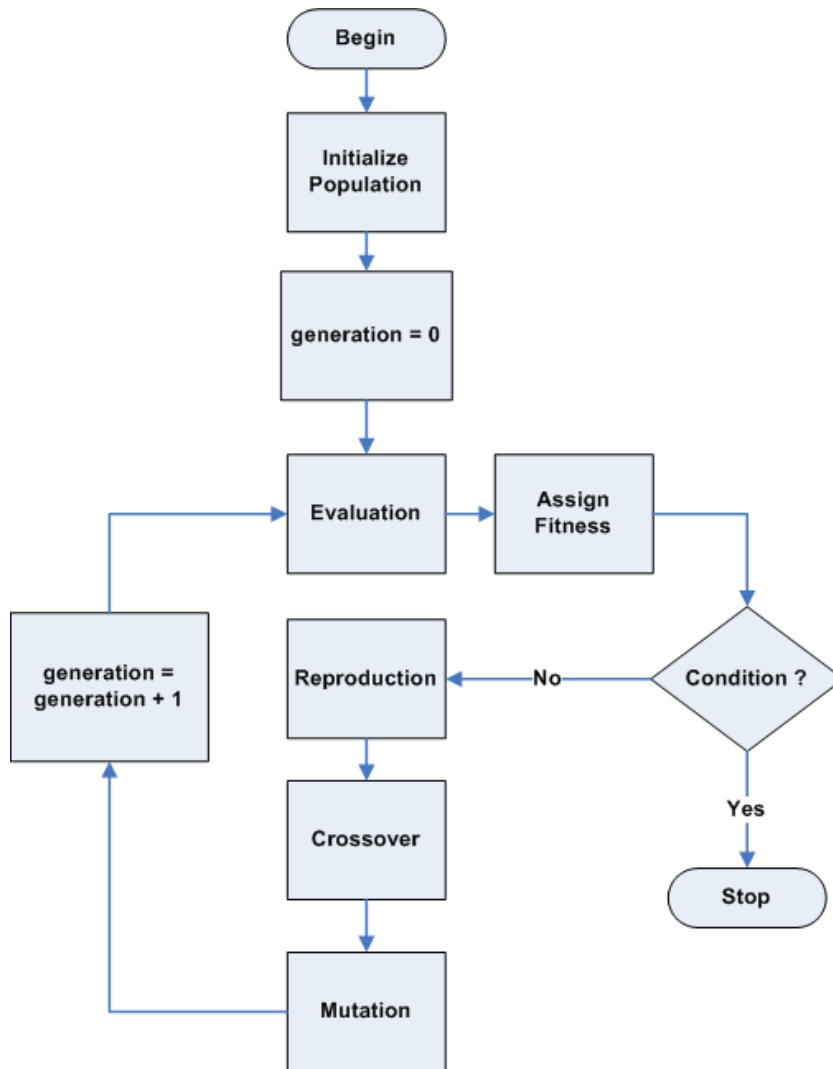
Figure 72: A flowchart of GA's working principle (Deb, 2001)

6.3 Optimization Problem Formulation

Two optimization problems are formulated for the optimization of the hybrid solar air conditioner. The first optimization problem is to minimize the electrical consumption of the complete system. The second is to minimize the total cost of the system. Both problems are formulated as follows:

$$\underset{x_1,x_2,\dots,x_n}{\text{Minimize }} f(\vec{x}) = f(x_1, x_2, \dots, x_n) \tag{41}$$

Subject to
$$g_j(\vec{x}) \le 0, \quad j = 1, \dots, J \tag{42}$$

$$h_k(\vec{x}) = 0, \quad k = 1, \dots, K \tag{43}$$

$$\vec{x}_L \le \vec{x} \le \vec{x}_U \tag{44}$$

where $\vec{x}$ represents the design variables: collector area, collector mass flow rate, storage tank volume, and number of batteries. Table 20 shows the details of the design variables.

Table 20: Optimization design variables

Variables	Units	Range
A_{coll}	m^2	[5-80]
$\dot{m}_{coll}$	kg/hr	[500-2000]
V_{tank}	m^3	[0.5-5]
N_{batt}	-	[2-20]

The electrical consumption of the complete hybrid solar A/C was calculated using Equation (45). The electricity requirement of the different components was not simultaneous. Therefore, the control signal (*CS*) was used to include the component's power consumption only when it was activated, as shown in Equations (46) to (48). The pump power consumption was based on pump laws. The DW, EW, and VCC power consumption was based on the components used in the experiment. The fan's power was calculated based on the anticipated pressure drop of the actual installation. The experimental fans power consumptions were not used since the fans were sized to overcome the pressure drop of the nozzles, thermocouples' meshes, and other experimental components.

$$P_{grid} = \int_{t_{start}}^{t_{stop}} (P_{pumps} + P_{fans} + P_{wheels} + P_{inverter}).\,dt \tag{45}$$

95

$$P_{pumps} = CS_{PumpColl}P_{PumpColl} + CS_{PumpLoad}P_{PumpLoad} \tag{46}$$

$$P_{fans} = CS_{fanSupp}P_{fanSupp} + CS_{fanExh}P_{fanExh} \tag{47}$$

$$P_{wheels} = CS_{DW}P_{DW} + CS_{EW}P_{EW} \tag{48}$$

The Total Cost (*TC*) of the system was divided into the initial capital cost and operating cost. Table 21 shows the initial cost of all the system components. The initial cost of the components associated with the design variables has to be adjusted during the optimization. This was accomplished by curve fitting the cost data for 60 storage tanks, 50 power inverters, and 30 fans. Details of the cost analysis can be found in Appendix D.

$$TC = C_{init} + C_{op} \tag{49}$$

$$C_{init} = C_{coll} + C_{pumps} + C_{st} + C_{hx} + C_{DW} + C_{EW}$$
$$+ C_{fans} + C_{batt} + C_{inv} + C_{VCC} \tag{50}$$

$$C_{op} = (P_{pumps} + P_{wheels} + P_{fans} + P_{inv}) \, t_{op} C_{elect} \tag{51}$$

Table 21: Initial cost of the hybrid solar A/C components

Component	Units	Value
Solar Collector	[$]	583 [$/m^2]* A$_{coll}$ [m^2] (SHC,2006)
Pump	[$]	881 [$/kW]*(P$_{pumps}$ [kW])$^{0.4}$ (Gebreslassie et al., 2009)
Storage Tank	[$]	3.046e-006(V$_{tank}$ [gal])^3-0.005251*(V$_{tank}$)^2+2.895* V$_{tank}$ -113.9
W_A_HX	[$]	100
DW	[$]	1002
EW	[$]	1352
Fan	[$]	169
Battery	[$]	2.23[$/Ah]* N$_{batt}$ [batt]*750[Ah/batt]
Inverter	[$]	-4.37e-009(P$_{inv}$ [W])^2 + 0.0001664*(P$_{inv}$) + 0.05749
VCC	[$]	729

A multi-objective optimization problem (MOOP), as shown in Equations (52) to (54), is constructed using the two objective functions, Grid Power (*P$_{grid}$*) and the Total Cost (*TC*). The only constraints are the upper and lower bounds on the design variables.

$$\underset{x_1, x_2, x_3, x_4}{\text{Minimize}} \; f_1(\vec{x}) = P_{grid}(x_1, x_2, x_3, x_4) \tag{52}$$

$$f_2(\vec{x}) = TC(x_1, x_2, x_3, x_4) \tag{53}$$

Subject to $$\vec{x}_L \leq \vec{x} \leq \vec{x}_U \tag{54}$$

6.4   Experimentally Validated Solar Hybrid Air Conditioner Model

Prior to optimizing the complete hybrid solar air conditioner, it is important to have an experimentally validated model in TRNSYS. Models of the main components, namely, the concentrating PVT collector, the desiccant wheel, the enthalpy wheel, and the vapor compression cycle, were updated based on experimental data.

6.4.1   The Concentrating Photovoltaic/Thermal Collector

The model for the CPVT collector was experimentally investigated by Coventry (Coventry, 2005). He developed a detailed analytical model to simulate the performance of a CPVT. The change of the fluid temperature in the receiver is given by Equation (55).

$$c_{p,coll} \frac{dT}{dt} + \dot{m}_f c_{p,f}(T - T_{in}) = Q_{th} \tag{55}$$

The receiver was divided into multiple elements along its length mainly because the electrical output depends on the cells' temperatures. In order to apply Equation (55) at each element, the heat flux Q_{th} should be calculated for each element. To do so, an equivalent thermal network of the CPVT was used, Figure 73.
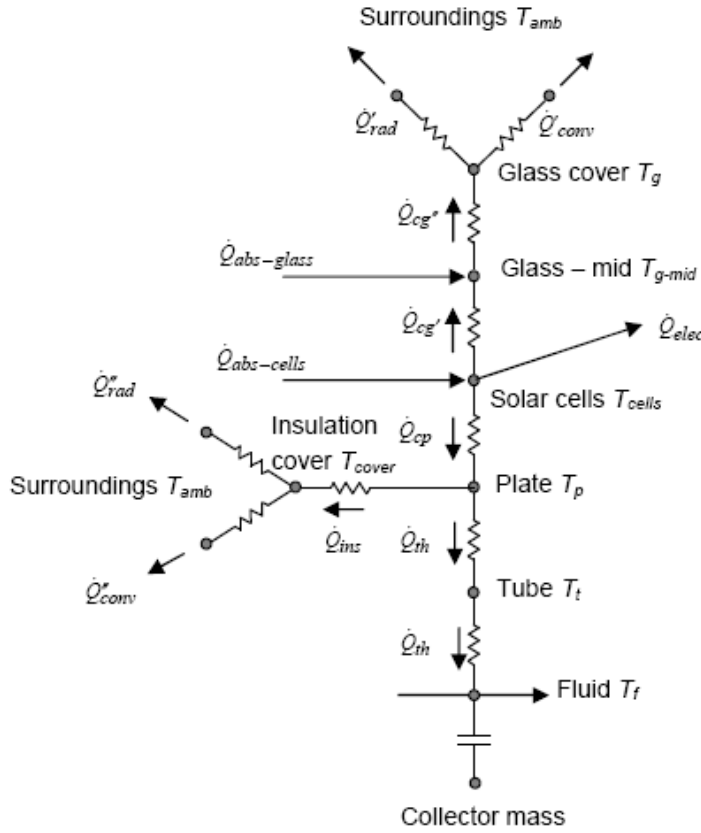
Figure 73: Thermal network of the CPVT collector (Coventry, 2005)

The thermal network can be mathematically represented by a set of nonlinear equations. The solution of these equations would provide the temperature at each node as well as the energy transferred from one node to another. The collector electrical and thermal outputs were calculated using Equations (56) to (58)

$$P_{coll} = F_{uniformity} Q_{sun} \eta_{ref} \exp(\beta (T_{cell} - T_{ref})) \tag{56}$$

$$Q_{sun} = F_{shape} F_{dirt} F_{shade} G_d A_m \rho_m \tag{57}$$

$$Q_{th} = h_{cw} A_{tf} (T_{tube} - T_f) \tag{58}$$

The heat transfer coefficient was calculated using Equation (59)

$$h_{cw} = \frac{F_H Nu_{D_h} k}{D_h} \tag{59}$$

98

where F_H was used to account for the internal fins according to the Carnavos relation and set to a value of 0.74. The Nusselt number was calculated using the Dittus-Boelter equation, Equation (60).

$$Nu_D = 0.023 \, Re_{D_h}^{0.8} \, \Pr^{0.4} \tag{60}$$

These equations were solved using MATLAB. In TRNSYS, TYPE 155, which is a subroutine used to run MATLAB scripts, was used to incorporate the CPVT model.

6.4.2 The Desiccant Wheel Cycle

There are various ways to incorporate the desiccant wheel and enthalpy wheel models into TRNSYS. For the case of the DW, the previously explained iso-potential line approach, given by Equations (19) to (22), can be updated to reflect the new Zeolite desiccant. Alternatively, the effectiveness approach could be used in which the experimental humidity ratio and temperature outlet conditions are correlated to the maximum possible potential, Equations (61) and (62).

$$\varepsilon_{DW_w} = \frac{w_1 - w_2}{w_1 - w_8} \tag{61}$$

$$\varepsilon_{DW_T} = \frac{T_1 - T_2}{T_1 - T_8} \tag{62}$$

Applying the two methods to the desiccant wheel to predict the process outlet temperature, Figure 74, and process outlet humidity ratio, Figure 75, shows a minor difference between the two methods. The conditions used refer to the test conditions shown in Table 14.
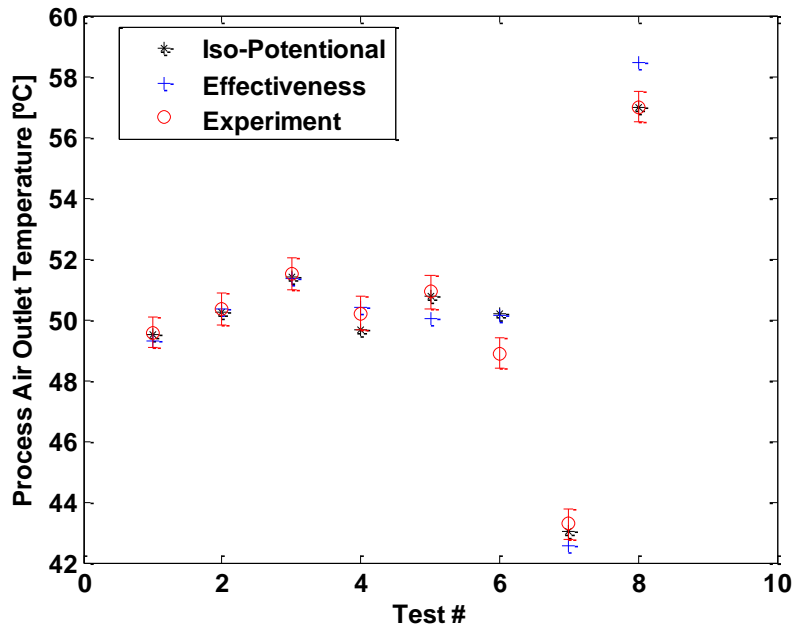
Figure 74: Desiccant wheel process outlet temperature
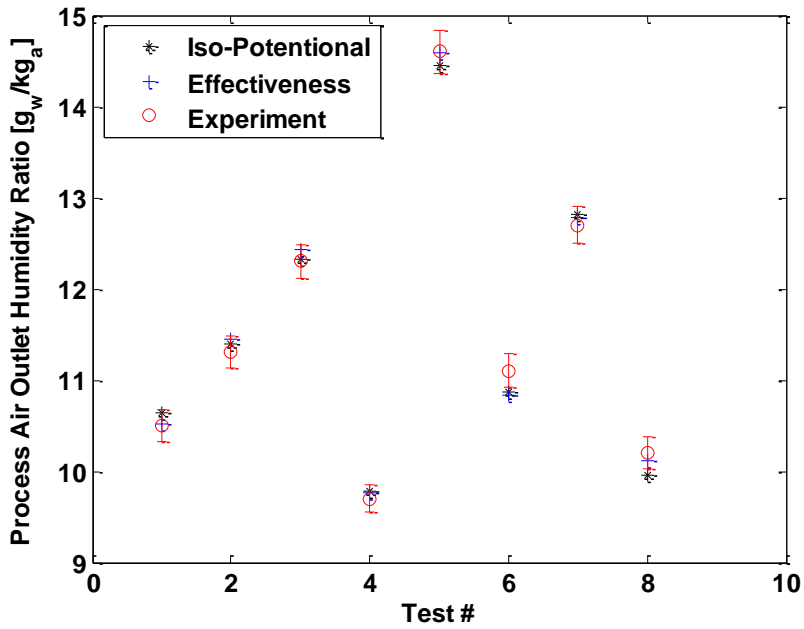
Figure 75: Desiccant wheel process outlet humidity ratio

In order to find the temperature and humidity ratio using the iso-potential lines approach, the equations have to be solved iteratively until the stopping criteria are satisfied. This implies using an initial guess to start the solver. It was found that one

initial guess might not necessarily work for all the simulated conditions. It was also found that the solution did not converge at higher humidity values. Therefore, the second approach was preferred due to its simplicity and applicability to both the desiccant and the enthalpy wheel.

In the case of the enthalpy wheel, the effectiveness method was applied to predict the temperature and humidity ratio at the process and exhuast air streams.

$$\varepsilon_{SW_w} = \frac{w_2 - w_3}{w_2 - w_6} \tag{63}$$

$$\varepsilon_{SW_T} = \frac{T_2 - T_3}{T_2 - T_6} \tag{64}$$

The temperature of the process side outlet is shown in Figure 76, whereas the humidity ratio is shown in Figure 77. Both the simulated process air outlet temperatures and the simulated process air outlet humidity ratios are maintained within ±10% of the experimental values.
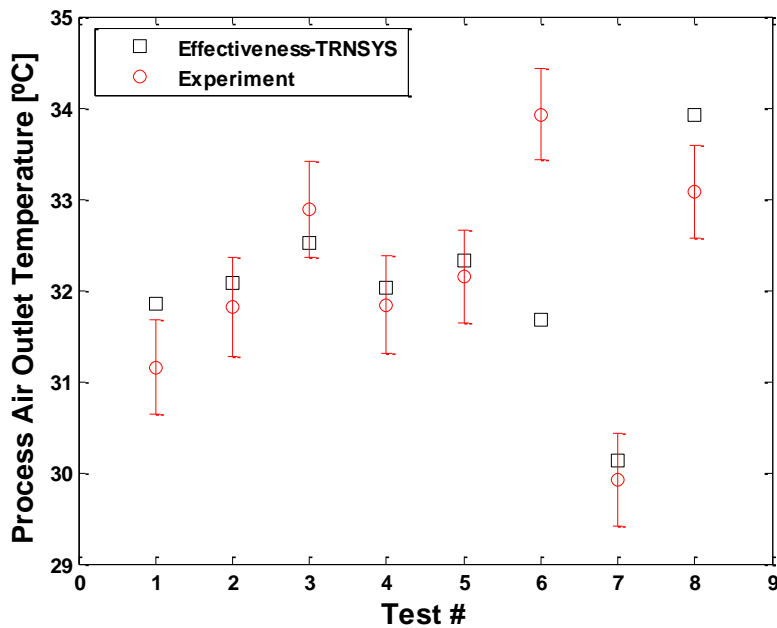
Figure 76: Enthalpy wheel process outlet temperature
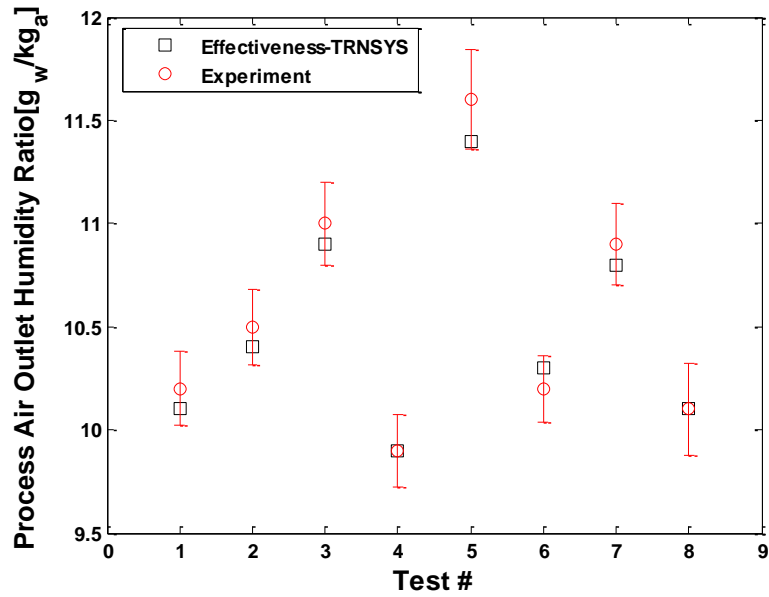
Figure 77: Enthalpy wheel process outlet humidity ratio

The exhaust air stream temperature, Figure 78, and humidity ratio, Figure 79, were also compared to the experimental results. The discrepancy is due to the leakage problem previously mentioned and due to the use of a fixed value of effectiveness for all the testing conditions.
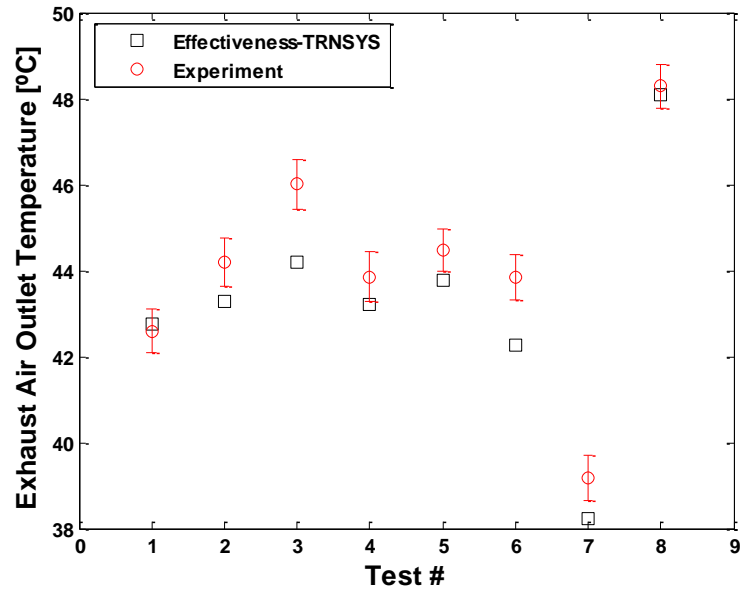
Figure 78: Enthalpy wheel exhaust outlet temperature
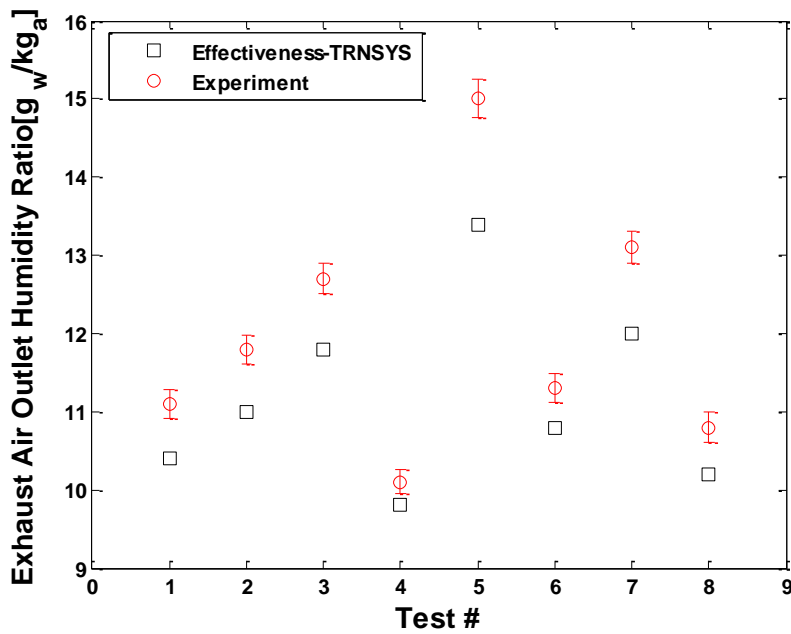
Figure 79: Enthalpy wheel exhaust outlet humidity ratio

TYPE 202 was created as a generic TRNSYS component to model any system component that can be represented by the effectiveness method. It was used to simulate the desiccant and enthalpy wheels.

6.4.3 The Vapor Compression Cycle

In order to investigate the VCC performance at different operating conditions, a separate test was conducted, Table 22. The compressor's speed was varied using the frequency inverter, whereas the superheat was changed using the electronic expansion valve. Using data acquisition software written in LabView, the temperature, pressure, refrigerant's mass flow rate, and the cycle electricity consumption, was recorded.

Table 22: VCC test matrix

Test #	T_{sh} [K]	f_{comp} [Hz]
1	3	60
2	5	60
3	10	60
4	3	50
5	5	50
6	10	50
7	5	45

In-house software, VapCyc (Winkler et al., 2008), was selected to simulate the vapor compression cycle performance. The collected experimental data were used to validate the model. Then, the model was used to simulate the VCC performance at various ambient conditions. The performance map of the VCC, created by VapCyc, was incorporated into TRNSYS.

VapCyc allows the use of detailed heat exchangers' models. Therefore, the evaporator and the condenser were simulated using in-house software, CoilDesigner (Jiang et al., 2006). The evaporator circuitry and temperature distribution is shown in Figure 80.
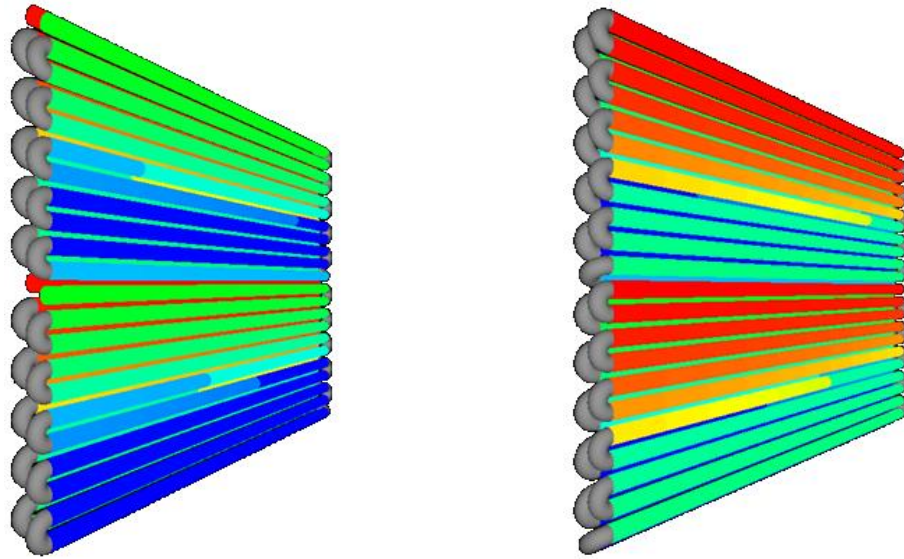
Figure 80: Evaporator circuitry and temperature distribution in CoilDesigner

Figure 81 shows the comparison between the CoilDesigner results and the experimental data for the evaporator's cooling capacity. The maximum discrepancy was 2.8% of the experimental value. The pressure drop in the evaporator was also compared to the experimental data, Figure 82. The differences range from 1-9% of the experimental values.

It has to be mentioned that CoilDesigner allows correction factors to be implemented to better match the experimental results. These correction factors are used to correct for the pressure drop and heat transfer in cases where the experimental conditions do not match the correlations' range of operating conditions, or the correlations for the refrigerant in use are not available. In the case of the evaporator, the correction factors applied to the pressure drop and the heat transfer are 1 and 0.7, respectively.
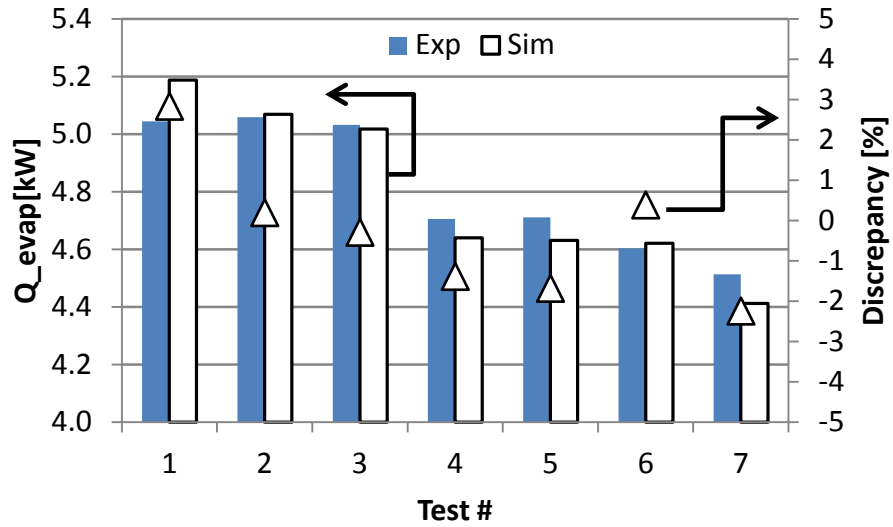
Figure 81: Evaporator capacity
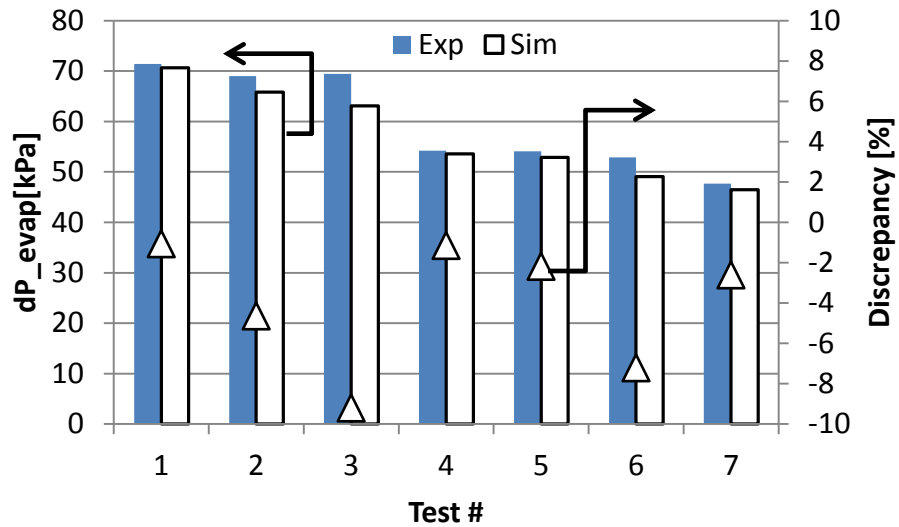
Figure 82: Evaporator pressure drop

Different applicable correlations were investigated. The most suitable ones that led to the minimum discrepancy while satisfying the testing conditions were chosen, Table 23.

Table 23: Selected evaporator's correlations

Heat Transfer		Correlation Name
Air side		Wang-Hwang-Lin/Wavy Herringbone Fin
Refrigerant	Liquid	Gnielinski
	Two Phase	Gungor-Winterton
	Vapor	Gnielinski
Pressure Drop		Correlation Name
Air side		Wang-Hwang-Lin/Wavy Herringbone Fin
Refrigerant	Liquid	Blasius-Type
	Two Phase	Friedel
	Vapor	Blasius-Type

The condenser's experimental data and measured dimensions were used in CoilDesigner to simulate its pressure drop and capacity. The condenser capacity predicted by CoilDesigner was compared to the experimental data as shown in Figure 83. The maximum discrepancy was about 3.1% of the experimental value. The condenser pressure drop was also compared to the experimental data, Figure 84, with an average discrepancy of 28% of the experimental value. A correction value of 1.3 was applied to the pressure drop and the heat transfer correlations. However, the pressure drop correlations were still unable to predict the experimental results. That was mainly due to the two phase pressure drop correlations.
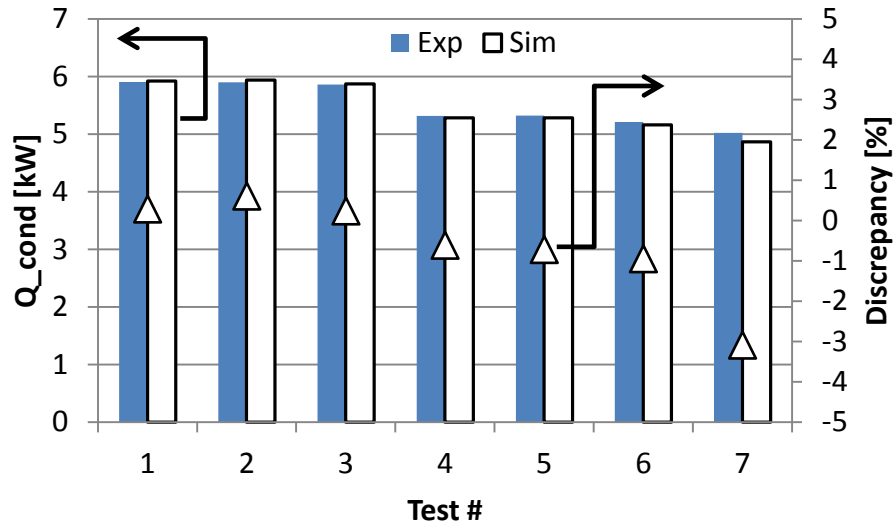
Figure 83: Condenser capacity
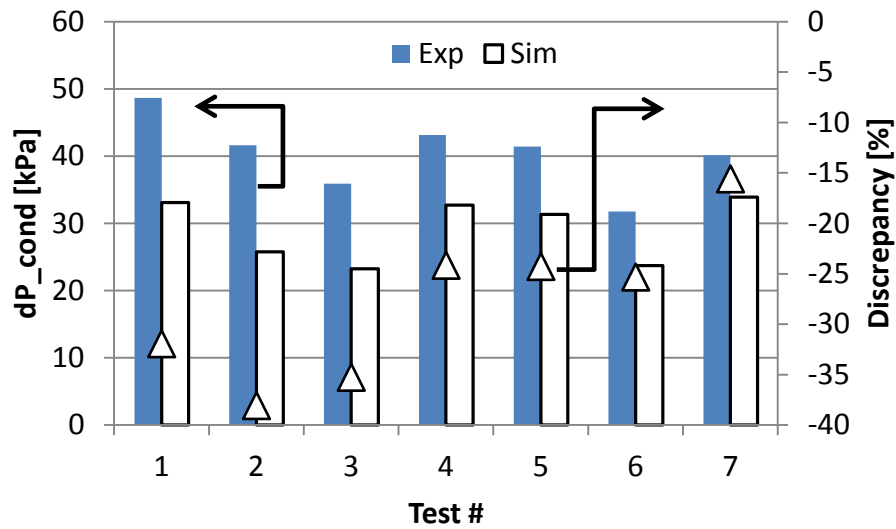
Figure 84: Condenser pressure drop

The condenser heat transfer and pressure drop correlations for the air and refrigerant

side are listed in Table 24.

Table 24: Selected condenser's correlations

Heat Transfer		Correlation Name
Air side		Wang-Tsai-Lu/Wavy Smooth Louvered Fin
Refrigerant	Liquid	Dittus-Boelter
	Two Phase	Dobson
	Vapor	Dittus-Boelter
Pressure Drop		Correlation Name
Air side		Wang-Tsai-Lu/Wavy Smooth Louvered Fin
Refrigerant	Liquid	Blasius-Type
	Two Phase	Friedel
	Vapor	Blasius-Type

The CoilDesigner models of the condenser and evaporator were used in the VapCyc model of the complete VCC, Figure 85. The remaining components are the expansion valve and the compressor. The expansion valve was model based on an isenthalpic fixed orifice model. The compressor model (Winkler et al., 2008) required experimental data to evaluate the isentropic efficiency, Equation (65), and the volumetric efficiency, Equation (66).

$$\eta_{isen} = \frac{h_{2s} - h_1}{h_2 - h_1} \tag{65}$$

$$\eta_{vol} = \frac{\dot{m}_{exp}}{\rho_1 V_{comp} R_{comp}[RPM]/60} \tag{66}$$
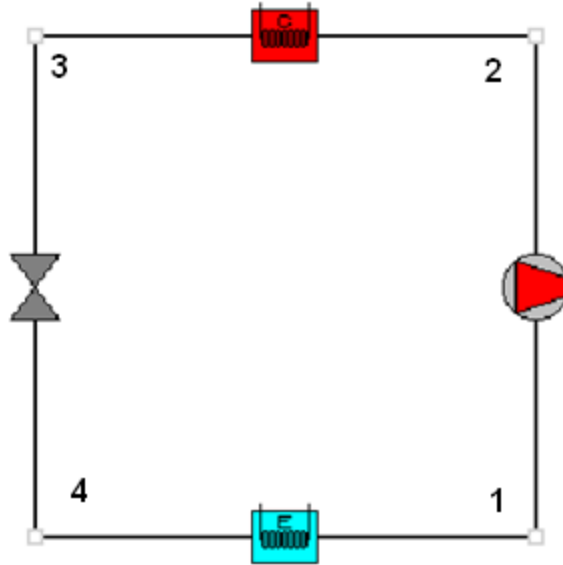
Figure 85: Vapor compression cycle in VapCyc

The VapCyc results of the evaporator capacity were compared to experimental values, Figure 86. The maximum discrepancy was maintained below the 5% of the experimental value. Similar results were found when predicting the compressor electricity consumption, Figure 87.
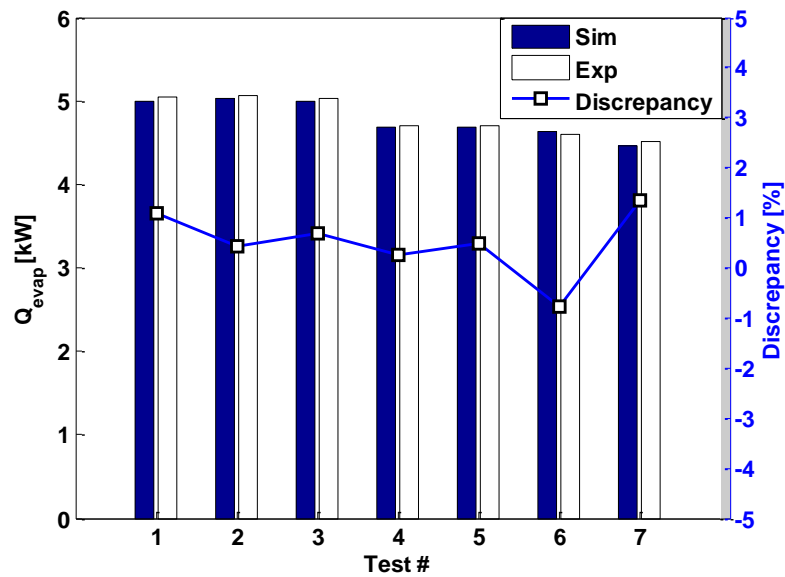
Figure 86: Evaporator cooling capacity
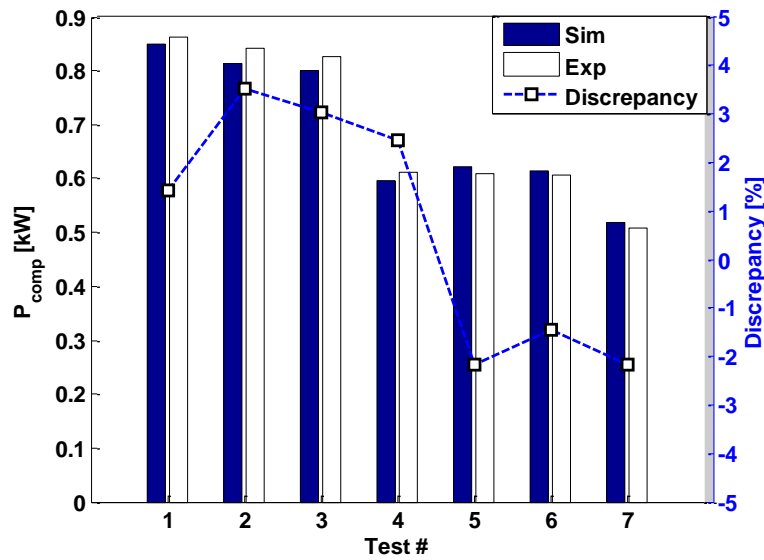
Figure 87: Compressor electricity consumption

The predicted condenser capacities were compared to the experimental value, Figure 88. Even though, the condenser capacity was not needed to construct the VCC performance map, it was important to be validated in order to ensure the cycle energy balance. In addition, the COP_{VCC} was calculated and compared to the experimental value as shown in Figure 89 with a maximum discrepancy less than 5%.
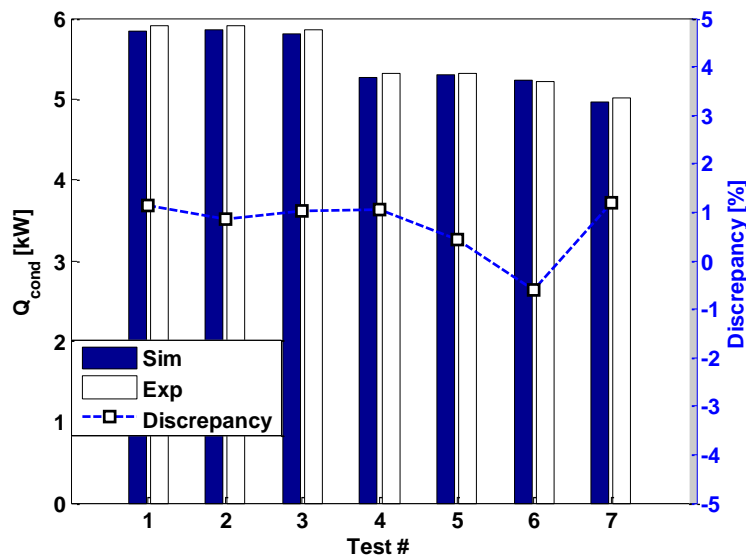
Figure 88: Condenser capacity
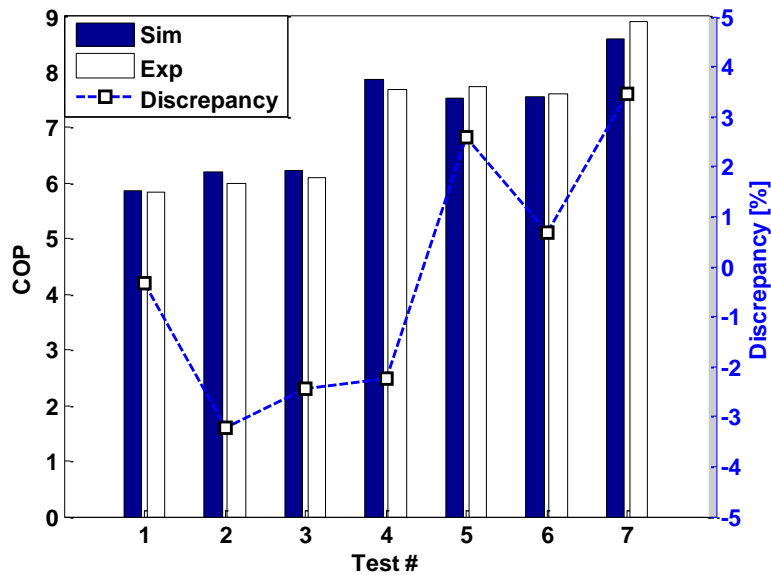
Figure 89: The experimental VCC coefficient of performance

The main purpose of the VCC model using CoilDesigner and VapCyc was to create a performance map for the VCC to be used in TRNSYS. The performance map was created by running the VCC model in VapCyc at various ambient and indoor conditions while acquiring the compressor and cooling capacity at each condition.

6.5   Results and Discussion

A representative problem, which was less time consuming and less complicated, was used to investigate the different optimization algorithms, Appendix B. The purpose of the initial investigation was to explore the dependence of the algorithms on the initial point selection. Minimization of the first objective function showed that not all the algorithms were able to converge to an optimum. The *fminsearch*, which is a local optimization technique, seemed to depend on the initial point since it converged to a local minimum. On the other hand, the *PatternSearch* (PS) and Genetic Algorithm (GA) were able to find the global minimum for all the trial initial points. The

TRNOPT was also able to converge to a global minimum as long as the initial points were inside the variables' domain. The algorithm selected in TRNOPT was the Hooke-Jeeves Algorithm, which is a modified pattern search algorithm (Wetter, 2001).

The difference between the MATLAB algorithms, *fminsearch*, PS and GA, was investigated further by a second objective function. Minimization of the second objective function showed that the minimal value was found by GA, but PS was faster. For the problem in hand, GA is preferred since it is a global optimization technique and it is capable of handling integer design variables.

The single objective function, total electrical consumption, was optimized using GA. The problem was further constrained by requiring the second objective function, the total cost, to be less than \$35,000. A fixed value penalty was assign to designs that did not satisfy the constraint. The optimum design and the minimum function value are listed in Table 25. Figure 90 shows the progress of GA toward the minimum grid energy consumption value. Only the feasible designs, which do not violate any constraint, are shown. The marker size represents the number of batteries, whereas its color represents the tank volume.

Table 25: Optimal Design specifications

Variable	Units	Value
A_{Coll}	m^2	42
$\dot{m}_{coll}$	kg/hr	1747
V_{tank}	m^3	1.6
N_{batt}	-	2
Minimum: f($\dot{x}$)	kW-hr	3,873.6
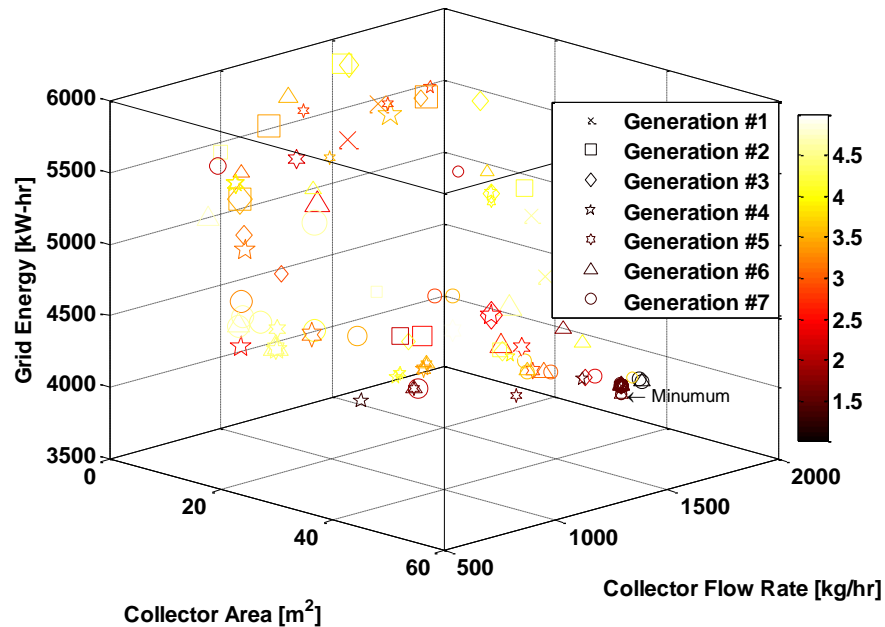
Figure 90: GA progress toward the minimum grid energy consumption

One advantage offered by coupling MATLAB and TRNSYS is the capability of handling Multi-Objective Optimization Problems (MOOP). The hybrid solar A/C MOOP was solved using the *gamultiobj* function from MATLAB, which is a Multi-Objective Genetic Algorithm (MOGA). It was also solved by an in-house developed MOGA (Aute et al., 2004). There is no single solution to MOOP, but there are a set of solutions, known as a Pareto front. All solutions on the Pareto front are optimal. Therefore, the goal of MOGA is to find the Pareto front within the design variables' bounds while satisfying the constraints. MOGA progress toward the final Pareto front is shown in Figure 91, while the final Pareto front solutions are shown in Figure 92. The solar hybrid A/C Pareto front results shows the tradeoff between the total cost and the grid energy consumption.
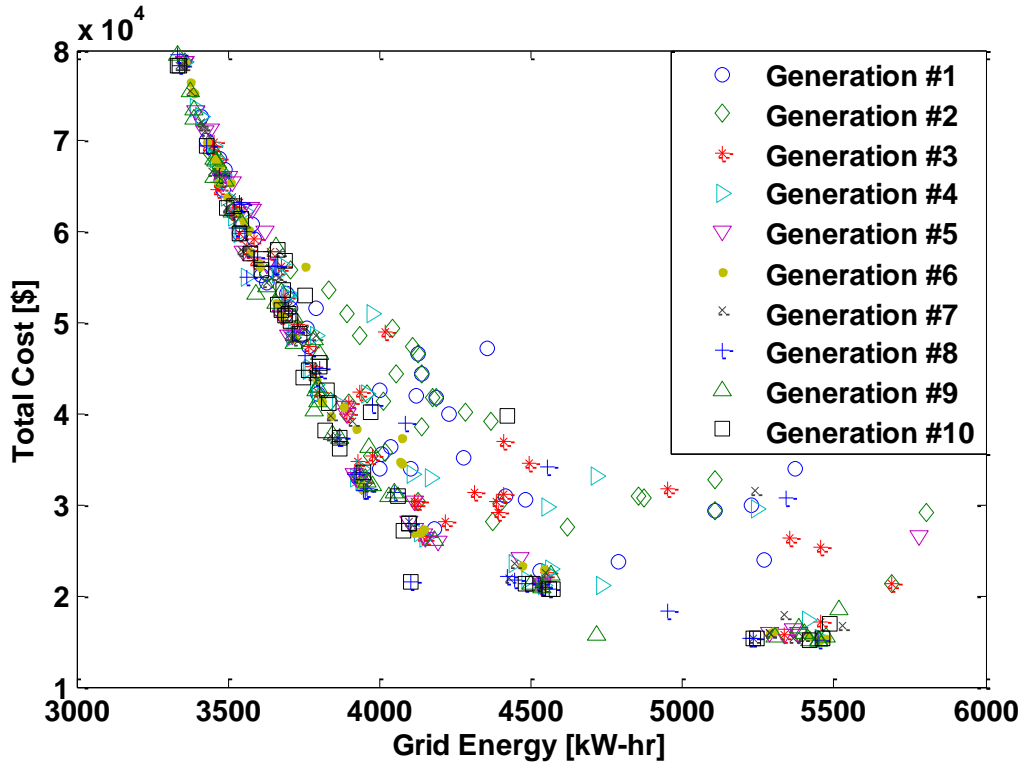
Figure 91: MOGA Pareto front progress
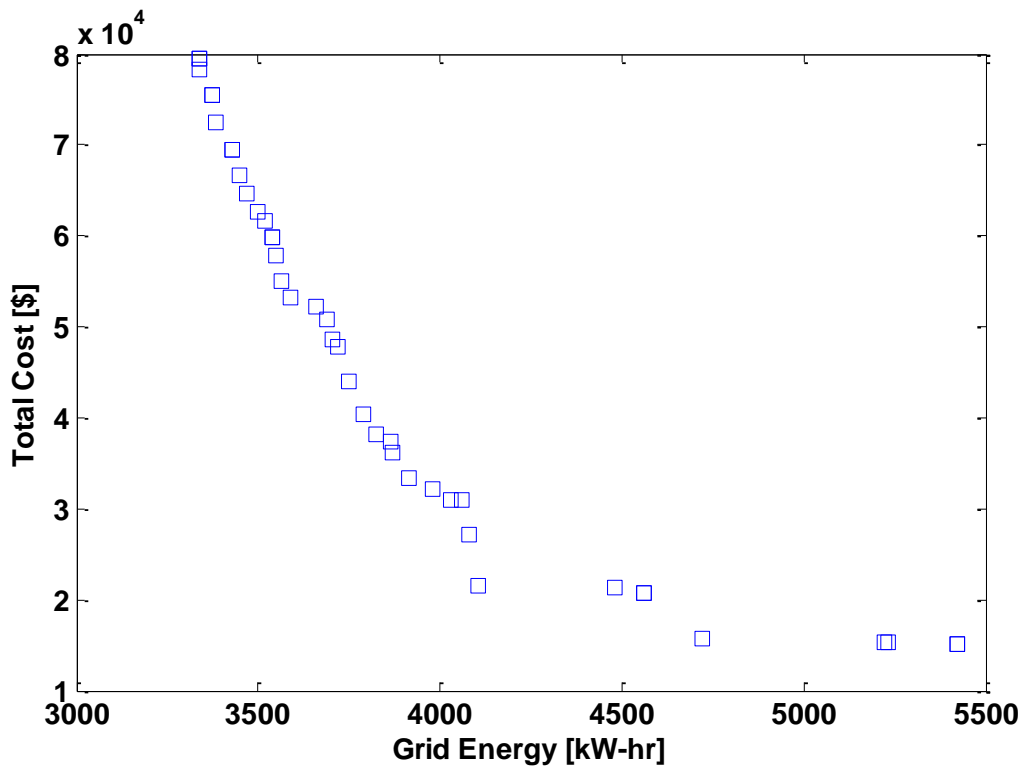
Figure 92: The solar hybrid A/C Pareto front solutions

For the same population size of 50 individuals, Figure 93 shows the results of the in-house developed MOGA compared to that of MATLAB. Since GA is heuristic by nature, Pareto fronts from the two MOGAs are not expected to coincide. This randomness effect on the Pareto front can also be noticed if the MATLAB-MOGA is run multiple times. Usually, MOGA is run for multiple times and the minimum of these runs is selected. It can be seen that both algorithms present an acceptable spread.
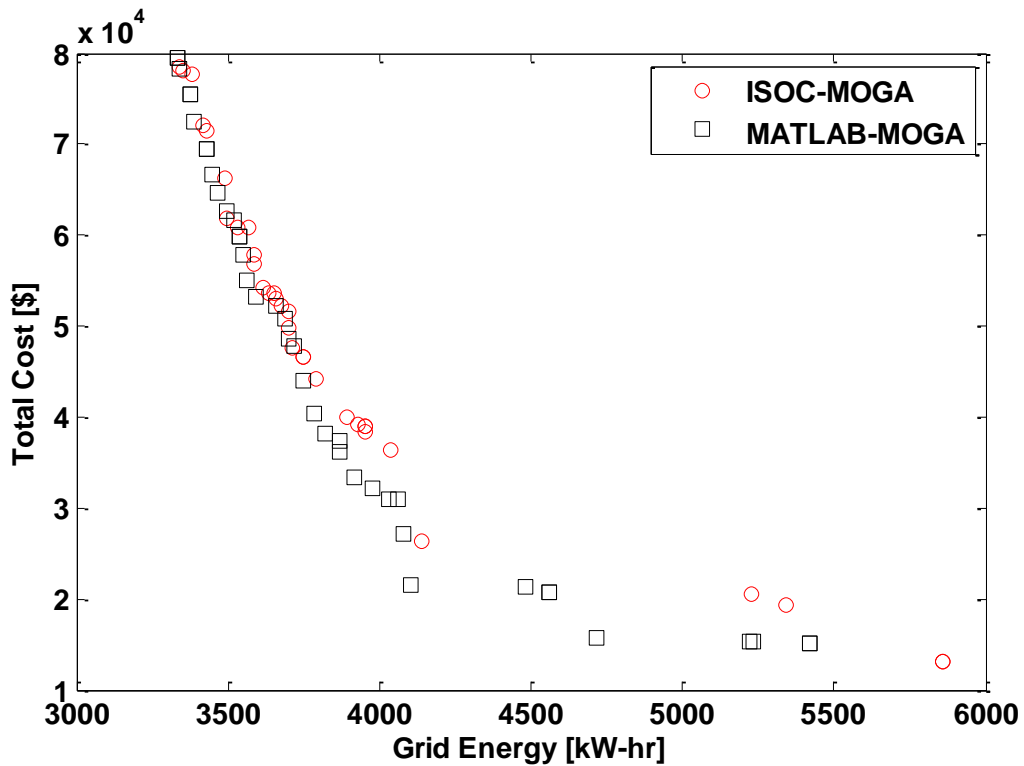
Figure 93: Comparing ISOC and MATLAB MOGA

The effect of increasing the population size is shown in Figure 94. Doubling the size of the population, from 50 to 100 individuals, does not seem to affect the Pareto front solutions significantly. However, a population size of 50 gives better results than a population size of 40, especially in finding the minimum total cost. In addition, the

results of minimizing the system power grid consumption, while keeping the cost less than $35,000, is superimposed on this figure.
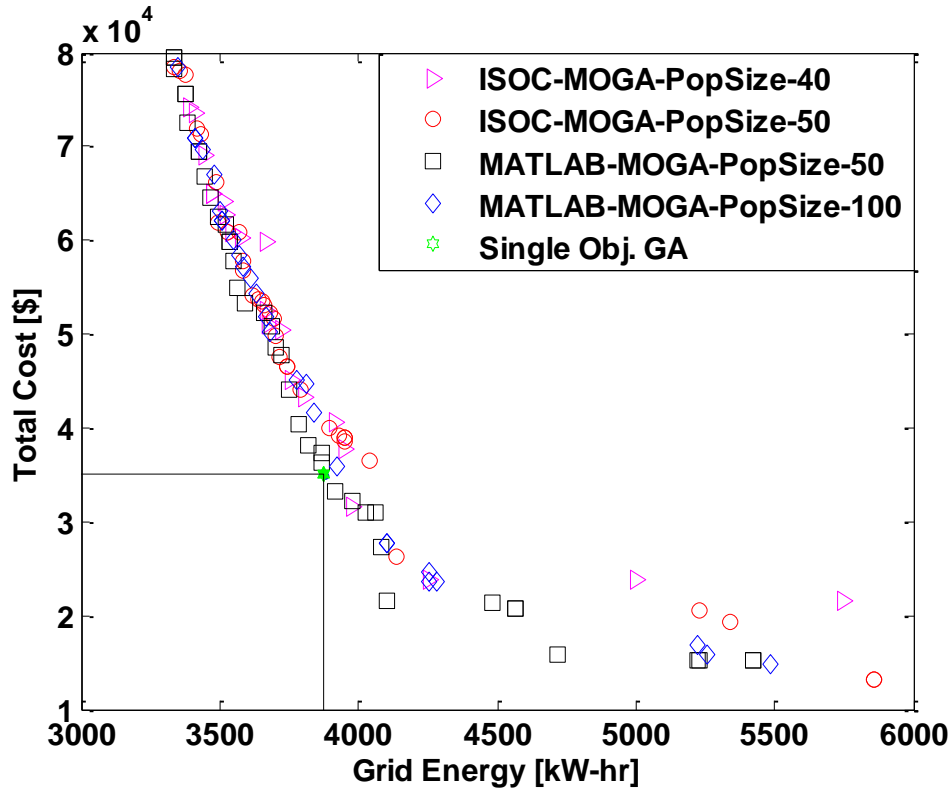
Figure 94: The effect of the population size

The optimized designs can be compared to a baseline system based on the importance of each objective function to the designer. If the total system cost is more important, designs from the lower right side of Figure 94 should be selected. For this case, the design with 4,719 kW-hr grid energy consumption and a total cost of $15,753 is selected for further investigation. A standard VCC with Seasonal Energy Efficiency Ratio (SEER) of 16 is selected as a baseline. Figure 95 shows the total cost of the hybrid solar A/C compared to that of the VCC as a function of time. The figure also shows the effect of the electricity price on the period required for the cumulative total cost of the proposed system to be less than that of the VCC. For electricity price of

0.12 $/kW-hr, the proposed system cumulative cost will be less than that of the VCC after 17.5 years of operation. As the figure indicates, the higher the electricity price, the shorter that period is.
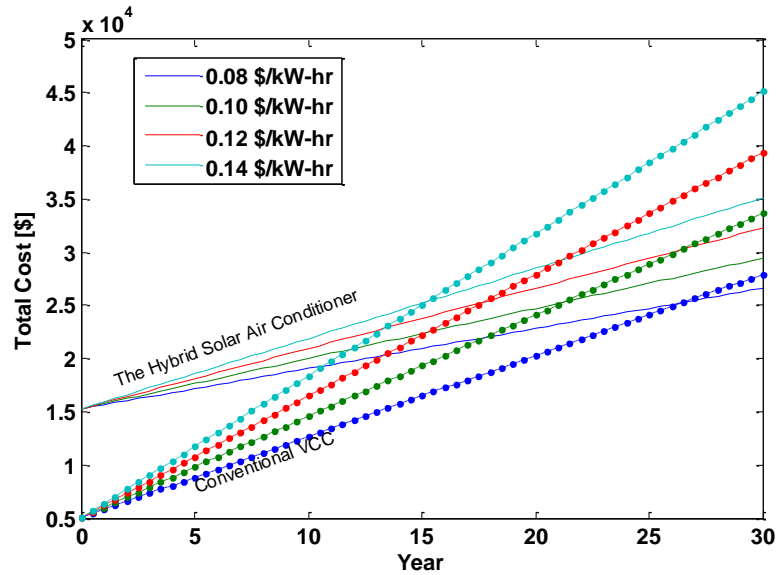
Figure 95: Total cost of the proposed system vs. conventional VCC

The total cost of the hybrid solar A/C can be allocated as shown in Figure 96. This figure helps to find the most expensive components and identify where the cost reduction efforts should focus. As the figure shows, the key component is the hybrid collector which represents 46% of the total system cost. The second most expensive component is the batteries.
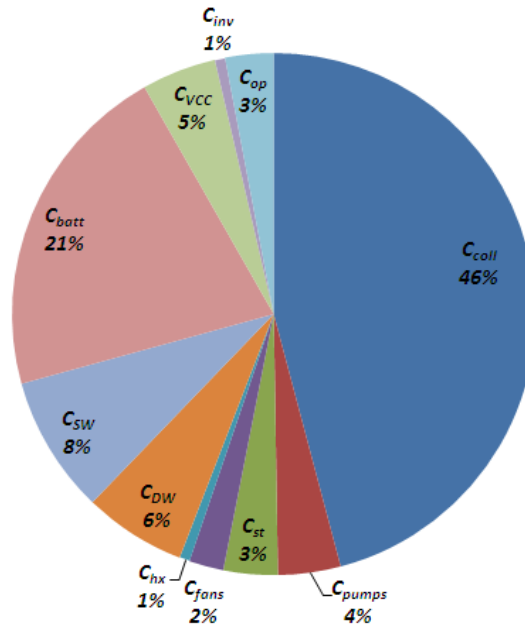
Figure 96: The hybrid A/C cost breakdown

Even though the proposed system is more expensive than the conventional VCC, it consumes less electricity and maintains better indoor comfort. The lower energy consumption reduces the peak electrical loads on utilities. It also reduces the consumer operating cost since less energy is purchased during the on peak periods. In addition, the total system cost shown in Figure 95 does not include any incentives or rebates. The total cost including federal tax incentive and some state rebates for Maryland, USA, is shown in Figure 97. The figure shows that the cumulative cost of the hybrid solar A/C is becoming less than the VCC after about 11 years of operation for electricity price of 0.12 $/kW-hr. The hybrid solar A/C design selected is able to pay back its initial investment in 24, 20, and 17 years for electricity prices of 0.10, 0.12, and 0.14 $/kW-hr, respectively. It has to be taken into consideration that the system performance and total cost are subject to change. That is because the PV cells efficiency is continuously improving and their cost is decreasing.

119
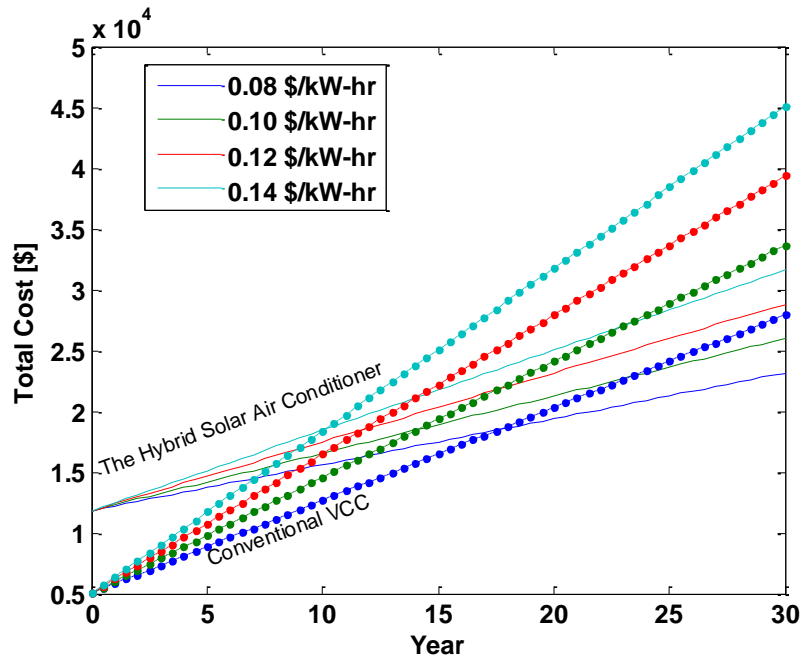
Figure 97: Total cost of the hybrid solar A/C with incentives

It has to be mentioned that the cost evaluation of the proposed system, as shown by Equations 49-51, is one of several ways of doing economic evaluations. The initial cost could have included the labor and installation cost, whereas the operating cost could have included the maintenance and parts replacements costs. In addition, the cost of electricity is assumed to be constant throughout the life of the system. However, the cost information provided in this work can be used in a more detailed economic study, such as the life cycle savings method which takes into account the time value of money and allows as many details as may be significant.

6.6   Conclusions of the Optimization Study

In order for the solar air conditioners to become a real alternative to the conventional systems, their performance and total cost has to be optimized. Various optimization methods were used to optimize an experimentally validated TRNSYS model of the

solar hybrid air conditioner. Minimizing the grid energy consumption of the system showed that MATLAB is capable of finding comparable results to that of TRNOPT. It was also shown that GA is preferred over Pattern Search algorithms since GA is a global optimization technique and it is capable of handling integer design variables. The advantage of coupling MATLAB and TRNSYS compared to using the TRNSYS optimizer was demonstrated by solving a multi-objective optimization problem. The tradeoff between the system performance and its cost was presented by a Pareto front. This Pareto front allows the designer to estimate the cost of the system based on the desired amount of load to be covered by solar energy. In addition, the results show that coupling TRNSYS and MATLAB expands TRNSYS optimization capability in solving more complicated optimization problems. It also provides more flexibility in formulating the optimization problems.

From the Pareto front, a design with a minimum cost is compared to a standard VCC with SEER of 16. The concentrated PV/T solar collector and batteries represents 46% and 21% of the hybrid solar A/C's total cost, respectively. For an electricity price of 0.12 $/kW-hr, the hybrid solar A/C's cumulative total cost will be less than that of the VCC in 17.5 years. However, this period is reduced to about 11 years once the federal tax incentive and some Maryland state rebates are applied. These periods are shortened if the electricity price increases. The hybrid solar A/C is able to pay back its initial investment in 24, 20, and 17 years for electricity prices of 0.10, 0.12, and 0.14 $/kW-hr, respectively

7. Summary and Conclusions

The main objective of this study is to search for a high coefficient of performance of solar air conditioners (A/C). This objective has been accomplished and the conclusions are summarized as follows:

7.1 Simulation Study

The simulation of the novel hybrid solar air conditioner was carried out using TRNSYS simulation program. In addition, a vapor compression cycle (VCC) driven by photovoltaic (PV) panels and an absorption cycle driven by evacuated tubes collector were simulated in TRNSYS for the sake of comparison. The results of the simulation study are as follows:

- A parametric study of the hybrid solar air conditioner showed that the CPVT collector area is the most important parameter that affects the system performance. However, other design variables such as, the hot water storage, number of batteries, and collector mass flow rate, have to be sized based on the solar collector area in order to obtain the optimum performance.

- Integrating a desiccant wheel cycle (DWC) with a conventional VCC is more effective than the standalone VCC in ensuring comfort of buildings in hot and humid climates.

- The size of the VCC should be reduced, if it is coupled with a DWC. That is because the VCC has to only accommodate the sensible loads.

- Comparing the COP of the hybrid solar air conditioner to that of the most common solar A/Cs showed that it is higher than that of a VCC powered by PV panels and a solar absorption system. The yearly average cooling COP of the hybrid solar air conditioner, the solar VCC, and the solar absorption cycle are found to be 0.68, 0.34 and 0.29, respectively.

7.2 Experimental Study

The experimental study was divided into two parts: desiccant wheel cycle (DWC) testing and the complete hybrid A/C testing. The purpose of the first test was to identify the most important variables that affect the cycle performance. The effect of the process air stream conditions, the regeneration temperature, the mass flow rate, and the desiccant wheel rotational speed on the cycle performance was studied. The conclusions of the first part of the experimental study are as follows:

- The highest desiccant wheel capacity of 1.96 kW was obtained for the lowest process air stream temperature. The high capacity does not necessarily ensure sufficient dry conditions at the desiccant wheel process air stream outlet.

- The highest latent coefficient of performance for the desiccant wheel was 1.28, which is obtained for the lowest regeneration temperature case.

- The desiccant wheel capacity and latent coefficient of performance did not vary much with rotational speed between 20-30 RPH.

- The average enthalpy wheel effectiveness for all the tests was found to be 0.71.

The effect of the ventilation mass flow rate and the ambient air temperature and humidity ratio on the hybrid A/C performance was investigated. The performance of the hybrid A/C system was also compared to that of a standalone VCC. The conclusions of the second part of the experimental study are as follows:

- The standalone VCC was not able to maintain the comfort conditions under ARI's humid conditions. However, the comfort zone was reached when the desiccant wheel cycle was activated. This indicates that the standalone VCC has to be oversized in order to control the humidity and temperature simultaneously.

- At different ambient conditions, the hybrid A/C system was found to be very effective in keeping the indoor conditions within the comfort zone. These results agreed with TRNSYS simulation of the complete hybrid A/C.

- Using the experimental data, the overall coefficient of performance COP_{sys} of the hybrid A/C powered by a hybrid solar collector was calculated. A COP_{sys} value more than 1.0 was found to be achievable. In the worst case scenario, the COP_{sys} was found to be less than unity, but still double that of the most common solar A/Cs.

7.3 Optimization Study

The TRNSYS model of the hybrid solar air conditioner was validated using the experimental data. Various optimization methods were investigated to optimize the

124

proposed system's performance and total cost. The findings of the optimization study are as follows:

- For single objective optimization problems, MATLAB is capable of finding comparable results to that of TRNSYS optimizer.

- Among MATLAB algorithms, Genetic Algorithm (GA) is preferred over Pattern Search algorithms since GA is a global optimization technique and it is capable of handling integer design variables.

- The advantage of coupling MATLAB and TRNSYS over using the TRNSYS optimizer was demonstrated by solving a multi-objective optimization problem.

- The tradeoff between the hybrid solar A/C performance and its cost was presented by a Pareto set. This set allows the designer to estimate the cost of the system based on the desired amount of load to be covered by solar energy.

- In addition, the results show that coupling TRNSYS and MATLAB expands TRNSYS optimization capability in solving more complicated optimization problems. It also provides more flexibility in formulating the optimization problems.

- Comparing a design with a minimum cost to a standard VCC with SEER of 16 shows that the proposed system's cumulative total cost is projected to be less than that of the VCC in 17.5 years of operation. However, this period is

reduced to about 11 years once the federal tax incentive and some Maryland state rebates are applied.

- The hybrid solar A/C is able to pay back its initial investment in 24, 20, and 17 years for electricity prices of 0.10, 0.12, and 0.14 $/kW-hr, respectively

- Cost allocation of the minimum cost design shows that the concentrated PV/T solar collector and batteries represents 46% and 21% of the hybrid solar A/C's total cost, respectively.

8. List of Major Contributions and Future Work

8.1 **Major Contributions**

Overall, this study provides an alternative way of looking at solar air conditioning. It suggests that in order to improve the performance of solar air conditioners (A/Cs), hybridization can be used instead of focusing on improving a single component or a single cycle in the traditional solar A/Cs. The benefits from hybridization is not only limited to the performance, but also includes better control of the indoor temperature and humidity ratio that ensures comfort. The hybridization of solar technologies and the synergy due to combining the appropriate cooling technology led to the high coefficient of performance (COP) of the proposed system. The required tasks to accomplish this goal resulted into the following major contributions:

- Innovative approach for solar A/Cs essentially doubling the COP of the current solar A/Cs, especially in hot and humid conditions. Attaining this contribution led to one conference paper, two journal publications, and one invention disclosure:

  o Al-Alili, A., Hwang, Y. , Radermacher, R., Kubo, I. , Rodgers, P. , (2008), High Efficiency Solar Cooling Technique", Second International Energy 2030 Conference, Abu Dhabi, U.A.E., November 4-5

  o Hwang, Y., Radermacher, R., AlAlili, A., Kubo, I., (2008). Review of Solar Cooling Technologies. HVAC&R Research 14, 507-528.

- o Al-Alili, A., Hwang ,Y., Radermacher, R., Kubo, I.,(2012), A high efficiency solar air conditioner using concentrating photovoltaic/thermal collectors, Applied Energy, 93, 138–147

- o Office of Technology Commercialization, (2008), "Advanced Solar Cooling Technology", University of Maryland, PS-2008-055

- A hybrid air conditioner which consists of a desiccant wheel cycle and a sensible vapor compression cycle (VCC) has been built. The performance of both cycles has been experimentally investigated under various operating conditions.

- Performance characterization of a new desiccant material which has a very low regeneration temperature, as low as 45°C, and a unique isotherm. A detailed analysis of the desiccant wheel performance has been discussed in the following paper:

  - o Al-Alili, A., Hwang, Y., Radermacher, R., (2012), Experimental Investigation Of A Desiccant Wheel Cycle, Proceedings of the ASME 2012 International Mechanical Engineering Congress & Exposition, Texas, USA, November 9-15. (Accepted)

- Unlike previous solar A/Cs studies, which mostly focus on the system performance, the indoor comfort has been taken into consideration. The experimental results of investigating the performance of the hybrid air conditioner has been discussed in the following paper:

- o Al-Alili, A., Hwang, Y., Radermacher, R., (2013), Experimental Investigation of A Hybrid Air Conditioner for Hot and Humid Climates, ASHRAE Winter Conference, January 26-30, Dallas, Texas. (To be Submitted)

- The experimentally validated simulation has been used to optimize the system performance and cost. Handling of multi-objective functions has been made possible by expanding the optimization capability of a widely used simulation tool for solar application. The optimization study have been described in the following papers

  - o Al-Alili, A., Hwang, Y., Radermacher, R., Kubo, I., (2010). Optimization of a solar powered absorption cycle under Abu Dhabi's weather conditions. Solar Energy 84, 2034-2040.

8.2 Future Work

Even though this thesis continues to improve solar air conditioners, the following would further develop the proposed system:

- The current TRNSYS simulation of the complete hybrid solar air conditioner takes about 20-30 minutes. It would be important to reduce the computational time, if larger scale optimization problems are needed to be solved. One improvement that might reduce the computational time is to implement the concentrated photovoltaic/thermal collector model in FORTRAN.

- The range of the desiccant wheel regeneration temperatures suggests that the solar sub-system might be utilized to provide domestic hot water. This would increase the energy savings further.

- An investigation on the effect of different enthalpy wheel on the desiccant wheel cycle performance can be carried out experimentally. This would help establish a guide on enthalpy wheel selection when coupled with a desiccant wheel.

- The optimization tool discussed is capable of handling more than two objective functions. Therefore, the environmental impact of the traditional and solar air conditioners can be added.

- The proposed system has many components that need to be controlled. Since the system's response to various operating conditions has been investigated experimentally, system control investigation would be the natural next step. The optimization tool explained in this thesis could be used to find the optimal set points for the controllers.

Appendices

Appendix A: Nozzle Calibration

The nozzle calibration was carried out based on ASHRAE Standard 41.2 (ASHEAE, 1992). The experimental setup had 4 nozzles at states number 1, 2, 6, and 9. The actual mass flow rates as a function of the nozzle pressure drops are shown in Figures A-1 to A-4, respectively.
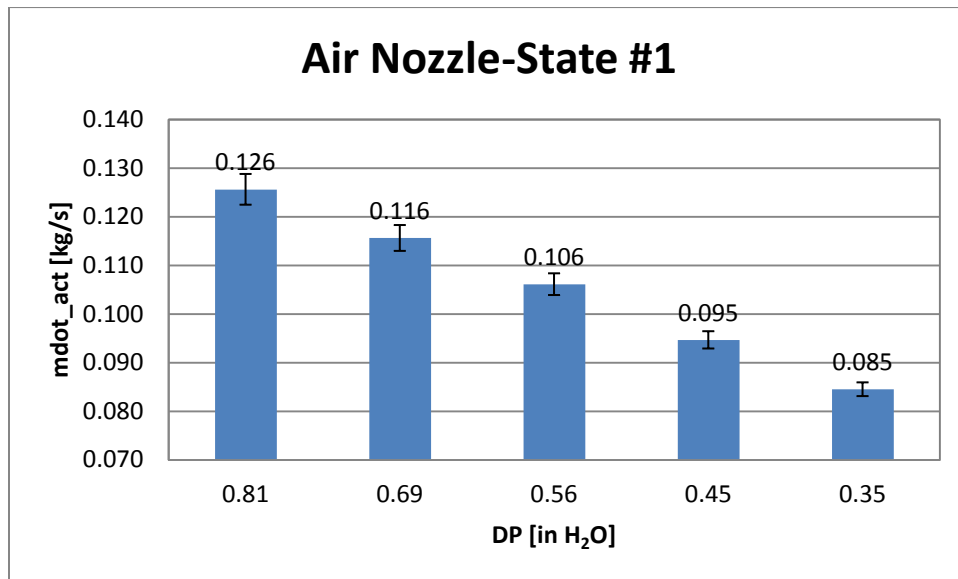

Figure A-1: Actual mass flow rate at state 1 vs. nozzle's pressure drop

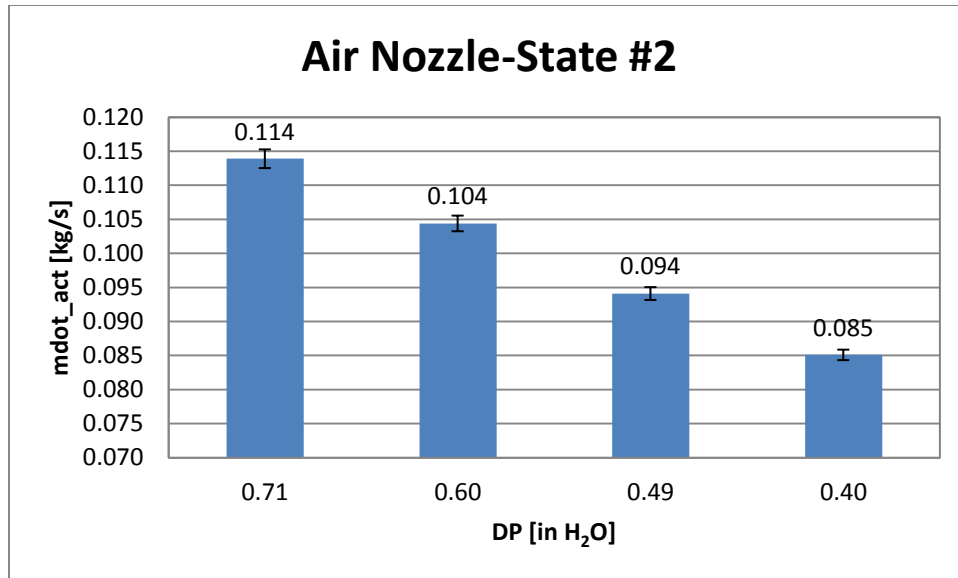Figure A-2: Actual mass flow rate at state 2 vs. nozzle's pressure drop
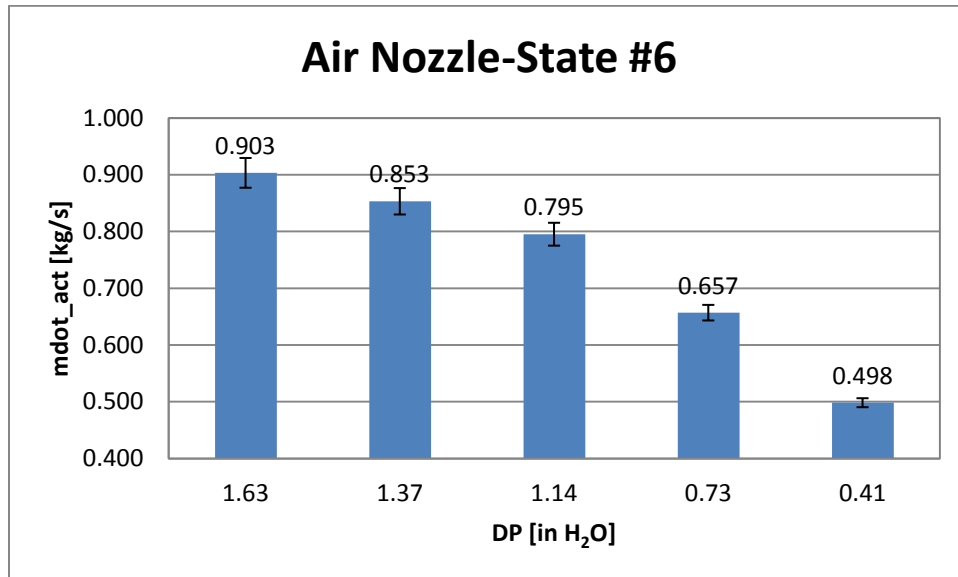
Figure A-3: Actual mass flow rate at state 6 vs. nozzle's pressure drop
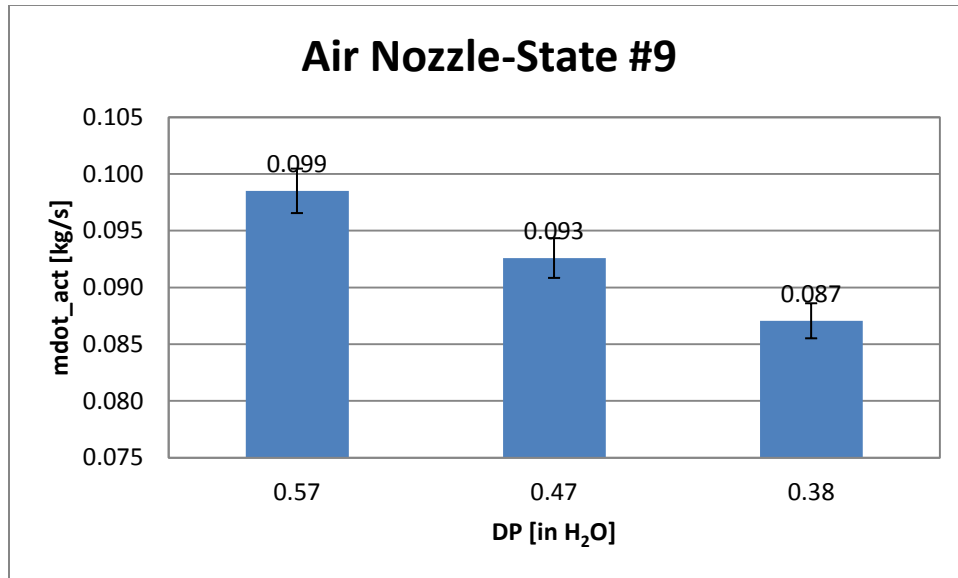
Figure A-4: Actual mass flow rate at state 9 vs. nozzle's pressure drop

The corresponding Nozzle discharge coefficients are shown in Figures A-5 to A-8, respectively.

Figure A-5: Nozzle discharge coefficient at state 1 vs. nozzle's pressure drop
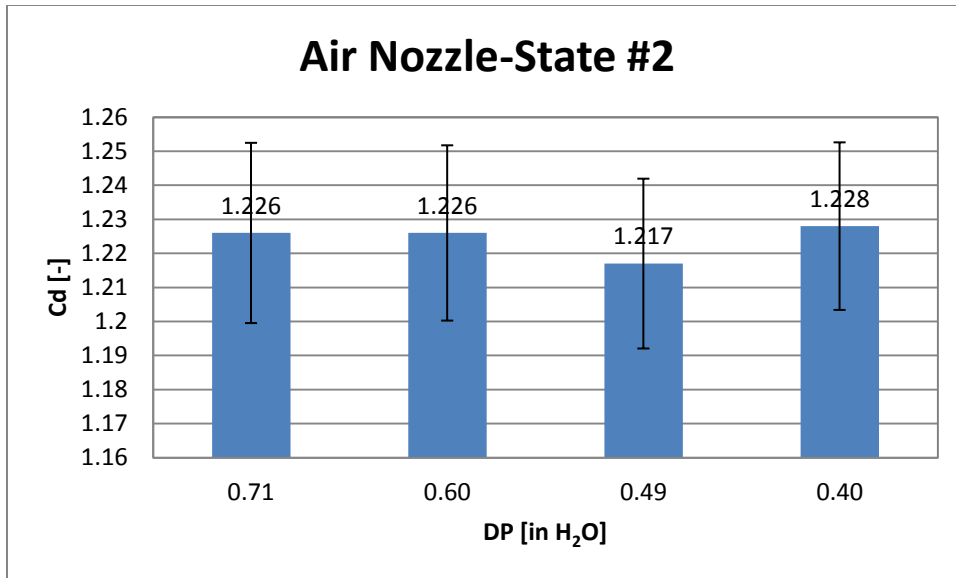
Figure A-6: Nozzle discharge coefficient at state 2 vs. nozzle's pressure drop
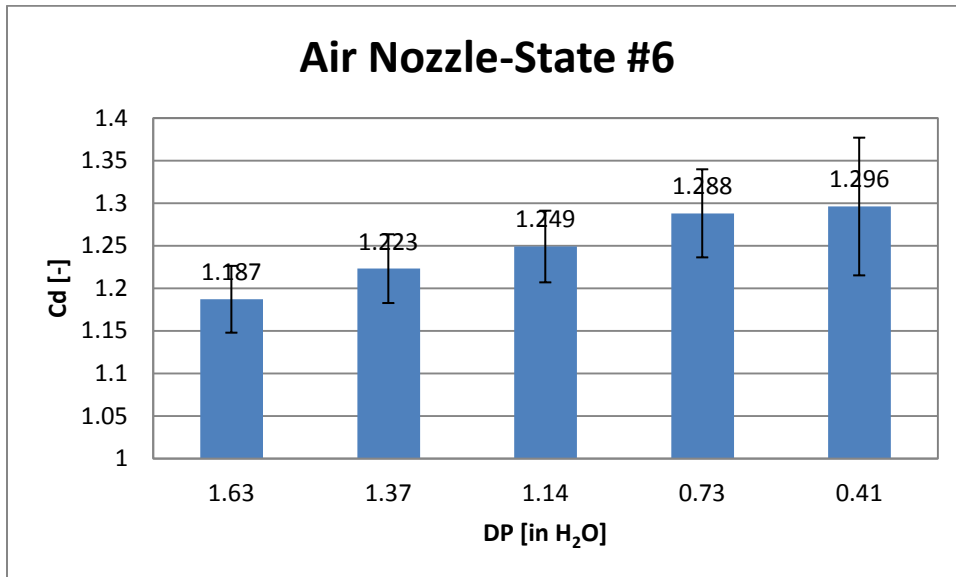
Figure A-7: Nozzle discharge coefficient at state 6 vs. nozzle's pressure drop

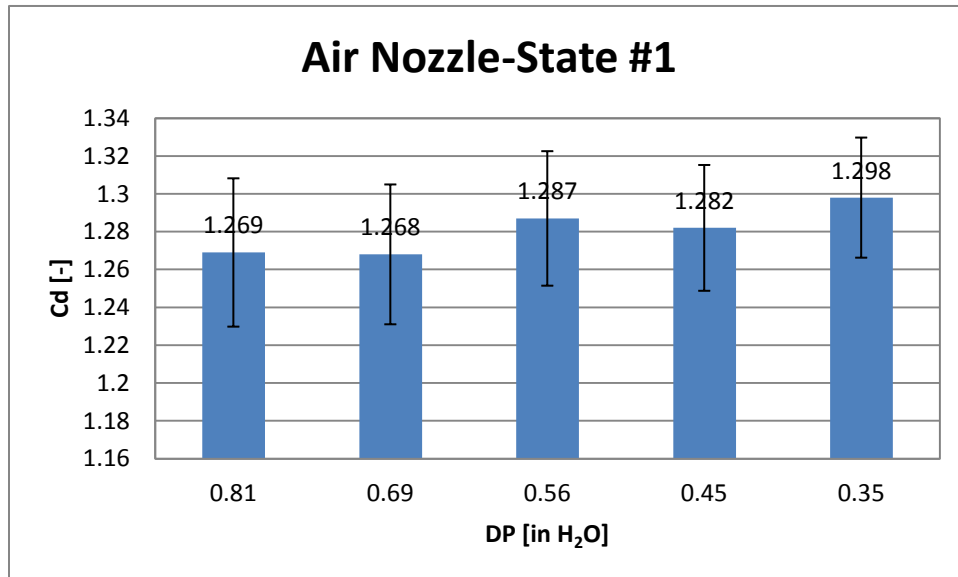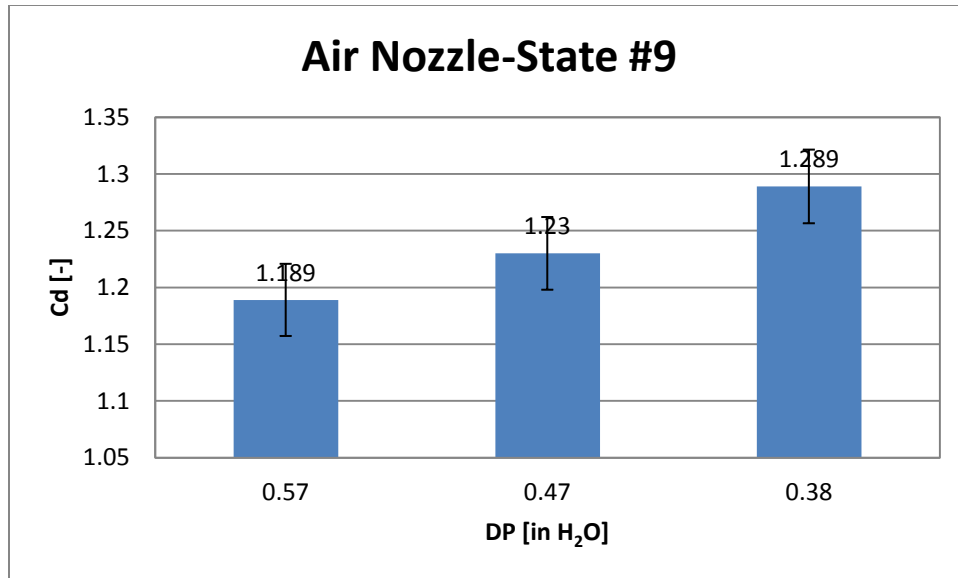Figure A-8: Nozzle discharge coefficient at state 9 vs. nozzle's pressure drop

Appendix B: Sample Optimization

A Solar Powered Absorption Cycle (SPAC) is modeled and optimized using TRNSYS based on the Typical Meteorological Year 2 (TMY2) data for Abu Dhabi, Figure B-1. Two single objective functions are defined and solved individually for SPAC which are to minimize the system electrical consumption and minimize its total cost, Equations (1-4). Then, a multi-objective optimization problem (MOOP) is constructed by the two single objective functions and the solutions are presented as Pareto points.
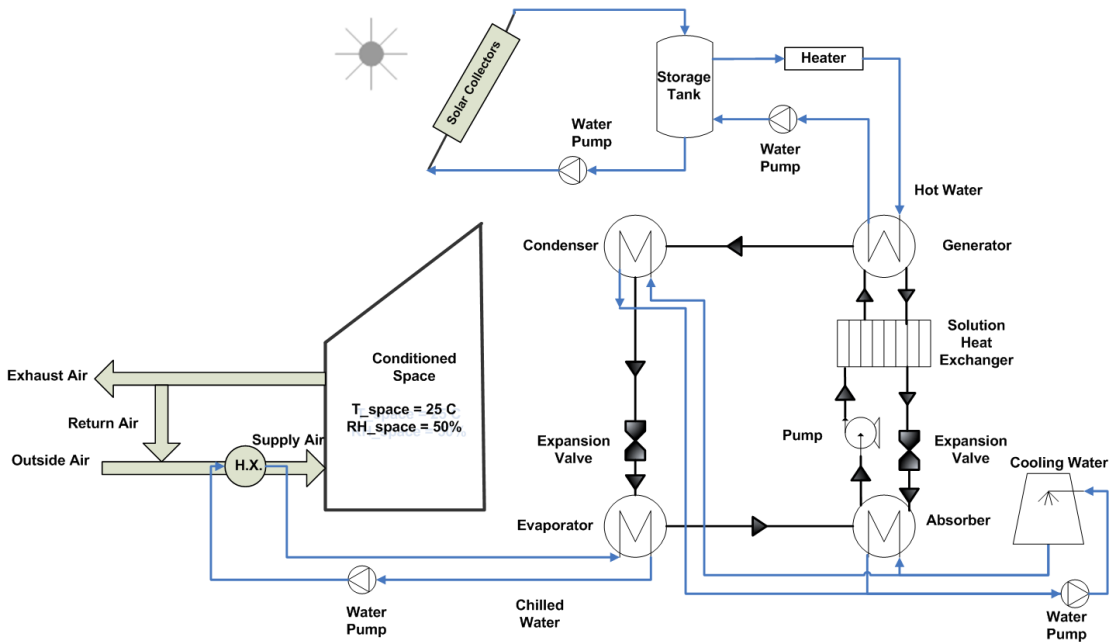
Figure B-1: Solar Powered Absorption Cycle

$$TC = C_{in} + C_{Op} \tag{1}$$

$$C_{in} = C_{sc} + C_{st} + C_p \tag{2}$$

$$C_p = k\, W_p^{0.4} \qquad \text{(Gebreslassie et al., 2009) (3)}$$

$$C_{op} = C_e W_p t_{op} \tag{4}$$

Four different algorithms are used to optimize the first objective function. In addition, Four different initial points are selected to explore the dependence of the algorithms on the initial point selection. It has to be noted that the first point is selected intentionally outside the variables' domain whereas the other three initial points are selected within the variables' domain. Figure B-2 shows that not all the algorithms are able to converge to an optimum. The *fminsearch*, which is a local optimization technique, seems to depend on the initial point since it converges to a local minimum for the last two points. On the other hand, the PS and GA are able to find the global minimum for all the trial initial points. The TRNOPT is also able to converge to a global minimum as long as the initial points are inside the variables' domain. The algorithm selected in TRNOPT is the Hooke-Jeeves Algorithm, which is a modified pattern search algorithm (Wetter, 2001).
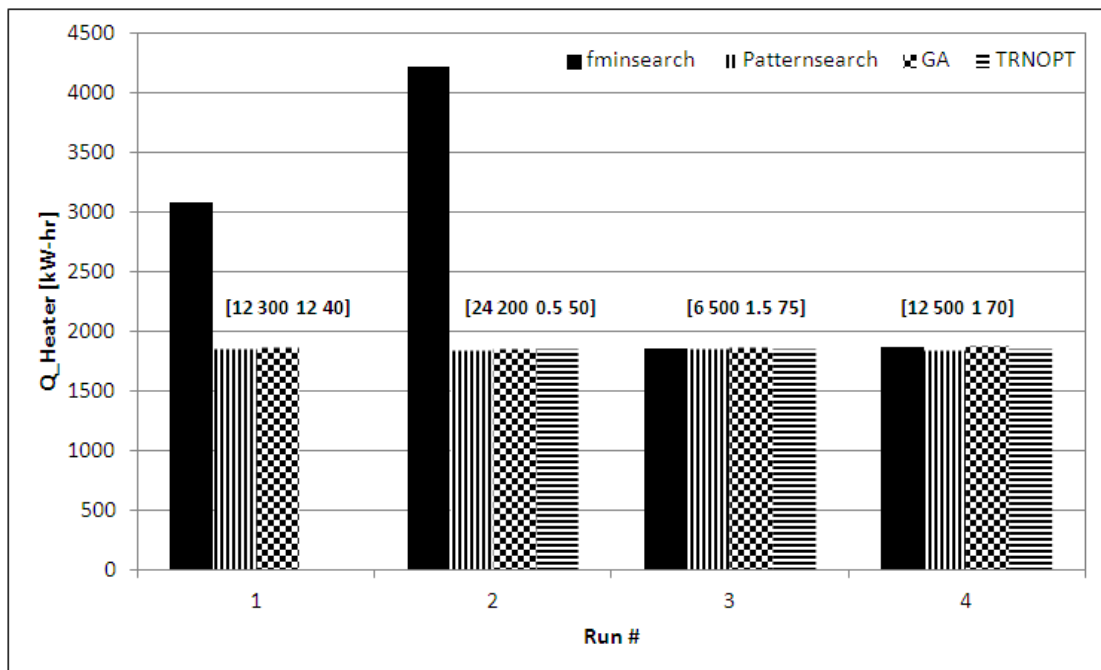
Figure B-2: Electrical heater consumption minimization

The difference between the MATLAB algorithms is investigated further by the second objective function. Figure B-3 shows the results obtained for four different initial points. A minimum solar fraction of 0.5, Equation (5), is used as a constraint. Even though, the minimal SPAC cost is found by the GA, the PS is preferred in this problem since it is faster and its optimal is very close to that of the GA.

$$SF = \frac{L_o - L_A}{L_o} \tag{5}$$
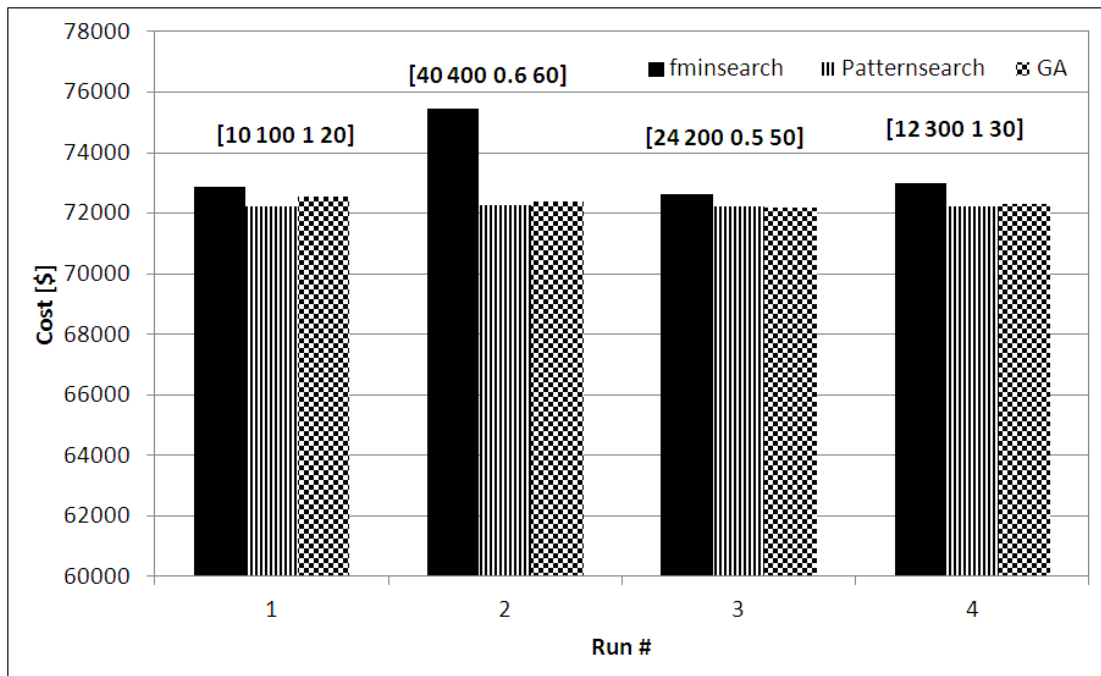
Figure B-3: Total cost minimization results

Appendix C: VCC Charge Optimization

The vapor compression cycle charge optimization was done in accordance with ASHRAE standard 116 (ASHEAE, 2010). The cycle coefficient of performance and the corresponding cooling capacity are showen in Figures C-1 and C-2.
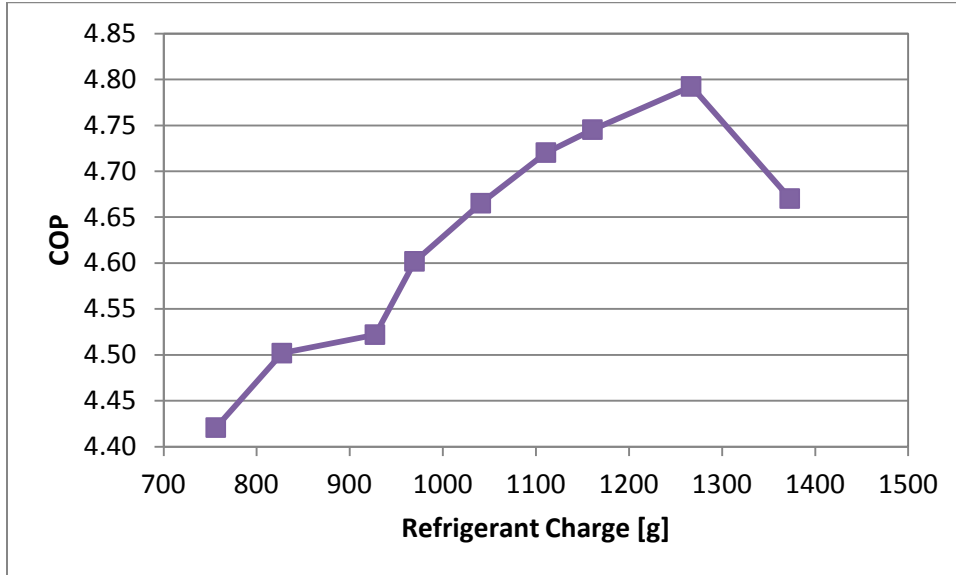
Figure C-1: COP as a function of refrigerant charge
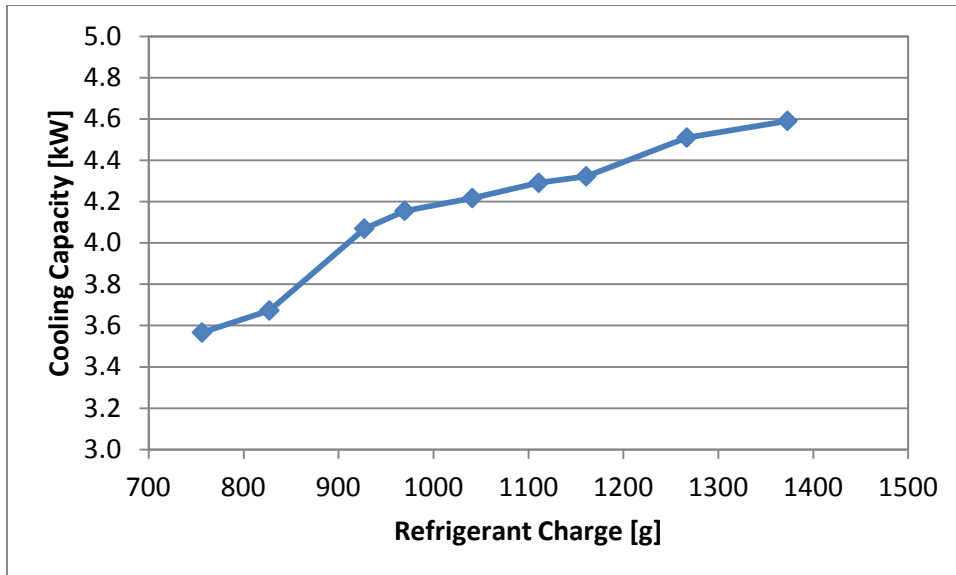
Figure C-2: Cooling capacity as a function of refrigerant charge

139

Once the optimum refrigerant charge was obtained, the refrigerant was recovered and the charging was repeated. Figure C-3 and C-4 shows the COP and cooling capacity for the second refrigerant charging.
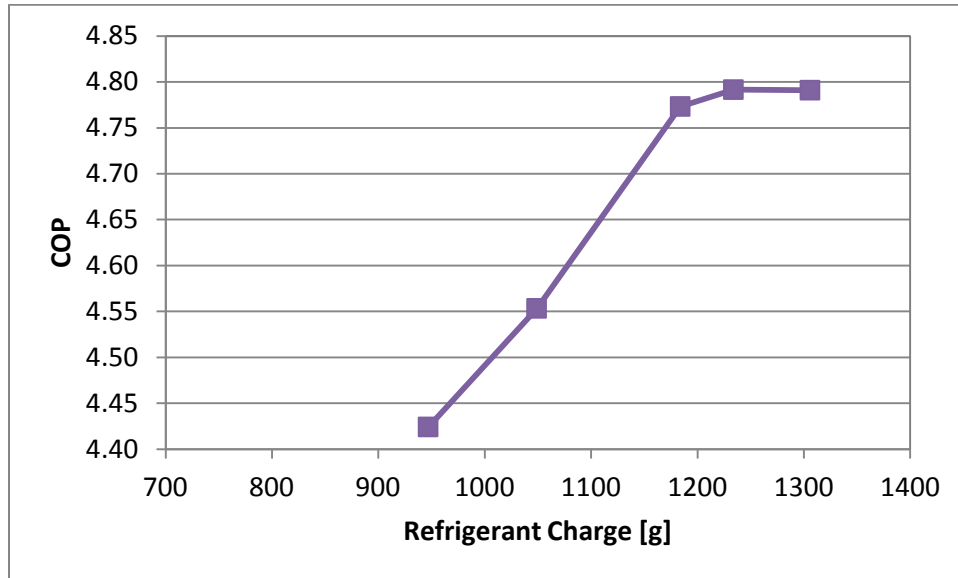
Figure C-3: COP as a function of refrigerant charge
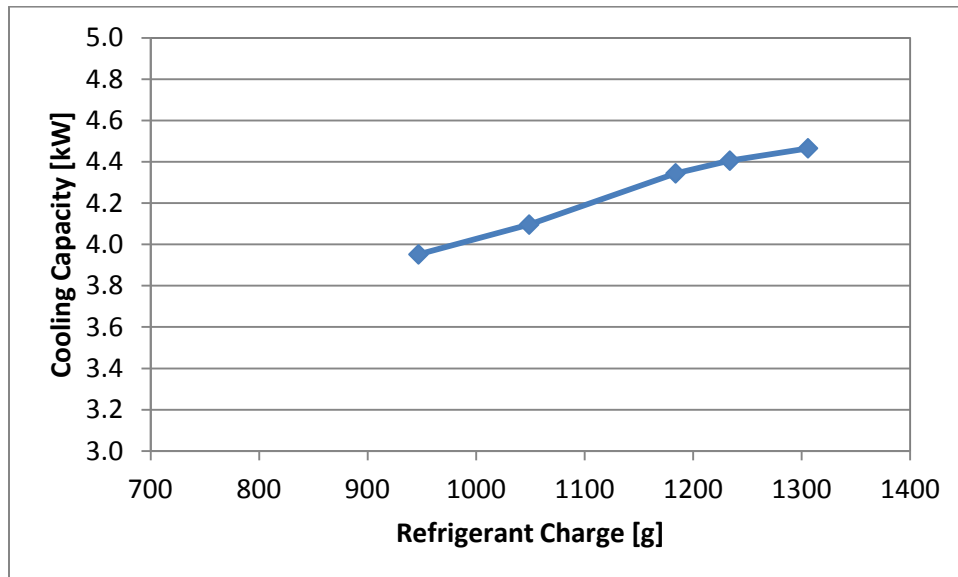
Figure C-4: Cooling capacity as a function of refrigerant charge

Appendix D: Cost Analysis

In order to construct the second optimization problem, the cost of the hot water storage tank, blower size, and inverter size had to be changed to correspond to different designs. The range of these equipments was set based on the range of the design variables. The cost of these equipments was based on the market prices in 2012. The cost of the hot water storage tank as a function of size for 60 tanks is shown in Figure D-1.
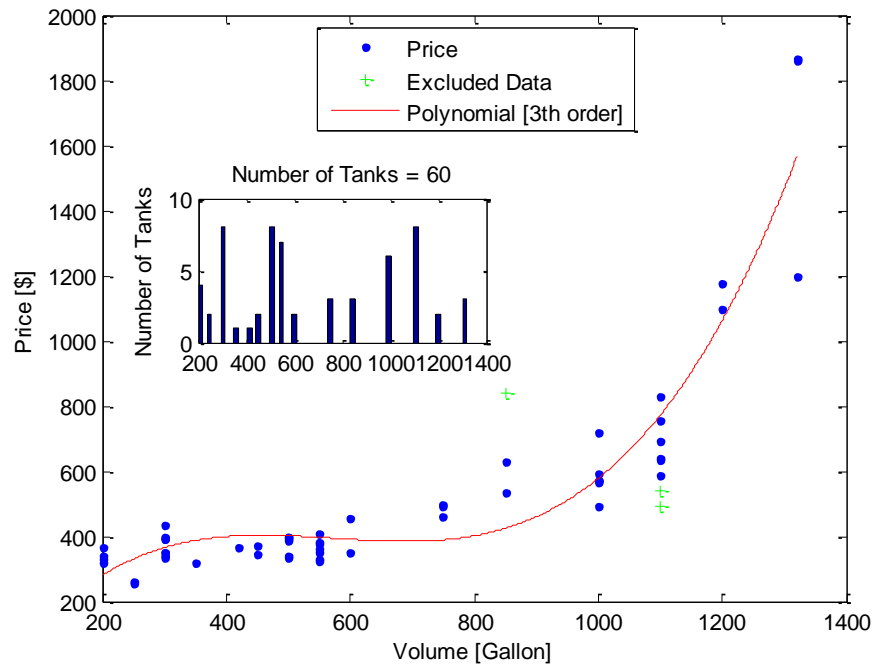
Figure D-1: The cost of different hot water storage tanks

The cost of 30 different blowers, for power range of 1/40 to 1/20 HP, is shown in Figure D-2. The blower power had to be changed to correspond to air mass flow rates.
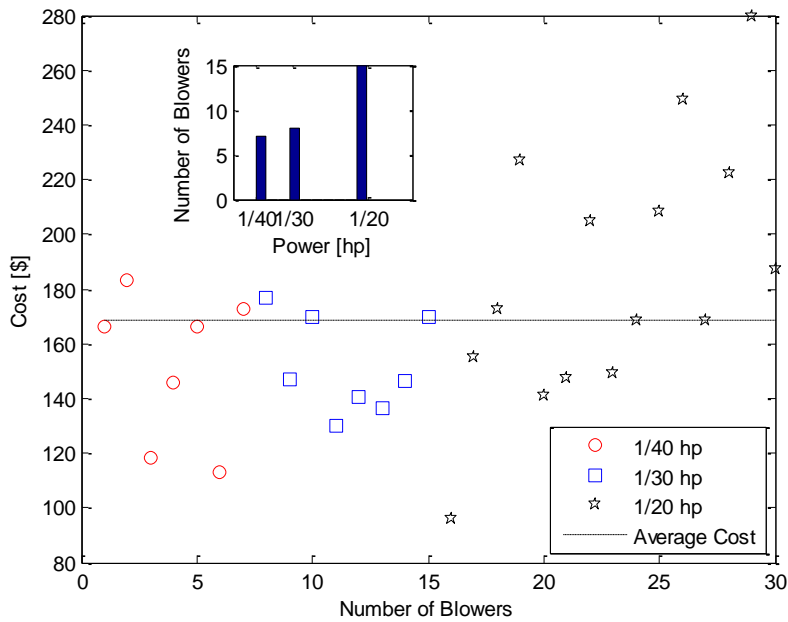
Figure D-2: The cost of air blowers.

The inverter size had to be selected based on the number of batteries. The cost of different inverters is shown in Figure D-3. The cost of the inverter was normalized by its capacity.
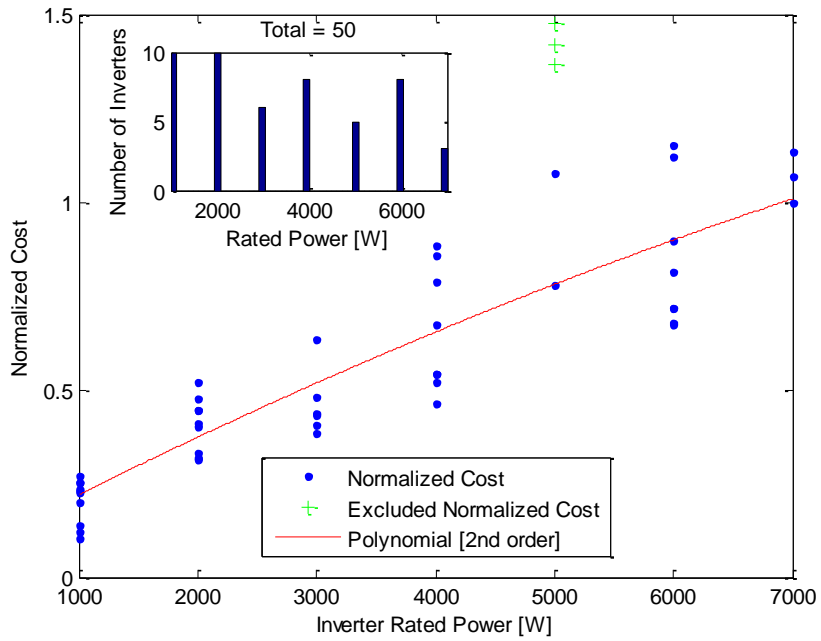
Figure D-3: The normalized cost of different inverters.

References

Antonellis, D.S , Joppolo, C.M., Molinaroli, L.(2010). Simulation, performance analysis and optimization of desiccant wheels. Energy and Buildings, 42(9), 1386–1393

Anyanwu, E.E. (2003). Review of solid adsorption solar refrigerator I: an overview of the refrigeration cycle. Energy Conversion and Management 44(2):301–12.

Arora, J.S., (2004). Introduction to Optimum Design with MATLAB, Introduction to Optimum Design, Second Ed, Academic Press, San Diego, 413-432.

ASHRAE 139, (2007). Methods of Testing for Rating Desiccant Dehumidifiers Utilizing Heat for Regeneration Process. American Society of Heating, Refrigerating and Air Conditioning Engineers.

ASHRAE 41.2, (1992). Standard Methods for Laboratory Air-Flow Measurement. American Society of Heating, Refrigerating and Air Conditioning Engineers.

ASHRAE Standard 116, (2010). Methods of Testing for Rating a Seasonal Efficiency of Unitary Air Conditioners and Heat pumps, Atlanta, GA.

ASHRAE. (2009). Fundamentals Handbook: Heating, Ventilating, and Air-Conditioning Applications. American Society of Heating, Refrigeration and Air Conditioning Engineering. Atlanta, USA.

ASHRAE standard 34, (1992), Designation and Safety Classifications of Refrigerants.

ASHRAE. (1999). HVAC Applications Handbook: Heating, Ventilating, and Air-Conditioning Applications. Atlanta, USA: American Society of Heating, Refrigeration and Air Conditioning Engineering Inc. CH.32.

Assoa, Y. B., Menezo, C., Fraisse, G., Yezou, R., & Brau, J. (2007). Study of a new concept of photovoltaic–thermal hybrid collector. Solar Energy, 81(9), 1132-1143.

Aute, V.C., Radermacher, R., Naduvath, M.A., (2004). Constrained Multi-Objective Optimization of a Condenser Coil Using Evolutionary Algorithms, 10th Int. Ref. and A-C Conf. at Purdue.

Badawy, M. T., (1998), Cycle analysis for solar ejector refrigeration and distillation system, In World Renewable Energy Congress, V. 4, pp. 2076 - 2079, Pergamon Press.

Beery, K.E. and Ladisch, M.R. (2001), Chemistry and properties of starch based desiccants, Enzyme and Microbial Technology 28 (7–8), 573–581.

Boubakri, A., Arsalane, M., Yous, B., Ali-Moussa, L., Pons, M., Meunier, F. , Guilleminot, J.J. (1992). Experimental study of adsorptive solar-powered ice makers in Agadir (Morocco): 1. Performance in actual site. Renewable Energy 2(1):7–13.

Brogren, M., Nostell, P., Karlsson, B. (2001). Optical efficiency of a PV–thermal hybrid CPC module for high latitudes. Solar Energy, 69(Supplement 6), 173-185.

Chow, T. T. (2003). Performance analysis of photovoltaic-thermal collector by explicit dynamic model. Solar Energy, 75(2), 143-152.

Chow, T. T., He, W., Ji, J. (2006). Hybrid photovoltaic-thermosyphon water heating system for residential application. Solar Energy, 80(3), 298-306.

Chung, T.W. and Chung, C.C. (1998). Increase in the amount of adsorption on modified silica gel by using neutron flux irradiation, Chemical Engineering Science 53 (16), 2967–2972.

Coventry, J. S. (2005). Performance of a concentrating photovoltaic/thermal solar collector. Solar Energy, 78(2), 211-222.

Critoph, R.E. (1993). Laboratory testing of an ammonia carbon solar refrigerator, ISES, Solar World Congress, Budapest, Hungary, 23–26.

Deb, K., (2001). Multi-Objective Optimization Using Evolutionary Algorithms. Wiley.

Dieng, A.O., and R.Z. Wang. (2001). Literature review on solar adsorption technologies for ice-making and air-conditioning purposes and recent developments in solar technology. Renewable and Sustainable Energy Reviews 5(4):313–42.

Dorantesa, R., C.A. Estradab, and I. Pilatowskyb. (1996). Mathematical simulation of a solar ejector-compression refrigeration system. Applied Thermal Engineering 16:669–75.

Duffie, J.A., Beckman, W.A., (1991). Solar engineering of thermal processes. Wiley-Interscience, New York.

Dunkle, R.V. (1965), A method of solar air conditioning, Mechanical and Chemical Engineering Transactions of the Institute of Engineers 73, pp. 73–78.

Eames, I.W., S. Aphornratana, and H. Haider. (1995). A theoretical and experimental study of a small-scale steam jet refrigerator. Int. J. Refrig. 18(6):378–86.

Enteria, N., Yoshino, H., Satake, A., Mochida, A., Takaki, R., Yoshie, R., Baba, S., (2010a). Development and construction of the novel solar thermal desiccant cooling system incorporating hot water production. Applied Energy 87, 478-486.

Enteria, N., Yoshino, H., Satake, A., Mochida, A., Takaki, R., Yoshie, R., Mitamura, T., Baba, S., (2010b). Experimental heat and mass transfer of the separated and coupled rotating desiccant wheel and heat wheel. Experimental Thermal and Fluid Science 34, 603-615.

Erhard, A., K. Spindler, and E. Hahne. (1998). Test and simulation of a solar powered solid sorption cooling machine. International Journal of Refrigeration 21(2):133–41.

Evans, D., Facinelli, W., Otterbein, R., (1978).Combined Photovoltaic/Thermal System Studies. Report ERC-R-78017, Arizona State University, Tempe, AZ

Figliola, R. and Beasley, D., (2000), Theory and Design for Mechanical Measurements, Third Ed., John Wiley & Sons, Inc.

Florschuetz, L. (1979). On heat rejection from terrestrial solar cell arrays with sunlight concentration. 11th IEEE Photovoltaic Specialists Conference Record (pp. 318–326). New York: IEEE.

Fraisse, G., Ménézo, C., & Johannes, K. (2007). Energy performance of water hybrid PV/T collectors applied to combisystems of direct solar floor type. Solar Energy, 81(11), 1426-1438.

Fujisawa, T. and Tani, T. (2001). Optimum Design for Residential photovoltaic-Thermal Binary Utilization System by Minimizing Auxiliary Energy. Electrical Engineering in Japan, 137 (1), 28-35.

García Casals, X., (2006). Solar absorption cooling in Spain: Perspectives and outcomes from the simulation of recent installations. Renewable Energy 31, 1371-1389.

GBU.(1995). Adsorption Chiller NAK, Technical Description. Retrieved from http://www.gbunet.de/outgoing/nak-prospect-e.pdf

Ge, T.S., Dai, Y.J., Wang, R.Z., Li, Y., (2008). Experimental investigation on a one-rotor two-stage rotary desiccant cooling system. Energy 33, 1807-1815.

Gebreslassie, B.H., Guillén-Gosálbez, G., Jiménez, L., Boer, D., (2009). Design of environmentally conscious absorption cooling systems via multi-objective optimization and life cycle assessment. Applied Energy 86, 1712-1722.

Ghali, K. (2008). Energy savings potential of a hybrid desiccant dehumidification air conditioning system in Beirut. Energy Conversion and Management,49(11), 3387–3390

Goswami, Y., Kreith, F. and Kreider, J.F. (2000). Principles of solar engineering. PA, USA: Taylor and Francis.

Grazzini, G., and A. Rocchetti. (2002). Numerical optimization of a two-stage ejector refrigeration plant. International Journal of Refrigeration 25:621–33.

Grenier, Ph., Guilleminot, J.J., Meunier, F. , Pons, M. (1988). Solar powered solid adsorption cold store. ASME Transactions—Journal of Solar Energy Engineering 110:192–97.

Grossman, G. (2002), Solar-powered systems for cooling, dehumidification and air-conditioning. Solar Energy 72(1):53–62.

Henning, H. (2007a). Solar-Assisted Air-Conditioning in buildings: A Handbook for Planners, 2nd ed. New York, USA: Springer Wien.

Henning, H. (2007b). Solar assisted air conditioning of buildings – an overview, Applied Thermal Engineering, 27 (10), 1734–1749

Henning, H.M., and H. Glaser.(2003), Solar assisted adsorption system for a laboratory of the University Freiburg. http://www.bine.info/pdf/infoplus/uniklaircontec.pdf.

Hildbrand, C., P. Dind, M. Pons, and F. Buchter. (2004). A new solar powered adsorption refrigerator with high performance. Solar Energy 77(3):311–18.

Huang B. J., Jiang C. B. and Hu F. I., (1985), Ejector performance characteristics and design analysis of jet refrigeration system, ASME J. Eng. Gas Turbines Power, 107, pp. 792–802.

Huang, B.J., J.M. Chang, V.A. Petrenko, and K.B. Zhuk. (1998). A solar ejector cooling system using

Huang, B.J., V.A. Petrenko, I.Y. Samofatov, and N.A. Shchetinina. (2001). Collector selection for solar ejector

Jeong, J., Yamaguchi, S., Saito, K., Kawai, S., (2010). Performance analysis of four-partition desiccant wheel and hybrid dehumidification air-conditioning system. International Journal of Refrigeration 33, 496-509.

Jia, C.X., Dai, Y.J., Wu, J.Y., and R.Z. Wang, (2006), Experimental comparison of two honeycombed desiccant wheels fabricated with silica gel and composite desiccant material, Energy Conversion and Management 47 (15-16), pp. 2523–2534

Jiang, H., Aute, V., Radermacher, R.,(2006). CoilDesigner: a general purpose simulation and design tool for air-to-refrigerant heat exchangers. International Journal of Refrigeration 29, 601–610.

Kalogirou, S. A. (2004). Solar thermal collectors and applications. Progress in Energy and Combustion Science, 30 (3), 231-295.

Kalogirou, S. A., Tripanagnostopoulos, Y. (2006). Hybrid PV/T solar systems for domestic hot water and electricity production. Energy Conversion and Management, 47(18-19), 3368-3382.

Kalogirou, S.A. and Tripanagnostopoulos, Y., (2007), Industrial application of PV/T solar energy systems, Applied Thermal Engineering, 27(8-9), 1259-1270.

Khattab, N. M. and M. H. Barakat, (2002), modeling the design and performance characteristics of solar steam-jet cooling for comfort air conditioning, Solar Energy, Volume 73, pp. 257-267

Khattab, N.M. (2004). A novel solar-powered adsorption refrigeration module. J. Appl. Therm. Eng. 24:2747–60.

Khattab, N.M. (2006). Simulation and optimization of a novel solar-powered adsorption refrigeration module. Solar Energy 80(7):823–33.

Khedari, J., Rawangkul, R. Chimchavee, W., (2003). Feasibility study of using agriculture waste as desiccant for air conditioning system, Renewable Energy 28 (10), 1617–1628.

Klein, S.A., Duffie, J.A., Beckman, W.A., (2007). TRNSYS 16, A transient simulation program, Thermal Energy System Specialists, LLC, Madison, WI.

Knez, Z. and Novak, Z. (2001). Adsorption of water vapor on silica, alumina, and their mixed oxide aerogels, Journal of Chemical and Engineering Data 46 (4), 858–860.

Kodama, A., Hirayama, T., Goto, M., Hirose, T., Critoph, R.E., (2001). The use of psychrometric charts for the optimisation of a thermal swing desiccant wheel. Applied Thermal Engineering 21, 1657-1674.

Kreith, F., and Kreider, J.F. (1978), Principles of solar engineering, Hemisphere publishing corporation, Washington, USA

Kribus, A., Kaftori, D., Mittelman, G., Hirshfeld, A., Flitsanov, Y., Dayan, A. (2006). A miniature concentrating photovoltaic and thermal system. Energy Conversion and Management, 47(20), 3582-3590.

Ladisch, M.R., (1997). Biobased adsorbents for drying of gases, Enzyme and Microbial Technology 20 (3), 162–164.

Lazarov, V., Schaeffer, C., Shishkov, M., Ivanova, M. (2005). Hybrid solar collector. Journal of Materials Processing Technology, 161(1-2), 229-233.

Loehrke, R. I., (1990), A passive, vapor compression refrigerator for solar cooling, Trans. ASME, J. Solar Energy Eng., V. 112, pp. 191–195.

Luo, H.L., R.Z. Wang, Y.J. Dai, J.Y. Wu, J.M. Shen, and B.B. Zhang. (2007). An efficient solar-powered adsorption chiller and its application in low-temperature grain storage. Solar Energy 81(5):607–13.

Mathiowitz, E., Jacob, J.S., Jong, Y.S. , Hekal, T.M. , Spano W., Guemonprez, R., (2001). Novel desiccants based on designed polymeric blends, Journal of Applied Polymer Science 80 (3), 317–327.

METEONORM. (2007). Global Meteorological Database for Engineers, Planners and Education.

Mitsubishi Plastics. (2010). Zeolitic Water Vapor Adsorbent, AQSOA, Retrieved from: www.mpi.co.jp.

Mittelman, G., Kribus, A., Dayan, A. (2007). Solar cooling with concentrating photovoltaic/thermal (CPVT) systems. Energy Conversion and Management, 48(9), 2481-2490.

Nehad, Al-Khalidy, (1998), An experimental study of an ejector cycle refrigeration machine operating on R113, Int. J. Refrig., V. 21 (8), pp. 612-625.

Nilsson, J., Hakansson, H. and Karlsson, B., (2007), Electrical and thermal characterization of a PV-CPC hybrid, Solar Energy, Vol. 81, pp. 917–928.

Panaras, G., Mathioulakis, E., Belessiotis, V., Kyriakis, N., (2010). Theoretical and experimental investigation of the performance of a desiccant air-conditioning system. Renewable Energy 35, 1368-1375.

Passos, E.F., J.F. Escobedo, and F. Meunier. (1989). Simulation of an intermittent adsorptive solar cooling system. J. Solar Energy 42(2):103–11.

Pennington NA. (1955). Humidity changer for air conditioning. USA, Patent No. 2,700,537

Pons, M., and J.J. Guilleminot. (1986). Design of an experimental solar-powered solid adsorption ice maker. J. of Solar Energy Eng. 108:332–37.

Pons, M., and J.J. Guillemiont. (1987). Experimental data on a solar-powered ice maker using activated carbon and methanol adsorption pair. J. of Solar Energy Eng. 109(4):303–10.

Pons, M., and Ph. Grenier. (1987). Experimental data on a solar-powered ice maker using activated carbon and methanol adsorption pair. Journal of Solar Energy Engineering, ASME Transactions 109:303–10.

Pridasawas, W., and P. Lundqvist. (2007). A year-round dynamic simulation of a solar-driven ejector refrigeration system with iso-butane as a refrigerant. International Journal of Refrigeration, (30) 5, 840–850

Roger A. and Ventre, M.J. (2005). Photovoltaic Systems Engineering, 2nd ed. Taylor & Francis.

Royne, A., Dey, C. J., Mills, D. R. (2005). Cooling of photovoltaic cells under concentrated illumination: A critical review. Solar Energy Materials and Solar Cells, 86(4), 451-483.

SACE, (2003). Solar Air Conditioning in Europe: Economic Study Results Report, Delft University of Technology, 2003, EU project NNE5/2001/00025

SHC, (2006). Solar Heating and Cooling Program, International Energy Agecy: Task 35- PV/Thermal Solar Systems,Netherlands

Stine, W.B., Geyer, W.B. (2001). Power from the sun. avialable at www.powerfromthesun.net
Subramanyam, N., Maiya, M.P., Murthy, S.S., 2004. Application of desiccant wheel to control humidity in air-conditioning systems. Applied Thermal Engineering 24, 2777-2788.

Sumathy, K., and L. Zhongfu. (1999). Experiments with solar-powered adsorption ice-maker. J. Renewable Energy 16:704–07.

The MathWorks, I., (2009). Genetic Algorithm and Direct Search Toolbox, User's Guide.

Threlkeld, J., Kuehn, T., Ramsey, J. (1998). Thermal Environmental Engineering, 3rd ed. USA: Prentice-Hall, Inc.

Tiwari, A., Sodha, M. S. (2006). Performance evaluation of solar PV/T system: An experimental validation. Solar Energy, 80(7), 751-759.

TRANE. (2008). Product Data: 4DCZ6036A through 4DCZ6060A. 22-1815-03

Vidal, H., S. Colleb, and G.d.S. Pereirab. (2006). Modeling and hourly simulation of a solar ejector cooling system. Applied Thermal Engineering 26(7):663–72.

Vokas, G., Christandonis, N., Skittides, F. (2006). Hybrid photovoltaic–thermal systems for domestic heating and cooling—A theoretical approach. Solar Energy, 80(5), 607-615.

Wang, R.Z., M. Li, Y.X. Xu, and J.Y. Wu. (2000). An energy efficient hybrid system of solar powered water heater and adsorption ice maker. Solar Energy 68(2)189–95.

Waugaman, D.G., Kini , A. Kettleborough, C.F., (1993). A review of previous desiccant term cooling systems, Journal of Energy Resources Technology 115 (1), 1–8.

Wetter, M., (2001). GenOpt – A Generic Optimization Program, Seventh International IBPSA Conference, Rio de Janeiro, Brazil, pp. 601-608.

Winkler, J., Aute, V., Radermacher, R. (2008). Comprehensive Investigation of Numerical Methods in Simulating a Steady-State Vapor Compression System, International Journal of Refrigeration (31), 930-942.

Yano, K., and Yoshiaki, F. (2003). Synthesis of super-microporous aluminosilicate having excellent water vapor adsorption property as an adsorbent for an adsorption heat-pump, "Journal of Porous Materials 10 (4), 223–229.

Zhai, X.Q., Wang, R.Z., (2009). A review for absorbtion and adsorbtion solar cooling systems in China. Renewable and Sustainable Energy Reviews 13, 1523-1531.

Zhang, X.J., Dai, Y.J., Wang, R.Z., (2003). A simulation study of heat and mass transfer in a honeycombed rotary desiccant dehumidifier. Applied Thermal Engineering 23, 989-1003.

Zondag, H. A., de Vries, D. W., van Helden, W. G. J., van Zolingen, R. J. C., van Steenhoven, A. A. (2002). The thermal and electrical yield of a PV-thermal collector. Solar Energy, 72(2), 113-128.

Zondag, H. A., de Vries, D. W., van Helden, W. G. J., van Zolingen, R. J. C., van Steenhoven, A. A. (2003). The yield of different combined PV-thermal collector designs. Solar Energy, 74(3), 253-269